Dielectrophoresis for Capillary Flow

Microfluidic Optoelectronics

A thesis submitted in fulfilment of the requirement for the degree of Doctor of Philosophy

By

DUNIA DANNO GILIYANA

School of Physics and Astronomy - Cardiff University

UK

June 2021

ABSTRACT

The development of a novel photonic integrated platform with three dimensional (3D) capillary flow and dielectrophoresis elements for chip based flow cytometers is discussed. Size-independent single stream particle focusing is the key for the efficient operation of a flow cytometer and many efforts have been made to reproduce it properly on a microchip scale.

In this work, capillary and negative Dielectrophoresis (n-DEP) components were integrated onto a single chip of III-V semiconductor material for conducting scattering measurements of microparticles. The integration of all components on a single chip is intended to result in low cost, portable and disposable microfluidic devices for point-of-care diagnostics. The design, fabrication and investigation of a system combining n-DEP with the capillary driven flow to align and reposition microparticles with fluid flow in a single stream around the centreline of the microchannel is considered. This is followed by testing the potential of n-DEP for efficient on-chip light scatter measurements. Planar microelectrodes face-to-face below and above the surface of the 3D microchannel are employed to create a localized non-uniform electric field to focus polystyrene microparticles in flowing fluid via n-DEP. The functionality of the device is assessed by detecting and counting 6 - 15 µm polystyrene microparticles (suspended in Deionised (DI) water) as an example to assess how similarly sized biological cells, such as blood cells, would flow within the fabricated 3D microchannel. The results show that the polystyrene microparticles are focused successfully in a single stream around the centreline of the 3D microchannel when operating the microelectrodes with an AC potential of 10 MHz and no more than 30 V peak-to-peak. The n-DEP focused microparticles show narrower velocity distribution, compared to randomly flowing particles, as well as exhibiting higher speeds (at the centre of the channel). The latter result suggests that a capillary-like speed profile is only present at the fluid front, and that the fluid flow becomes faster at the centre, behind the advancing meniscus, due to the greater friction at the microchannel's side walls. Consistent pulse shapes and peaks are observed in the laser data from the similarly sized polystyrene microparticles using a fully-integrated platform with lasers and photo-detectors. This suggests that the n-DEP focusing microelectrodes can significantly improve the operation efficiency of the device by regulating the flow of microparticles and passing them through a consistent scanning zone albeit with an increase in the precision of the fabrication required.

ACKNOWLEDGEMENTS

and nephews. I always remember their encouraging words through the toughest time and all the shared happy moments of my life. I love you all.

Finaly, I am deeply grateful to the love of my life, my husband, Marbina. Thank you for your love, patience, and support as I pursued this PhD journey. Thank you for keeping things going and for sharing my wish to reach the goal of completing this degree. Without you, I would not have overcome all the toughest moments, and I would not enjoy the happy times the same. The last word goes for Mariam, my 3 years old daughter, and Esho, my baby boy, who light up my life and who have given me the strength and motivation to get things done. Life has blessed me with you. If I could give you one thing in life, I would give you the ability to see yourself in my eyes, then you would realize how special you to me. I love you.

CONFERENCE PRESENTATION

1. D. Giliyana*, R. Thomas, A. Sobiesierski and P. M. Smowton, '**Dielectrophoresis for Semiconductor Integrated Optoelectronic Microfluidics**', Semiconductor Integrated Optoelectronic, UK, 2017

2. D. Giliyana*, E.Le Moulbar, A. Sobiesierski and P. M. Smowton, '**Dielectrophoresis for Semiconductor Integrated Optoelectronic Microfluidics**', Semiconductor Integrated Optoelectronics, Cardiff, UK, 2018

3. D. Giliyana*, E.Le Boulbar, B. Almagwashi and P. M. Smowton, '**Dielectrophoresis for Semiconductor Integrated Optoelectronic Microfluidics**, Dielectrophoresis 2018, UK, 2018

4. D. Giliyana*, E. Le Boulbar, S. Gillgrass and P. M. Smowton, '**Particle Manipulation and Control for Integrated Optoelectronic Microfluidics**', Semiconductor Integrated Optoelectronics, UK, 2019

5. D. Giliyana*, S. Gillgrass, B. Almagwashi, E. Le Boulbar, and P. M. Smowton, '**An Integrated Optoelectronic Microfluidic Platform for Particle Manipulation and Control**', UK Semiconductors, UK, 2019

6. D. Giliyana*****, Sara-Jayne Gillgrass, Basmah Almagwash, Emmanuel Le-Boulbar, S. Shutts and P. M. Smowton, '**An Integrated Optoelectronic Microfluidic Platform for Particle Manipulation and Control**', Photonics West, USA, 2020

CONTENTS

LIST OF FIGURES

LIST OF TABLES

Chapter 1

INTRODUCTION AND MOTIVATION

1.1 Research Background and motivation

Counting and identifying small particles such as cells is an important and commonly used measurement in clinical diagnosis. For example, counting different blood cells that present in a blood test can be used to diagnose a variety of medical conditions including anaemia or to identify fundamental health problem such as leukaemia. Until the 1950s the clinical test of the full blood cells in a specific volume relied on manual preparation of the blood smear and to the subsequent efforts to visually identify the blood cells under an optical microscope [1]. A skilled operator is needed to carry out this test. Hence, the method itself is laborious, time-consuming, and the results are subjected to several sources of inaccuracy such as handling and transportation time. Therefore, there were efforts to develop automated and fast blood cell analysis and investigation technologies that can provide initial information about a patient's health and whether further testing is needed.

Since the invention of the laser in the 1960s, an advanced technique such as flow cytometry has reformed the hematologic assay and allow automated cell analysis that overcomes the limitation of microscopic methods. A flow cytometer is considered as a powerful analysis tool to measure physical (for example; size and shape) and chemical properties (for example; cell cycle distribution and DNA contents) of cells or other particles as they passed in a single stream through a laser beam [1]. This is due to its ability to deliver accurate measurements of cellular components. Cellular

components of blood consist of three types of cells; red blood cells (RBCs), white blood cells (WBCs) and platelets [2], each serves different functions. WBCs form our immune system, defending the body against foreign pathogens and infectious disease. WBCs are produced and derived from multipotent cells in the bone marrow and any change in their percentage can be a sign of infections or disease. WBCs have a nucleus; thus, we can differentiate them from the anucleated RBCs and platelets. The main types of WBCs are granulocytes and agranulocytes. A granule, in cell biology, is a small particle that can be of any structure hardly visible under the optical microscope. WBCs can be classified further into: lymphocytes, monocytes, neutrophils, eosinophils and basophils. Table 1-1 shows the five different WBC types and their differences in granularity and nucleus shape.

Table 1-1 The five main WBC types, the category put in order from the most common to the least one for both main types [3]

Granulocyte		Agranulocyte	
Neutrophil		Lymphocyte	
Eosinophil			
Basophil		Monocyte	

Neutrophils are by far the most common of all the WBC types, constituting 50-70% of the WBC. They are usually 10-12 µm in diameter and are distinguishable due to the multilobed nucleus (normal neutrophils should have 3-5 lobes connected by slender strands). They are our defence against bacterial infection. Eosinophils are present in human blood with a percentage range between 1-5%. They have mainly a rounded

shape with diameter also around 10-12 µm. Their nucleus, however, is different in size and shape from that in a neutrophil. Generally, eosinophils nucleus are bi-lobed, and the lobes connected via a thin strand. Their level increases dramatically during allergies and parasitic infections such as worms. Basophils represent only less than 0.5% of the total count and have a smaller diameter of 8-10 µm. In general, the nucleus is with two or three lobes. They are also quite tricky to see due to several coarse dark violet coloured granules that hide it. However, these granules make it easy to distinguish from other blood cells. Basophils release histamine, which helps to widen blood vessels and increase the flow of blood to injured tissue, and heparin which inhibits blood from clotting. Lymphocytes are the second most common type of WBCs with a percentage of 20-45% and a size of 7-15 µm in diameter. They can be distinguished by their intense staining, rounded nucleus and a relatively small amount of cytoplasm. Monocytes are the largest type of WBCs with a diameter of 12-18 µm and a percentage of 3-9% from the total blood count. Their levels fall or spike depending on what is happening to the immune system. Conditions such as leukaemia and other types of cancer lead to a rise in monocytes level. Whilst side effects of medications will cause their level to lower for example in cancer chemotherapy (that can injure bone marrow) or the presence of diseases such as HIV and AIDS (that weaken the body's immune system) [4].

Much work has been done on the technological development of lab-on-chip devices or microfluidic flow cytometers to count WBCs and to perform the differential count of the 5-types of WBCs in a blood test, with high throughput. Many sources provide detailed descriptions of nature, history of flow cytometers as well as their operation and applications [1], [5]. Basically, the performance of a conventional flow cytometer is dependent on one of the three main components integral to it: i) the fluidic system (along with the flow focusing technique) for the introduction and placing of a large number of particles to be processed by passing them in a single stream through an optical system, ii) the optical system, which allows for illumination of particles and collection of emitted light (both forward and side scattered light intensities and often fluorescence), and iii) the system for data collection and data analysis. Figure 1-1 shows a schematic of a conventional flow cytometer with the position of the optical detection components.
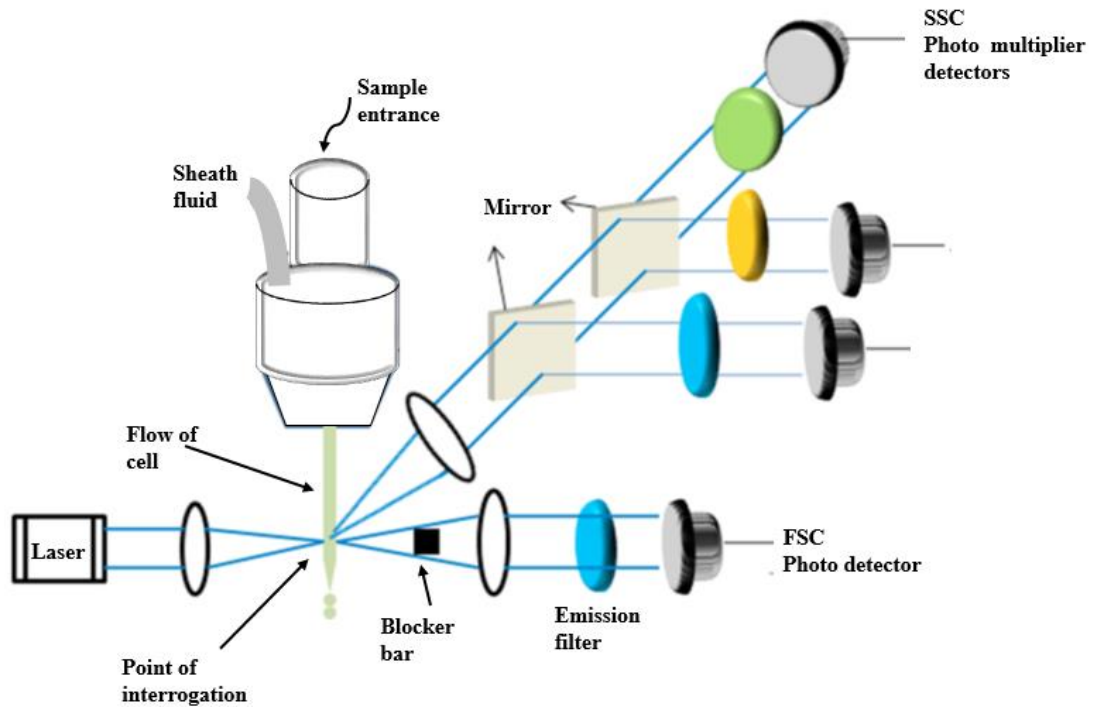
Figure 1-1 Schematic of a conventional flow cytometry showing the flow cell with hydrodynamic focusing, excitation optics and collection optics. Light scattering at different angles provides information about the number, size and type of investigated analyte [6].

In bench scale flow cytometry, the suspended cells or particles are hydrodynamically focused so that they will pass through the centre of the channel in a single profile at an equilibrium position. Therefore, focusing microparticles in the flow through a microfluidic system is the key for the efficient operation of a flow cytometer. It ensures microparticles (regardless to their size difference) passes through the detection region one at a time and more important at a steady velocity which reduces variation in the detected light intensity from the same sized microparticles. Once at the interrogation region, the cells or particles are each optically interrogated separately by a focused laser beam (typically about 20 – 40 µm in width) passing perpendicularly across the microchannel. Particle focusing is critical for device performance and reliability in such an optical system. A pulse is generated when a cell or particle passes through the laser beam. The pulse amplitude and shape relate to the interaction between the incident light beam and the cell or particle size, geometry and internal structure, as well as the fluorescence (again based on the system used). In addition, commercial flow cytometers have a sorting apparatus to isolate particles of interest and direct them into specific containers for further study. An advanced flow cytometer might be able to discriminate as many as 17 independent channels [7]. The current bench scale

cytometers are highly developed in terms of data acquisition and data processing but use very conventional optical components. They are expensive (cost between $50,000 and $400,000) to buy and costly to maintain, they are also very bulky. These concerns limit their affordability by point-of-care clinics and individual laboratories. Hence, efforts have been made to develop and commercialise miniaturised devices to reduce costs and promote portability. The key challenge to develop miniaturised flow cytometers that have comparable performance (accuracy, sensitivity and reproducibility) to their full-scale laboratory counterpart is to figure out how to drive down the size and cost of these three (fluidic along with the focusing and illumination and detection) core systems. If small relatively low cost optoelectronic microfluidic devices that are available to use within and out standard laboratory sites (as alternatives to an expensive state of the art systems), they would promote portability and affordability by individual laboratories and resource-poor settings throughout the world. Figure 1-2 shows an image of a BD FACSCalibur Flow Cytometer.

Figure 1-2 Image of a <u>BD FACSCalibur Calibur Flow Cytometer 4 Color</u> [from <u>https://images.app.goo.gl/x1LYbPvzsEEgJGEB7</u>]. The flow cytometer is costly, bulky, requires electricity and refrigerated reagents and a skilled operator for its operation and maintenance.

In this PhD, a novel photonic integrated platform with dielectrophoresis (DEP) particle focusing for chip-based flow cytometer is proposed. The microscale system combines an array of lasers and detectors for photo-voltage measurements across a microchannel with an on-chip capillary fill fluid delivery system and integrated microelectrodes. various size of microparticles can flow through an etched microchannel and become an active element between the two laser sections.

In the capillary fill fluid delivery system, capillary action is the only force driving the fluid and setting it into motion. Therefore, understanding how capillary driven flow behaves inside the microchannel will help to optimise the performance of DEP focusing force. Working in microscale domain and under low speeds, the flow within the microchannel is treated as a laminar flow. Laminar flow is characterised by a smooth flow of fluid in layers (parallel streamlines) with little to no lateral mixing. The particles travailing within such fluid can be expected to adhere to these streamlines. The flow itself is expected to slow down with time, so the speed of microparticles is expected to change with time or distance travelled inside the proposed microchannel. If microparticles are traveling at different heights, speed variations would be expected based on the height they were travelling at (slower close to the floor, or faster in the middle). This means that, for microparticle size that several microparticles can fit in the microchannel's height, the beam width caused by unfocused microparticle passing through the source/detector section in our intend device is a function of a microparticle hight inside the microchannel not the size of the microparticle. In other words, as the experimental set-up in this work does not provide a mechanism to measure the height at which the microparticles are travelling, whether the beam width belongs to microparticles traveling close to the floor or far from it is not clear. Therefore, focusing microparticles in the vertical direction is more important than the lateral one. Therefore, planar metallic electrodes, with cross (X) polarity of applied AC voltage, above and below the 3D capillary driven microchannel, is proposed and used to create a localised non-uniform electric field. The overall observation of microparticles, the applied field were capable of focusing polystyrene microparticles in the flowing fluid via the DEP method (the results obtained in chapter 4). The microparticles that flow downstream to the laser sections remain within the same focusing cross section as they were under the effect of the DEP (chapter 4). Basically, the variation in detected intensity from the same size microparticles flowing through the capillary driven microsystem would be insignificant compared to those without the DEP focusing effect reported in chapter 4. This would enhance counting and sorting purity in our final microdevice.

Furthermore, such a microsystem minimises the volume of blood required for accurate analysis that would allow for point-of-care clinics or in-situ haematological monitoring. It can be used in situations such as emergency surgery. This has already

been seen with the commercial HemoSepR technology [8], a system that can be used during any blood loss to measure the percentage red blood cells in the blood and recycle it so that it can transfuse back to the patient. We can imagine further development to our prototype, by integrating the data acquisition board (DAQ) and controlled electronics on chip and a smartphone could replace the personal computer or laptop. This would allow, for example, such a device to be inserted under the skin, offering a realistic route to continuous monitoring during everyday life. This is already available for patients with diabetes who require continuous glucose monitoring, using products such as the FreeStyle LibreTM [9].

1.2   Aim and research methodology

This work aims to develop a photonic integration platform with DEP particle manipulation for a chip-based flow cytometer that could perform light scattering measurements, focusing on narrow angle scattering detection. The development of the microfluidic structure was a two-fold task which includes i) building the dielectrophoretic unit that is capable of focusing polystyrene microparticles or cells (based on volumetric similarity to the WBC_s) in the flowing fluid stream into the centre of a microchannel with an on chip capillary driven system, before ii) integrating it with a III-V semiconductor substrate that owns its lasers and detectors for on chip light scattering measurements. This was achieved by designing the three main components; i) capillary fill fluid delivery system, ii) metallic microelectrodes above and below the 3D microchannel to focus microparticles in flow within a fluid flow stream to the centre of the microchannel using DEP technology and iii) an array of lasers and detectors, which were arranged perpendicular to the microchannel facing opposite each other. This would allow for narrow angle scattering measurements to be made on an analyte of choice. These components must be integrated on the same substrate (single chip) to benefit from integration. Therefore, the materials selection necessary to fabricate a fully integrated microchip is based on reasonable cost, stability, rapid fabrication and sample compatibility. Thus, an active III-V semiconductor substrate was used to build our prototype. Monolithically integrated light sources/detectors with 3D capillary filled fluidic delivery systems and dielectrophoresis microparticle manipulation technique are created on a single chip. This has been seen as the best solution not only to reduce the overall device size that would lower costs and enhance

portability but also to minimise light loss by having less optical interfaces to decrease the distance amongst components and improve alignment and coupling. This was achieved by the development of process flow that employs relatively fast and inexpensive techniques, enabling high-quality device fabrication. The final fabricated chip in Figure 1-3 shows a novel photonic integration platform with DEP capillary fill fluid delivery network for a chip-based flow cytometer.
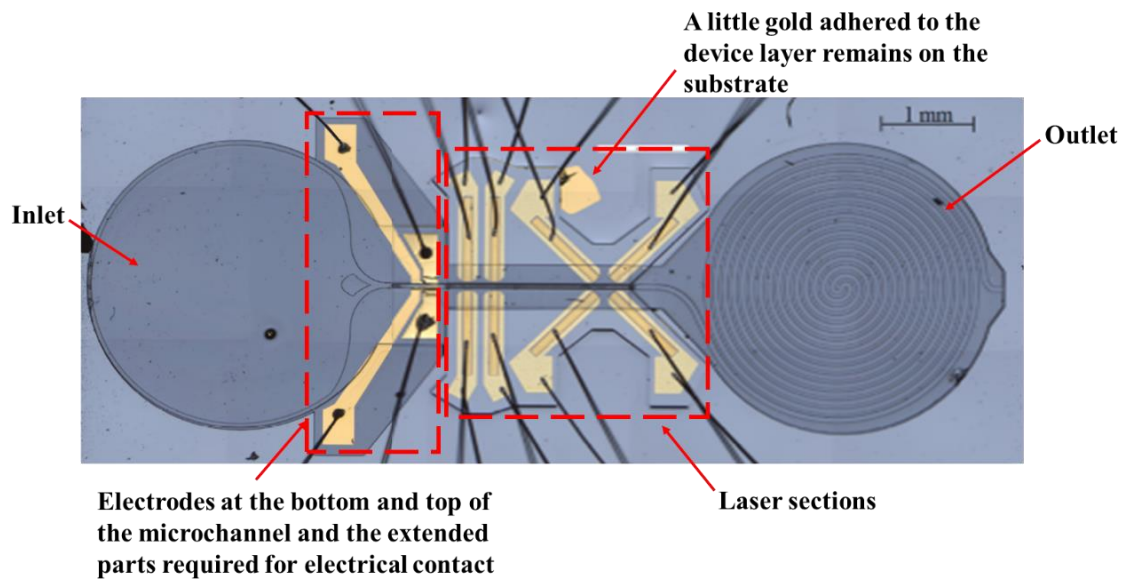
Figure 1-3 Plan view of an integrated chip with four microelectrodes, an array of oxide stripe lasers and the key components of the SU-8 capillary fill fluid delivery system. The figure shows, from left to right, inlet, straight channel and outlet of the roofless spiral channel. The spiral outlet geometry was considered to provide a sustained pull for a long duration.

In the early stages of this work, the strength of generated DEP focusing force, the effect of the applied AC non-uniform electric field, and its potential for application with the capillary filled fluidic delivery system was investigated using only an optical microscope and a high-speed camera. The resulting data (microparticle tracking) from experiments is analysed using an image processing code written in MATLAB R2018a software. For data (image) analysis, a high speed camera often struggles to capture the high rate of frames per second with enough resolution to provide any useful information about fluid motion and particle flow to verify the performance of the DEP capillary filled microchip. With pulsed laser operation, using a photo-voltage output change during a microparticle transit event, the potential of this device for flow cytometer applications is shown through the ability of detecting polystyrene microparticles.

1.3   On-chip integrated components

The high level of integration (the ability of integrating different optical elements, fluid focusing and cell manipulation) on a single chip would bridge the gap between the developing microfluidic platforms and the already commercially available benchtop flow cytometers. Over the last decade, researchers have developed microfluidic flow cytometers using externally pumped systems, coupled with semi-integrated optics of optically passive material such as glass, silicon and Polydimethylsiloxane (PDMS). However, no one was yet ready to replace the bench scale systems in the clinic, as they are still expensive and bulky. Fluid focusing on microfluidic systems has been commonly demonstrated using off chip pumping techniques [10], [11]. In recent years, there are some remarkable examples where pumping and microvalves have been integrated on chip [12], [13]. Hydrodynamic focusing is the most commonly used fluid confinement method. Using such an approach, microparticles such as cells can be confined into a narrow stream by focusing another fluid stream, known as the sheath fluid. This type of fluid confinement is typically two dimensional, where the sample flow is concentrated in the lateral direction that limits the amount of variation of the detected signal intensity. In practice, this will increase the throughput but will not solve the confinement problem, as the microparticle flowing through the microchannel continues to move freely in the vertical direction. The microparticles near the bottom and top surface of the microchannel are likely to travel at a different velocity than those moving in the centre. This would increase the probability of a false count, and more importantly increase variation in detected signal intensities from the same sized microparticles reducing device performance and accuracy. Researchers have demonstrated devices with 3D hydrodynamic flow focusing (width and depth) with the achievement of the fluid confinement in the vertical direction [14]. However, in practice, such techniques have not wildly been adopted due to increased complication in the fabrication process flow. Advanced strategies for microfluidic based cytometers have demonstrated fluid focusing using capillary action and narrow channels that forces flowing particles through a narrow detection zone without the need for any external pump system [15]. However, the probability of channel clogging increases compared with examples using hydrodynamic focusing, this is due to the particles flowing through a narrow channel experiencing increased shear stress due to fluid viscosity (fluid deform pattern inside the microchannel). Various techniques have been

developed and employed to-date to achieve focusing in micro-scale devices including dielectrophoresis (DEP). DEP is defined as the motion of a neutral particle due to the action of a non-uniform electric field on the particles' induced dipole. It depends, among other factors, on the size and dielectric properties of a particle and surrounding medium, which represent the morphological and chemical characteristics of bioparticles (e.g. cells), that allows highly sensitive and selective analysis. The particle and the surrounding fluid become electrically polarised in the presence of an electric field. Depending on the relative polarizability of both the particle and the surrounding fluid, a net DEP force will either attract the particles towards the region of higher electric field gradient (positive DEP, p-DEP) or repel them away from the region of electric field strength maximum (negative DEP, n-DEP) [16]–[21]. DEP can be generated either by using direct current (DC) or alternating current (AC) field, and both have been successfully applied for particle manipulations. However, the AC-DEP is more favourable due to the lower operating voltage that prevents Joule heating [22], making the microfluidic system compatible with biological cell manipulation. In a microsystem, the microparticles or cells that are exposed to either AC or DC electric field might be negatively affected. However, it is very difficult to know the consequences of this exposure; thus, the interaction of microparticles with the applied electric field needs to be decreased to reduce any effects.

In addition to the fluid or particle focusing, one of the essential steps in the development of point-of-care devices is to precisely shape and deliver excitation laser light to the fluidic microchannel. Then the scattered and fluorescence (based on the system in use) light will be detected by the photo-detectors. This localisation of the excitation beam and light collection will have a positive impact on improving the signal-to-noise ratio. There are various approaches to integrated optical systems with the microfluidic chip presented in the literature. The simplest way is through direct fibre to the vicinity of the microchannel [23]. A more complex solution can be found in integrated waveguides [24], lens and fibre to waveguide coupler [25] in which all of these optical elements have been defined in one layer of SU-8 negative photoresist by standard photolithography. While fibres and lenses have been a good start to the on chip optical system integration, they are not a complete solution. Both fibres and waveguides emit a diverging cone of light which means less directional and non-uniform illumination beam. The lenses are commonly two dimensional; consequently,

the light path is unaffected in the vertical direction. Besides, lenses require high optical-quality facets, near-vertical sidewall and even perfectly smooth surface. Further development, to facilitate the complete system on single chip or substrate, has demonstrated an integrated III-V semiconductor substrate that carries a coupled array of light sources and detectors along with an on chip capillary fill fluid delivery system [26]. However, the variation in speed caused by unfocused particles flowing under the capillary action resulted in measured intensity variations from the same sized (identical) microparticles. The resulting required data analysis is complicated and time-consuming. Therefore, it is important to focus micro-scale particles into the centre of the microchannel prior to any functions on the microdevices, such as counting, characterisation and sorting/separation. Hence, in this work, the well-known dielectrophoresis (DEP) method in pump driven system is proposed and used to drive the particles in the stream by two pairs of microelectrodes. This objective requires redesign the chip's mask and development of fabrication process for the new microsystem as well as testing the design's performance experimentally before integrating it with a semiconductor substrate. As a result, the spread of the measured focused particles under the DEP force is significantly improved compared to those without DEP.

1.4   Thesis structure

This chapter has introduced the general flow cytometry concept and DEP phenomena. Also mentioned are the motivation behind higher integration of on chip components, objectives and research methodology.

Chapter 2 presents a detailed theoretical description concerning the context of the succeeding chapters. We have derived expressions of the dipole moment and DEP force for a neutral spherical particle. We have discussed some important features of the DEP force. Scaling analysis is presented to consider the appropriate size of the 3D microchannel and its scaling effects on DEP force. In the following sections, we have provided some theoretical basis of the quantum well (QW) semiconductor laser devices. Light scattering based on the angle scattering detection and individual visualisation of the analyte of choice is also discussed. Thus, in principle, it should be

able to distinguish microparticles (e.g. cells) based on their size. This knowledge was fundamental in the formulation of this project.

Chapter 3 includes a discussion of the design and fabrication work that has been undertaken to develop the final version of the photonic integrated platform with DEP particle focusing for chip based flow cytometer. The monolithic nature of the design requires a deep foundation for fluidic microsystem, along with adhesion and physical insulation layers, which is achieved using a plasma etching process. The channel is in the range of 27 - 30 µm deep and is etched into the surface of an active GaAs crystal. SU-8 negative photoresist is deposited to form the capillary filled fluid delivery system so that the optical axis of the lasers/detectors will intersect with the middle point of the 3D microchannel. The length of the 3D microchannel is proposed and designed so that it can accommodate the microelectrodes and laser sections. The localised DEP force is generated by the mean of integrated metallic microelectrodes. Triangular-shaped microelectrodes, face-to-face above and below 3D capillary driven microchannel, create a highly localised non-uniform AC electric field, capable of focusing polystyrene microparticles in a flowing fluid via n-DEP. Two laser/detector pairs are patterned perpendicular to the microchannel facing opposite to each other. This is the minimum number of required forward scatter measurements that would allow for error checking results and calculating the microparticle velocity at the point of interrogation. Thus, the length of the microsystem is proposed to accommodate the required components (metallic microelectrodes, two laser/detector pairs and longer microelectrode or extra laser sections if needed) while reducing the final chip size. This would have a positive impact of reducing waste of III-V semiconductor active material and so reducing the total cost per device. The materials used to make our microdevice are biocompatible; therefore, in principle, the prototype should be able to distinguish biological cells in a blood sample based on their size.

Chapter 4 demonstrates a combination of the DEP phenomena, more familiar in pump driven systems, and laminar flow in a 3D capillary fill fluid delivery system to align and position microparticles within a flowing fluid in a single stream around the centre of a microchannel without any external pump or syringe systems. This is based on dielectric properties of microparticles and the surrounding medium and the strength of the generated a non-homogeneous AC electric field. A theoretical study is presented to estimate the operational frequency values for the parameters of a microparticle and

medium. The response of the 6 and 10 μm polystyrene particles to the AC electric field is demonstrated. The microparticles were used as an example to assess how biological cells, and mainly WBCs, might flow within the fabricated 3D capillary driven microsystem based on volumetric similarity. The lateral position of microparticles downstream where lasers/detectors might be in our final device is also discussed to show the effectiveness of the microelectrodes design and the strength of the generated DEP force in the device performance.

Chapter 5 concentrates on the microparticles velocity distribution with two different configurations of the applied AC field (side-to-side and cross (X)-pattern). This has the potential to reduce the distribution of velocities of the microparticles, by reducing the variation in position across the fluid channel. The separation distance between focused microparticles and the implication for interrogation of close particles is also discussed. Experimental analyses were performed on polystyrene microparticles of two different sizes. Particle tracking measurements were carried out using two different methods; i) using the object tracking tool from the control software for tracking the lateral position of a single particle through the video frames in the AVI player and ii) a MATLAB R2018a software.

Chapter 6 presents a novel photonic integrated microfluidic platform with a DEP element and laminar flow to count and discriminate microparticles. It concentrates on essential practical features related to small angle light scattering measurements. We can, through the microfluidic device, monitor polystyrene microparticles under the well-controlled microenvironment without any external pump or syringe system. Using the perturbation in the light signals across a microchannel, we measure a photo-voltage output change during a particle transit event. This provides the potential to overcome the variations in detected intensities from the same sized particle and remove the need for complicated data analysis allowing for in-situ haematology assessment.

Chapter 7 concludes this work with a summary and suggests directions for future research.

1.5   Bibliography

[1]   H. M. Shapiro, "Practical Flow," *John Wiley Sons, Inc.*, p. 724, 2003.

[2]   R. Hoffman, E. Benz, and S. Sanford, "Hematologia. Principios Basicos y Practica," p. 2451, 2013.

[3]   F. Article, "Medical gallery of Blausen Medical 2014," *WikiJournal Med.*, vol. 1, no. 2, 2014, doi: 10.15347/wjm/2014.010.

[4]   L. Putzu and C. Di Ruberto, "White Blood Cells Identification and Classification from Leukemic Blood Image," *Proc. IWBBIO Int. Work …*, no. January, pp. 18–20, 2013.

[5]   A. L. Givan, "Principles of flow cytometry: An overview," *Methods Cell Biol.*, vol. 63, no. 63, pp. 19–50, 2001, doi: 10.1016/s0091-679x(01)63006-1.

[6]   H. S. Aaron r. Hawkins, *Handbook of Optofluidics*. Taylor & Francis Group, LLC, 2010.

[7]   P. K. Chattopadhyay *et al.*, "Quantum dot semiconductor nanocrystals for immunophenotyping by polychromatic flow cytometry," *Nat. Med.*, vol. 12, no. 8, pp. 972–977, 2006, doi: 10.1038/nm1371.

[8]   C. A. Robertson and T. Gourlay, "Development of a diagnostic sensor for measuring blood cell concentrations during haemoconcentration," *Perfus. (United Kingdom)*, vol. 32, no. 2, pp. 126–132, 2017, doi: 10.1177/0267659116667806.

[9]   U. Hoss and E. S. Budiman, "Factory-calibrated continuous glucose sensors: The science behind the technology," *Diabetes Technol. Ther.*, vol. 19, no. S2, pp. S44–S50, 2017, doi: 10.1089/dia.2017.0025.

[10]   K. Sato *et al.*, "Integration of an immunosorbent assay system: Analysis of secretory human immunoglobulin A on polystyrene beads in a microchip," *Anal. Chem.*, vol. 72, no. 6, pp. 1144–1147, 2000, doi: 10.1021/ac991151r.

[11]   M. A. McClain, C. T. Culbertson, S. C. Jacobson, N. L. Allbritton, C. E. Sims, and J. M. Ramsey, "Microfluidic Devices for the High-Throughput Chemical Analysis of Cells," *Anal. Chem.*, vol. 75, no. 21, pp. 5646–5655, 2003, doi: 10.1021/ac0346510.

[12] A. Y. Fu, H. P. Chou, C. Spence, F. H. Arnold, and S. R. Quake, "An integrated microfabricated cell sorter," *Anal. Chem.*, vol. 74, no. 11, pp. 2451–2457, 2002, doi: 10.1021/ac0255330.

[13] K. W. Oh and C. H. Ahn, "A review of microvalves," *J. Micromechanics Microengineering*, vol. 16, no. 5, 2006, doi: 10.1088/0960-1317/16/5/R01.

[14] C. G. Hebert, S. J. R. Staton, T. Q. Hudson, S. J. Hart, C. Lopez-Mariscal, and A. Terray, "Dynamic radial positioning of a hydrodynamically focused particle stream enabled by a three-dimensional microfluidic nozzle," *Biomicrofluidics*, vol. 9, no. 2, p. 024106, 2015, doi: 10.1063/1.4914869.

[15] S. M. Stavis, J. B. Edel, K. T. Samiee, and H. G. Craighead, "Single molecule studies of quantum dot conjugates in a submicrometer fluidic channel," *Lab Chip*, vol. 5, no. 3, pp. 337–343, 2005, doi: 10.1039/b416161k.

[16] D. Holmes, H. Morgan, and N. G. Green, "High throughput particle analysis: Combining dielectrophoretic particle focussing with confocal optical detection," *Biosens. Bioelectron.*, vol. 21, no. 8, pp. 1621–1630, 2006, doi: 10.1016/j.bios.2005.10.017.

[17] H. Morgan, D. Holmes, and N. . Green, "3D focusing of nanoparticles in microfluidic channels," *IEEE Proc. nanobiotechnology*, vol. 152, no. 6, pp. 207–211, 2003, doi: 10.1049/ip-nbt.

[18] A. Hilal-Alnaqbi, A. Alazzam, S. Dagher, and B. Mathew, "Analysis of dielectrophoresis based 3D-focusing in microfluidic devices with planar electrodes," *Proc. Annu. Int. Conf. IEEE Eng. Med. Biol. Soc. EMBS*, no. July, pp. 3588–3591, 2017, doi: 10.1109/EMBC.2017.8037633.

[19] F. Alnaimat, S. Krishna, A. Hilal-Alnaqbi, A. Alazzam, S. Dagher, and B. Mathew, "3D focusing of micro-scale entities in dielectrophoretic microdevice," *Med. Devices Sensors*, vol. 2, no. 2, pp. 1–11, 2019, doi: 10.1002/mds3.10028.

[20] H. Chu, I. Doh, and Y. H. Cho, "A three-dimensional particle focusing channel using the positive dielectrophoresis (pDEP) guided by a dielectric structure between two planar electrodes," *Trans. Korean Soc. Mech. Eng. A*, vol. 33, no. 3, pp. 261–264, 2009, doi: 10.3795/KSME-A.2009.33.3.261.

[21] M. Li, W. H. Li, J. Zhang, G. Alici, and W. Wen, "A review of microfabrication techniques and dielectrophoretic microdevices for particle manipulation and separation," *J. Phys. D. Appl. Phys.*, vol. 47, no. 6, 2014, doi: 10.1088/0022-3727/47/6/063001.

[22] B. Cetin and D. Li, "Effect of Joule heating on electrokinetic transport," *Electrophoresis*, vol. 29, no. 5, pp. 994–1005, 2008, doi: 10.1002/elps.200700601.

[23] Y. C. Tung, M. Zhang, C. T. Lin, K. Kurabayashi, and S. J. Skerlos, "PDMS-based opto-fluidic micro flow cytometer with two-color, multi-angle fluorescence detection capability using PIN photodiodes," *Sensors Actuators, B Chem.*, vol. 98, no. 2–3, pp. 356–367, 2004, doi: 10.1016/j.snb.2003.10.010.

[24] J. Godin and Y.-H. Lo, "Two-parameter angular light scatter collection for microfluidic flow cytometry by unique waveguide structures," *Biomed. Opt. Express*, vol. 1, no. 5, p. 1472, 2010, doi: 10.1364/boe.1.001472.

[25] Z. Wang *et al.*, "Measurements of scattered light on a microchip flow cytometer with integrated polymer based optical elements," *Lab Chip*, vol. 4, no. 4, pp. 372–377, 2004, doi: 10.1039/b400663a.

[26] R. Thomas, A. Harrison, D. Barrow, and P. M. Smowton, "Photonic integration platform with pump free microfluidics," *Opt. Express*, vol. 25, no. 20, p. 23634, 2017, doi: 10.1364/OE.25.023634.

Chapter 2

THEORY AND BACKGROUND

2.1 Introduction

This chapter presents the theory behind the basic components used to create the final device. It covers the components that would guarantee the functionality of a portable device without sacrificing the analytical capabilities of benchtop flow cytometers. It covers the theory behind dielectrophoresis (DEP), the force used to move and align the individual microparticle to an equilibrium position within the capillary driven system. We believe this would have a positive effect on reducing variations in the detected signal intensities and enhance microparticle sorting purity compared to those without the DEP effect. We discuss specific considerations and fundamental limitations for DEP applied to microparticle manipulation. Later in this chapter, a description is given of the drag force arising on microparticles in movement through viscous fluid in flow. A good understanding of the fundamentals of laser diodes is necessary to understand device functionality and make connections between device outlines and performance. Therefore, this chapter introduces the general principles of the semiconductor laser. It starts with optical transmission in a two-level system and moves on to threshold gain in a quantum well material, which was used to fabricate the experimental devices. The final part of this chapter covers scattered light from a single microparticle. This knowledge can be used to extract the microparticle's physical properties such as size.

2.2 Flow control

In bench scale flow cytometry, focusing the sample flow regardless of its size variation into a single stream to the centre of the microchannel is essential to reduce variations in detected signal intensity and enhance particle sorting purity. In other words,

identical travel through the interrogation region ensures repeatability and illumination uniformity, leading to reliable detection and reducing the possibility of false-sort events. For these reasons, significant efforts have been made to incorporate effective and elegant focusing techniques into a microfluidic flow cytometry. In general, flow control in microfluidics can be achieved using active or passive pumps. Recently, capillary drive has been used due to its simplicity of use, as it does not need any external pump or syringe systems. The technique is based on surface tension as the only force driving the fluid along the channel and setting it into motion. However, this approach also has its inherent drawbacks. For example, fluid flow is less controlled than with an external pump, and particle velocity depends on its relative position within the channel cross section. Thus, while dielectrophoresis has been demonstrated to be effective in pumped systems, in this work I investigate its potential for application with capillary driven microfluidics, leading towards a true fully chip size particle sensing system with its own monolithic integrated lasers and photo-detectors. Consequently, these phenomena and the parameters on which they are based need to be understood and will be described in the next section.

2.3 Dielectrophoresis (DEP)

When an electrically neutral microparticle is exposed to an external electric field, positive and negative charges are induced on its surface, forming electric dipoles [1]. The interaction between the applied electric field and the induced dipole generates a force acting on the microparticle. The direction and magnitude of this force depend on several variables; the dielectric properties of microparticles and the surrounding medium, the size of microparticles, and the magnitude and frequency of the applied electric field. The force mainly depends on the non-uniformity of the applied electric field.

In a uniform electric field, the neutral microparticle does not experience a net force; this is because two halves of the microparticle feel opposite directional forces, equal in magnitude, so they cancel each other out. However, if the electric field is inhomogeneous, the forces on either side of the microparticle are different in magnitude, and the overall forces result in microparticle movement either toward or against areas of high field intensity. This is based on the relative polarizabilities of the microparticle and the medium [2]. This phenomenon is known as the dielectrophoresis

force [3]. The direction of the DEP force is independent of the polarity of the applied voltage; thus, the phenomena can be found under the influence of direct current (DC) as well as alternating current (AC) fields. Using the AC electric field has the great advantage of avoiding problems such as temperature increase inside the microchannel (Joule heating). This temperature increase within the microchannel may form bubbles or damage bioparticles [4][5]. For example, as reported in [5], 4ºC above physiological cell temperature for a mammalian cell can lead to cell death.

In a non-uniform AC electric field, like the one generated in this research, where the field strength around the edge of the microelectrodes is greater than other regions, the imbalance of forces on either side of the induced dipole would result in microparticle motion.
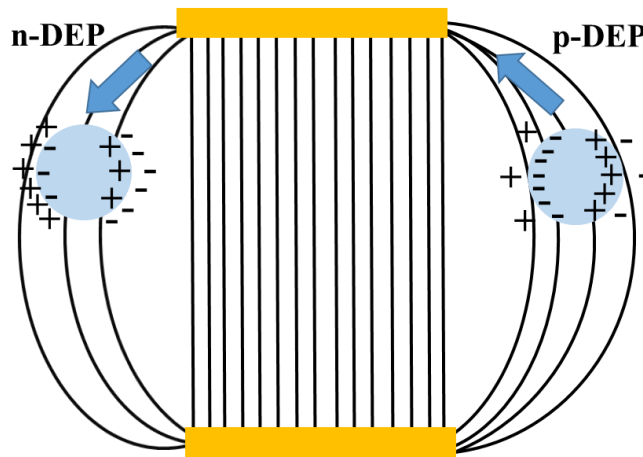
Figure 2-1 Schema of how different dielectric microparticles polarise under a non-uniform electric field. If the microparticles have lower polarizability than the surrounding medium, more charges are produced on the outside of the microparticle/medium interface and the forces on the dipole are imbalanced, and a so-called n-DEP force is exerted to push the microparticles away from the high electric field regions. The opposite case gives rise to p-DEP force. (no polarity dependence).

When the polarizability of the microparticle is lower than that of the surrounding medium, as in the studied case, as also in the case of blood cells, the microparticle experiences a net force which drives it in the direction of the minimum electric field regions. This gives rise to negative dielectrophoresis (n-DEP), as shown in Figure 2-1. This condition allows for less stress in cases where manipulation of biological objects is required, and so it has advantages. The opposite situation gives rise to positive dielectrophoresis (p-DEP), as shown in Figure 2-1, and in this case, the microparticles experience a net force in the direction to the maximum electric field line density.

In quantitative terms, the net DEP force upon a microparticle can be expressed as a dipole moment (P) times the gradient of the electric field (E)[3]. Therefore, it is important to introduce the basic concept of the induced dipole, as presented in the next sub-section.

2.3.1   Force on a dipole in an electric field

The charge distribution at the interface between two dielectrics can be described by introducing the mean of polarizability. Polarizability can be defined as a material's ability to produce charges at the interface in the presence of an external electric field [6]. For electrically neutral microparticles suspended in a dielectric solution and exposed to an external electric field, such as the studied case, the positive and negative charges are expected to accumulate at each side of the interface. This redistribution of charges at the interface gives rise to a dipole around the microparticle, and the dipole itself will experience a net force that acts through the entire body of the medium. Therefore, to drive the expression for DEP force, we consider the simple picture of a dielectric microparticle of radius R, e.g. a biological cell, occupying region Ω in space centred on the position vector r_0 in a non-uniform electric field E having electric charge density ρ, as illustrated in the figure below.
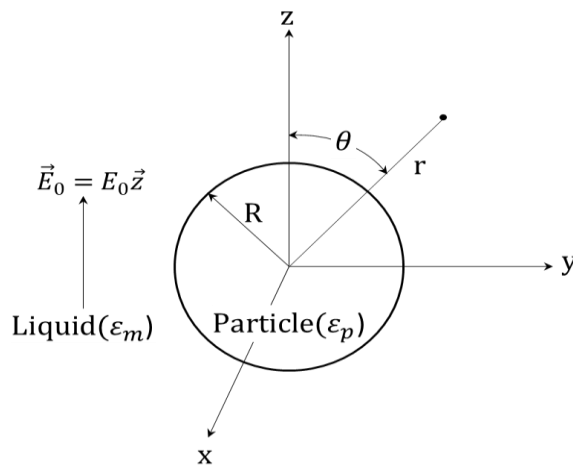
Figure 2-2 Dielectric uniform sphere of radius R and permittivity ε_p suspended in a dielectric fluid of permittivity ε_m and subjected to a uniform z-directed electric field of magnitude E_0.

The resulting force should satisfy the Navier-Stokes equation, and, the i'th component of electric force F_i (where i referred to the x, y and z- components in three dimensional cartesian coordinates) can be written as follows [7]:

$$F_i = \int_\Omega \rho\,(r + r_0)E_i\,(r + r_0)dr, \tag{2.1}$$

where $(r + r_0)$ denotes the general position inside the particle. Then, the electric field can be expanded as a power series where the induced higher order multipolar terms other than dipole moment are ignored. This is acceptable for moderate non-linear electric field [8], which is the typical situation for DEP-based lab-on-chip devices. Therefore, the expression of E_i can be written as:

$$E_i(r + r_0) \approx E_i(r_0) + (r.\nabla)E_i(r_0), \tag{2.2}$$

So, the force on the particle can be expressed as:

$$F_i \approx \int_\Omega \rho(r + r_0)dr\,E_i(r_0) + \left(\int_\Omega \rho(r + r_0)rdr.\nabla\right)E_i(r_0), \tag{2.3}$$

where the integral terms represent the monopole and dipole moment contributions respectively. The electric dipole moment, P, and the net charge, Q, can be defined as:

$$P = \int_\Omega \rho(r + r_0)rdr$$

$$Q = \int_\Omega \rho(r + r_0)dr, \tag{2.4}$$

Q is zero for an electrically neutral microparticle, so the monopole term in the previous equation is zero. However, the force still presents if the electric field gradient and dipole are non-zero. Under these conditions, the approximation expression of the force on an infinitesimal dipole in an electric field can be [3], [7], [9]

$$F_{dipole} = (P.\nabla)E \tag{2.5}$$

The above expression shows that no net force can be found on a dipole unless the applied electric field is inhomogeneous, which is the case for DEP based microfluidics. The next step involves the derivation for the induced dipole moment so that it can be used in the previous equation to define the DEP forces on microparticles.

The resulting electric potential Φ on a uniform dielectric particle of radius R should satisfy Laplace's equation. The divergence of the electric field is finite, and so the curl is zero ($\nabla^2\Phi = 0$). The solutions for the potential inside the microparticle Φ_p and the medium Φ_m have been expressed as [9]:

$$\Phi_p(r, \theta) = -A\,r\cos\theta, \qquad \text{for r} < R \tag{2.6}$$

$$\Phi_m(r, \theta) = -E_0 \, r \cos\theta + B \frac{\cos\theta}{r^2}, \qquad \text{for } r > R \qquad (2.7)$$

where r and θ are the radial positions and the angular coordinate, respectively, and A and B are the coefficients which have been determined using the standard boundary conditions: i) the electric potential is continuous across the microparticle surface, and ii) on either side of the microparticle's surface the normal component of the displacement flux $\varepsilon(\partial\Phi/\partial r)$ remains the same. Flux is a vector quantity, describing the magnitude and direction of the flow of a substance or property. Hence, the two boundary conditions can be expressed as:

$$\Phi_p(r = R, \theta) = \Phi_m(r = R, \theta), \qquad (2.8)$$

$$\varepsilon_p E_p(r = R, \theta) = \varepsilon_m E_m(r = R, \theta), \qquad (2.9)$$

where $E_p = -\partial\varphi_p/\partial r$ and $E_m = -\partial\varphi_m/\partial r$ denote the normal electric field components in the dielectric sphere and fluid medium respectively. Combining Equations 2.6 and 2.7 with Equations 2.8 and 2.9, the two unknown coefficients A and B can be obtained as [9]:

$$A = \frac{3\varepsilon_m}{\varepsilon_p + 2\varepsilon_m} \, E_0 \qquad \text{and} \qquad B = \frac{\varepsilon_p - \varepsilon_m}{\varepsilon_p + 2\varepsilon_m} \, R^3 \, E_0 \qquad (2.10)$$

The electric potential, Φ_{dipole}, as a result of a point dipole with a moment of P_{eff} in a dielectric solution of permittivity ε_m can be expressed as:

$$\Phi_{dipole} = \frac{P_{eff} \cos\theta}{4\pi\varepsilon_m r^2}, \qquad (2.11)$$

Combining Equation 2.10 with Equation 2.7, and comparing the induced dipole term of Equation 2.7 with Equation 2.11, the dipole moment of a homogeneous, dielectric sphere can be expressed as:

$$P_{eff} = 4\pi\varepsilon_m R^3 f_{(CM)} E, \quad \text{where} \quad E = E_0 \text{ and } f_{(CM)} = \frac{\varepsilon_p - \varepsilon_m}{\varepsilon_p + 2\varepsilon_m} \qquad (2.12)$$

where $f_{(CM)}$ is known as the Clausius-Mossotti factor. It is clear that, from the $f_{(CM)}$ expression, when microparticle permittivity is less than that of the fluid, $\varepsilon_p < \varepsilon_m$, the value of $f_{(CM)}$ becomes negative. The converse of this is that when microparticle permittivity is higher than that of the fluid, $\varepsilon_p > \varepsilon_m$, $f_{(CM)}$ becomes positive. If the

limits are taken with $\varepsilon_p \to \infty$ and $\varepsilon_m \to \infty$, then $f_{(CM)}$ is bounded by 1 and -0.5. It is clear that even when $\varepsilon_p \to \infty$, the magnitude of the induced dipole moment is finite.

Substituting the dipole moment expression of a sphere, Equation 2.12, back in Equation 2.5, the DEP force can be written as:

$$F_{DEP} = 4\pi\varepsilon_m R^3 f_{(CM)} (E \cdot \nabla)E, \tag{2.13}$$

Using vector quantity[†1], and based on the fact that the electric field is irrational where curl is equal to zero everywhere[†2], yields:

$$F_{DEP} = 2\pi\varepsilon_m R^3 f_{(CM)} \nabla E_{rms}^2 \tag{2.14}$$

where (rms) denotes the root-mean-square. So far, the behaviour of the microparticles in an electric field have been presented. There is however, significantly, the case of microparticles in a sinusoidal AC electric field, as presented in the next section.

[†1] $\nabla(A \cdot B) = (A \cdot \nabla)B + (B \cdot \nabla)A + B \times (\nabla \times A) + A \times (\nabla \times B)$

[†2] $\nabla \times A = 0$

2.3.2 Dielectrophoresis in an AC electric field

To determine the expression of DEP force for a uniform sphere placed into a sinusoidal AC electric field, applied potential of a single angular frequency ($\omega, where\ \omega = 2\pi f$) is considered. In such a case, the electric field can be represented as [9],

$$E(r,t) = Re[\bar{E}(r)e^{j\omega t}], \tag{2.15}$$

where $j^2 = -1$, r denotes the position at time t, and the symbols $Re[...]$ denotes a real part of the quantity to be used. $\bar{E}$ denotes the complex corresponding electric field phasor, which contains spatial information on the field intensity and polarisation, $\bar{E}.e^{jwt} = \bar{E}(cos\omega t + jsin\omega t) = Re[\bar{E}] + \text{Im}[\bar{E}]$, where Im denotes the imaginary part, and is typically used for travelling wave DEP [9]–[12]. In this work, the phase remains the same across the system; therefore, the field phasor can be taken to be the real part only without any loss of generalisation. Similar derivation and the same basics used in the previous section have been performed to derive a more general expression of the DEP force on a dielectric spherical microparticle, except that, in the following, the microparticles and the fluid medium have non-zero dielectric conductivities of σ_p and σ_m respectively, in addition to their dielectric permittivities. The solution forms for the potential inside and outside the microparticle, Φ_p and Φ_m, respectively, can be adopted while assuming that the constants, A and B, in the expressions are complex, $\bar{A}$ and $\bar{B}$, respectively. Therefore, the boundary condition for the potential at the surface of the microparticle remains the same in its form $\Phi_p(r = R, \theta) = \Phi_m(r = R, \theta)$. However, Equation 2.9 needs to be replaced by a charge continuity condition [9]. The general boundary condition of a free surface charge can be written as [9]:

$$\sigma_{surf} = \varepsilon_m E_{r,m} - \varepsilon_p E_{r,p}, \qquad at\ r = R \tag{2.16}$$

With finite conductivity and an AC electric field, the free electric surface charge σ_{surf} becomes non-zero and time-dependent; as the charge conservation condition is given by:

$$J_{r,m} - J_{r,p} + \frac{\partial \sigma_{surf}}{\partial t} = 0 \qquad at\ r = R \tag{2.17}$$

where $J_{r,m} = \sigma_m E_{r,m}$ and $J_{r,p} = \sigma_p E_{r,p}$ are the normal component of the Ohmic current density inside the fluid medium and dielectric microparticle, respectively. If the approximation of the exponential time dependence for all variables is assumed and

then the approximation $\partial/\partial t = jw$ is used as in [9], the new boundary condition can be expressed as:

$$\bar{\varepsilon}_m E_{r,m}(r = R, \theta) = \bar{\varepsilon}_p E_{r,p}(r = R, \theta) \tag{2.18}$$

Equation 2.18 is seen to have the same appearance as Equation 2.9, except for the use of a form of complex dielectric constants where $\bar{\varepsilon}_m = \varepsilon_m + \sigma_m/j\omega$ and $\bar{\varepsilon}_p = \varepsilon_p + \sigma_p/j\omega$. Therefore, the solution coefficients can be directly written as:

$$\bar{A} = \frac{3\bar{\varepsilon}_m}{\bar{\varepsilon}_p + 2\bar{\varepsilon}_m} E_0 \qquad \text{and} \qquad \bar{B} = \frac{\bar{\varepsilon}_p - \bar{\varepsilon}_m}{\bar{\varepsilon}_p + 2\bar{\varepsilon}_m} R^3 E_0 \tag{2.19}$$

Now, using the above results, a more general form for the complex version of the effective dipole moment can be expressed as:

$$\overline{P}_{\text{eff}} = 4\pi\varepsilon_m [f_{(CM)}(\omega)] R^3 E_0 \tag{2.20}$$

where

$$f_{(CM)}(\omega) = \frac{\bar{\varepsilon}_p - \bar{\varepsilon}_m}{\bar{\varepsilon}_p + 2\bar{\varepsilon}_m}. \tag{2.21}$$

The Clausius-Mossotti factor, in the previous expression, becomes a function of the complex quantities, where the normal boundary condition has been employed. Noting that the factor ε_m in Equation 2.20 is not complex. This is so the identification of the induced dipole moment is based on the relationship of charge to the applied electric field.

In moving toward the real time-averaged DEP force for a complex result, $\langle F_{DEP}(t) \rangle$, the phasor notation time dependent dielectrophoretic force can be used, where $(F_{DEP}(t) = Re[\overline{P}e^{j\omega t}] \cdot \nabla Re[Ee^{j\omega t}])$, and then, by taking the average over time, $\langle F_{DEP}(t) \rangle = \frac{1}{2} Re[\overline{P}e^{j\omega t} \cdot \nabla E^*]$, wherein the symbols $\langle...\rangle$ and $(*)$ denote the time-averaged and complex conjugate of that quantity respectively, the result is

$$\langle F_{DEP}(t) \rangle = 2\pi\varepsilon_m R^3 Re[f_{(CM)}(\omega)] \nabla E_{rms}^2 \tag{2.22}$$

A close inspection of Equation 2.22 reveals all the important key parameters in determining the DEP force for moving particles in suspension [2], [9], [11], [13]–[16]. The first is the gradient of the electric field magnitude squared ∇E_{rms}^2; therefore, it is clear that the DEP force is present only if the applied field is inhomogeneous. The second is the microparticle volume; the DEP force increases as the 3rd power of the

microparticle radius, R^3, radius (proportional to volume) and therefore, it is relatively easy to focus or position large microparticles in a capillary fill driven microsystem using relatively lower voltages, it is the compensation of microparticles radius and its surface conductance (Section 2.3.3). This is with the assumption that both microparticles are suspended and being carried by the fluid, and hence they will have the same velocity of the fluid in flow. The third factor is the real part of the CM factor and therefore the permittivity and conductivity of both the fluid medium and the microparticle, as well as the frequency of the applied AC field. In reality, its sign and magnitude determine the sign and magnitude of the DEP force [17]–[19], as introduced in the following section.

2.3.3   The Clausius-Mossotti factor

The direction of the DEP force does not depend on the polarity of the applied electric field [20]. Its direction depends on the sign of the Clausius-Mossotti (CM) factor [13], [15], [16], [21], which is a frequency dependent complex number, as seen from its mathematical representation form, Equation 2.21. The complex CM factor can also be written as:

$$f_{cm}(\omega) = \frac{(\sigma_p-\sigma_m)+(\varepsilon_p-\varepsilon_m)j\omega}{(\sigma_p+2\sigma_m)+(\varepsilon_p+2\varepsilon_m)j\omega}, \qquad (2.23)$$

by extracting the real part of the CM factor, as the only relevant part in the time-dependent DEP force, for the reason stated earlier in this chapter (Section 2.3.2), we can arrive at,

$$Re\big[f_{(CM)}(\omega)\big] = \frac{(\sigma_p-\sigma_m)(\sigma_p+2\sigma_m)+(\varepsilon_p-\varepsilon_m)(\varepsilon_p+2\varepsilon_m)\omega^2}{(\sigma_p+2\sigma_m)^2+(\varepsilon_p+2\varepsilon_m)^2\omega^2}. \qquad (2.24)$$

From the above equation, it can be easily seen that the sign of the CM factor is determined by the permittivities of the microparticle and the fluid medium at high frequencies. However, it is determined by the electric conductivities at low frequencies.   When $\varepsilon_m > \varepsilon_p$ and $\sigma_p > \sigma_m$, the CM factor is negative at high frequencies and positive at low frequencies. This is reversed when $\varepsilon_p > \varepsilon_m$ and $\sigma_m > \sigma_p$. So, for the case where $Re\big[f_{(CM)}(\omega)\big] > 0$, if all other features remain the same, a microparticle feels a net force driving it to the regions of higher electric field strength, which is under the microelectrode in the proposed design (shown in Chapter 1, Figure

1-3), and the force is known as positive-DEP (p-DEP). Meanwhile, for the case where the $Re[f_{(CM)}(\omega)] < 0$, a microparticle feels a net force driving it away from regions of maximum electric field strength, and in the proposed design towards the centre of the channel, and the force is known as negative-DEP(n-DEP). Many cells show only n-DEP if suspended in a physiological fluid medium because both their effective permittivity and conductivity are lower than that of the fluid medium [22]. This would allow low stress on biological objects for manipulation purposes, as mentioned earlier in this chapter.

For the case where the microparticles are less polarizable than the fluid medium, the frequency response for some given input parameters is presented in Chapter 4, Figure 4-5. Clearly, the CM curves fall in the range $1 > Re[f_{(CM)}(\omega)] > -\frac{1}{2}$, or, put differently, they have two numerical regimes which are either positive or negative[23]. Based on these two limits, at a range of frequencies, the microparticle experiences n-DEP force, whereas it shows p-DEP response at another range of frequency. Between these limits, there is a transition regime where the DEP force falls to zero and switches signs. At one particular frequency, the polarizability of the particle becomes identical to the suspending fluid, which means there is no induced dipole and the force falls to zero. This frequency is known as cross-over frequency, and it is used to separate the mixture of different cells [20]. This critical angular frequency (ω_{cri}) can be found by equating Equation 2.24 to zero as follows [24] [25]:

$$\omega_{cri} = \left((\sigma_m - \sigma_p)(\sigma_p + 2\sigma_m) / (\varepsilon_p - \varepsilon_m)(\varepsilon_p + 2\varepsilon_m) \right)^{\frac{1}{2}}, \qquad (2.25)$$

From all the above, it should be noted that the CM factor and therefore, the cross-over frequency varies with the size of the microparticle as well [20][26]–[29]. Even though this may not be obvious in the previous equations, it is enclosed within the microparticle conductivity term due to the formation of the stern and diffuse layer around it [6] [26]–[29]. The overall conductivity for solid, spherical and homogeneous microparticles σ_p can be written by using the concept of surface conductance K_s as:

$$\sigma_p = \sigma_b + \frac{2K_s}{R}, \qquad (2.26)$$

the equation above shows that for micron-sized particles the surface conductance can dominate over the bulk conductance, and therefore the later value can be neglected ($\sigma_b \cong 0$). Hence, the electric conductivity of the polystyrene microparticles is different

for different sizes. In Figure 4-6, see chapter 4, the electric conductivity of the fluid is held constant, and the DEP response for different sized microparticles are plotted. The cross-over frequency shifts to the lower frequencies as the particle conductivity decreases (particle size increases) and vice versa. However, the simulation shows that the real part of the CM factor is constant and close to - 0.5 at frequencies in the MHz region.

From all of the above, in a non-uniform AC field, we can say that the interfacial layer occurring at the particle-fluid interface introduces an additional shell that has distinct electric properties. The importance of such a shell becomes significant for manipulating different sizes particles [8]. However, the interfacial effect may also arise at the interface between fluid-microelectrode surfaces and may lead to electrode polarisation. Such an effect can cause an electric potential reduction in the suspension of very low conductivity, lower DEP force felt by the particle and a reduction in the particle control capability [8], and hence this effect needs to be avoided. However, Gascoyne and Vykoukal 2002 [8] show that this effect only occurs at low frequencies, below about 15 kHz, and so it cannot cause problems in this investigation.

2.3.4   Scaling

Equation 2.22 shows that the DEP force is proportional to the gradient of the electric field squared, ∇E_{rms}^2. In the studied system, as mentioned earlier in this work, the non-uniformity of the AC electric field is defined by microelectrode design. While computer assisted simulations could be used to optimise design, given some of the uncertainties in parameter values I decided to experimentally adjust voltage and frequency to find a good DEP focusing force in the frequency range where the CM factor is ~ -0.5. To estimate a starting point, when using any microfluidic structure, the magnitude of ∇E_{rms}^2 can be determined using approximate analytical solutions. For example, the electric field generated by the proposed microelectrode can be approximated as that of a semi-infinite plate capacitor [29]–[32], in which the electrodes run from $x = -\infty$ to $x = 0$, for which the force in dipole approximation can be used to estimate the maximum value of the DEP force. Due to symmetry, for a homogeneous spherical microparticle pushing away from the microchannel sidewall

to the half distance $(H = \frac{a}{2})$, H, in our case, is the depth of the designed microchannel, in the plane between the two microelectrodes, the maximal DEP force it feels is [30]

$$F_{DEP_z}^{max} = \frac{27}{32}\pi^2\varepsilon_m Re\big[f_{(CM)}(\omega)\big]\frac{R^3}{a^3}U_{rms}^2, \qquad (2.27)$$

where U_{rms}^2 denotes the root mean square voltage, and the force itself is as a function of a distance z , where $z = ((4 - 2Ln(3))a)/6\pi$, far away from the edge of the microelectrode reported in [30].

In our case, and from simple scaling law, this means that the DEP force scales more strongly with a. Increase in the applied voltage by a factor of 2 increases the DEP force by a factor of 4; however, doubling the microelectrode gap reduces the force by a factor of 8. Experimentally, we fabricated a 3D microchannel with a smaller cross section (50×27) that still allowed a range of polystyrene microparticles to be tested. However, to reduce the probability of channel blockage, as well as to provide a platform for a higher range of analytes to be tested, subsequently the channel cross section was increased to 60 µm in width and about 30 µm in height, as the maximum cross section which could be achieved while still being able to highly focus the smallest microparticle of interest into a single stream to the centre of the microchannel. This is based on the highest AC potential with a stable signal at which the in-house made voltage amplifier can be used to power the microdevice.

The ultimate goal of this work is to produce an integrated microchip-based flow cytometry to closely mimic the functionality of conventional flow cytometers. As far as possible, all three main components in flow cytometer need to be integrated into a single chip. Thus, by incorporating DEP transport mechanisms with a capillary fill driven system, the device would provide reliable analytical information even though the flow rate itself is not precisely controlled. If a sufficient n-DEP force can be achieved during the transition time of the microparticle through the microelectrode section, the movement of the microparticles might remain within the same streamlines as they were under the effect of n-DEP, downstream where the laser/photo-detector is, due to the laminar flow.

Ideally, the n-DEP force on a microparticle flowing under capillary action has to be greater than, for example, the hydrodynamic drag force; otherwise, microparticle focusing will not be achieved. Therefore, it is important to understand how the flow

behaves under capillary action to understand the microparticles' distribution and their relative velocity variations within the fluid flow, as presented in the next section. Note, gravity is ignored, as it is of little or no effect for most applications involving microsystems.

2.4   Particle motion in a capillary fill fluid delivery system

In the studied design (shown in Chapter 1, Figure 1-3), a liquid drop is deposited at the inlet reservoir, where it is pulled into the microchannel by capillary action. Simply, capillarity can be defined as an autonomous flow of fluid in narrow channels. The pressure difference between the initial and final part of the capillary is responsible for the fluid motion. In a microsystem like the one we designed, and also at low velocities, the Reynold number R_e, is very low and consequently, the fluid can be considered as a laminar flow. R_e, compares the effect of the body force of fluid to that of viscosity and can be given as $R_e = (\rho D_h v) / \mu$, where ρ is the fluid density, D_h, where $D_h = \frac{2hw}{h+w}$, is the hydraulic diameter of the rectangular capillary, usually lower than 1 for microfluidic channels, v is the average fluid velocity, and μ is the dynamic viscosity. Therefore, the very low R_e signifies viscous forces that tend to dominate over inertial forces and factors such as surface tension and fluidic resistance [33]. Thus, during the time frame of an experiment, although the flow rate through the microchannel is not controlled, a significant change in the microparticle velocity as it flows within the microchannel can only occur from a change in the forces acting upon it. Therefore, if we can measure the velocity of a microparticle as a function of distance or time, we will be able to measure the force acting on it. In particular, during the time course of an experiment, we can say that in a capillary system a microparticle will always travel at a constant velocity under a constant force field.

For a homogeneous sphere suspended in a viscous fluid, the hydrodynamic drag force acting on it is characterised by Stoke's law as follows:

$$\vec{F}_{HD} = 6\pi\mu R(\vec{v} - \vec{v}_P),   \quad (2.28)$$

where R is the microparticle radius, $\vec{v}_P$ is the microparticle velocity and v is the fluid velocity. Ideally, the particles suspended in, for example, a fluid of water-like density and viscosity will have the same velocity as their carrier. However, this is not the case in the presence of external forces such as DEP [34]. In the studied design, the forces

that tend to dominate on a microparticle flowing through the focusing microelectrode are the viscous force and electrical or DEP force, as shown in Figure 2-3.
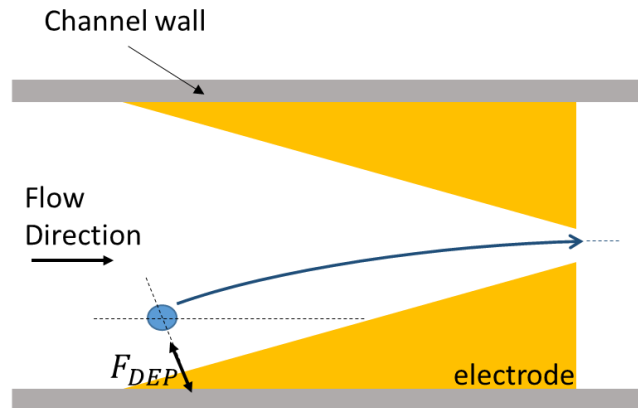
Figure 2-3 The forces acting on a microparticle in flow through focusing microelectrode.

During flow through the DEP focusing section, if the generated n-DEP force is strong enough to overcome the drag force, then the microparticle will be repelled from the electrode edge and move toward the centre of the microchannel. Ideally, this changing direction of a moving particle from a reference frame causes the particle to slow down in the stream direction z, but this is not easy to observe. Within the time course of our experiments, this effect is evident by comparing the velocity distribution of microparticles in flow through different regions along the length of the microchannel, the result of which is presented in Chapter 5. In addition, because the designed microelectrode is angled, the particle will continue travelling in the direction of the parallel component of the hydrodynamic drag force. In theory, the change in microparticle average velocities appears to be relative to its original position in the microsystem. This is also has been introduced in chapter 5. Therefore, to understand the working principle of typical capillary driven microsystems, it is crucial to understand the basic concepts and parameters that support their functionality, as presented in the following sections.

2.4.1   Capillary induced pressure and capillary force

As mentioned earlier in this chapter, the microfluidic device in this work is a pump-free capillary driven system. In other words, the surface tension is the only force drawing the fluid into the microchannel. This self-propelling phenomenon is a result of the pressure drop at the front end of the meniscus. Such a value of pressure can be

driven from the energy changes in the triple (liquid-solid-air) interface line. Figure 2-4 shows a configuration of a capillary fill microchannel with the front triple interface line of flowing fluid.
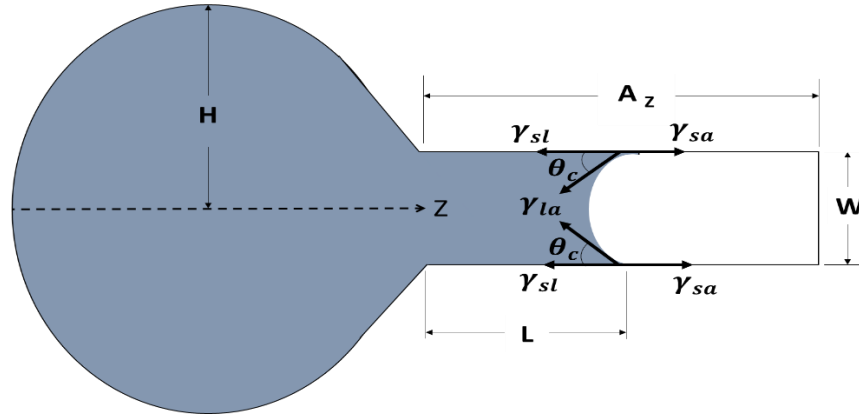
Figure 2-4 A schematic of a liquid front in a hydrophilic microchannel, top view.

The total surface energy of such a system is given by [35], [36]:

$$E_T = A_{sl}\gamma_{sl} + A_{la}\gamma_{la} + A_{sa}\gamma_{sa}, \tag{2.29}$$

The symbols A_{sl}, A_{la}, and A_{sa} refer to the solid-liquid, liquid-air, and solid-air interface areas, and γ_{sl}, γ_{la}, and γ_{sa} are its corresponding three surface tensions satisfying Young's law as [37]:

$$\gamma_{sa} = \gamma_{sl} + \gamma_{la}\cos\theta_c, \tag{2.30}$$

where θ_c is the contact angle between the liquid and the walls of the microchannel. Therefore, using Equation 2.30 in Equation 2.29 yields

$$E_T = E_0 - A_{sl}\gamma_{la}\cos\theta_c + A_{la}\gamma_{la}, \tag{2.31}$$

where E_0, $E_0 = (A_{sl} + A_{sa})\gamma_{sa}$, is the surface energy stored in the filling reservoir, and it is constant, since the sum ($A_{sl} + A_{sa}$) remains unchanged. Taking the derivative of Equation 2.31 as a function of the volume V_l filled by the fluid in the channel, the capillary pressure (P_{cap}) can be expressed as [33], [35]:

$$P_{cap} = -\frac{dE_T}{dV_l} = -\gamma_{la}\left(\cos\theta_c\frac{dA_{ls}}{dV_l} - \frac{dA_{la}}{dV_l}\right), \tag{2.32}$$

The equation above shows how spontaneous filling of a liquid inside a microsystem occurs as long as the capillary induced pressure is negative, which is true if the term

between the brackets is positive [33]. In other words, the spontaneous capillary driven flow occurs when

$$\frac{dA_{la}}{dA_{ls}} < \cos\theta_c \tag{2.33}$$

Assuming a homogenous confined microchannel, as is the case with the studied 3D microchannel, the liquid-air interfacial surface area remains unchanged with the advancing fluid front in the channel, and hence $\left(\frac{dA_{la}}{dV_l} = 0\right)$, while the solid-liquid interfacial surface area increases linearly with liquid travel distance Z along the axial direction of the capillary system. Thus, Equation 2.32 can be expressed as follows [38]–[41]:

$$P_{cap} = -\gamma_{la}\left(\cos\theta\frac{\frac{dA_{ls}}{dZ}}{\frac{dV_l}{dZ}}\right) = -\gamma_{la}\left(\cos\theta\frac{\frac{2(W+H)dZ}{dZ}}{\frac{HWdZ}{dZ}}\right)$$

$$P_{cap} = -2\,\gamma_{la}\cos\theta\left(\frac{1}{H}+\frac{1}{W}\right), \tag{2.34}$$

where H and W denote the height and width of the microchannel, respectively. From Equation 2.34, the capillary pressure is affected by both the surface tension and contact angle. The angle in these equations is the generalized Cassie angle. It is the average contact angle between the advancing fluid front and capillary walls. This angle may vary during the early stages of the meniscus development [42] and can also vary with the size of the capillary driven flow: however, it was mentioned that this value seems to be almost constant for sizes less than 80 µm [38], [43], [44]. In addition, since the capillary number is small (e.g. $C_a < 10^{-3}$, where $C_a = \mu V / \gamma$, and V is the mean fluid velocity [45]), the advancing contact angle is constant and the same as the static one [41]. In addition, the capillary pressure equation shows that the smaller the channel dimension, the larger the pressure drop at the capillary interface.

For a confined rectangular cross-sectional microchannel, the capillary force applied on the fluid column along the flow direction is expressed as the capillary pressure times the unit area:

$$F_{cap} = P_{cap}\text{HW} = 2\,\gamma_{la}\cos\theta(H+W), \tag{2.35}$$

From the above equation, the driving capillary force can be written in the form of free p_F and wetted p_w perimeters, which are the length of the fluid front not in contact with walls in a cross section and the length of the contact line between the fluid and the solid in the same cross section, respectively. Also, if an open channel (a free boundary with air) is considered, then ($\frac{dA_{la}}{dV_l} \neq 0$, Equation 2.32) and the capillary force can be written as follows [41], [42], [45], [46]:

$$F_{cap} = \gamma(p_W \cos\theta - p_F), \qquad (2.36)$$

where $p_w = 2(H + W)$. The above equation shows that the condition of spontaneous capillary fill can be met as long as $p_F/p_W < \cos\theta$ or the contact angle is less than $\frac{\pi}{2}$ [42], [45], [47]. Another way of looking at this is to say that this 'packed in' force will keep advancing the fluid through the microchannel as long as there are walls to be wetted, or until the increasing resistance at the polymeric microchannel walls stops it [48]. This is based on the assumption that there is enough liquid in the inlet reservoir. In the next section, the viscous drag force is introduced.

2.4.2 Viscous drag force

As we mentioned earlier, the pressure difference at the front end of the meniscus works as an intrinsic pumping force for the fluid and set it into motion. With time t, the increasing fluid length within the microchannel encounters resistance to fluid penetration. This resistance is a function of the average velocity V and the total length of the fluid column Z. Hence, the viscous drag force F_D can be expressed as [41]:

$$F_D = R_T(Z, V), \qquad (2.37)$$

The total resistance to the flow R_T comes from the wall shear stress, therefore by integrating the friction acting to the wall area, F_D can be expressed as:

$$F_D = \tau S = \int_0^z \tau p_W dz = \tau p_W Z(t), \qquad (2.38)$$

where S denotes the wetted surface between the origin and the front end of the meniscus. Wall friction on a capillary wall can be expressed in terms of the average velocity as[41][47]:

$$\tau = \mu \, \partial V / \partial y = \mu \, V / \lambda, \tag{2.39}$$

where λ denotes the friction length and y the coordinates perpendicular on the channel walls, which depends on the capillary geometry. Note, μ denotes the fluid's viscosity and is constant for a Newtonian fluid.

For the studied design, due to the mixture of the open and 3D microchannel, the advancing interface is expected to pass through various geometries, changing values of the cross-sectional area S_i where $(i = 1, \dots, n)$. Hence, the wall friction on the fluid will be the sum of the friction in all these various sections, and can be written as[42], [46]:

$$F_{D,K} = \sum_{i=1}^{K-1} F_{D,i} + \mu \frac{V_K}{\lambda_K} (Z - Z_{K-1}) p_{WK}, \tag{2.40}$$

where Z is the location of the advancing end of the fluid front, V_K is the mean velocity in section K that varies with Z from the beginning to the end of each section, Z_{K-1} is the distance from the channel's inlet to the end of section K-1. Advancing further along the microchannel, Equation 2.40 can be written to take the general form of [42], [46]:

$$F_{D,K} = \sum_{i=1}^{K-1} \mu \frac{V_i}{\lambda_i} \Delta Z_i p_{Wi} + \mu \frac{V_K}{\lambda_K} (Z - Z_{K-1}) p_{WK}, \tag{2.41}$$

Where $\Delta Z_i = Z_i - Z_{i-1}$ denotes the length of section i. In theory, this expression shows that the larger the friction length for a given cross section, the lower the friction force. However, this statement does not translate directly to a rise in the force that drives the flow. A large friction length is not associated with a large wetted perimeter [47]. Hence, for the fluid to induce inside the capillaries as desired, a compromise between the two opposing effects of capillary force and wall friction needs to be taken into account.

In the case of a confined rectangular microchannel, the average friction length $\bar{\lambda}$ can be written in the terms of the hydraulic resistance $\tilde{R}_H$ and wetted perimeter as follows,

$$\bar{\lambda} = \mu \frac{p_W}{\tilde{R}_H S_c}, \tag{2.42}$$

where $S_c = hw$ is the cross-sectional surface area, and the hydraulic resistance per unit length is governed by:

$$\tilde{R}_H = \frac{4\mu}{h^2}\left[\frac{1}{3} - \frac{64}{\pi^5}\frac{h}{w}\tanh\frac{\pi}{2(h/w)}\right]^{-1}, \qquad (2.43)$$

Equation 2.41 also shows how the friction increases as the fluid advances along the channel. This will reflect on the fluid velocity, causing it not only to slow down but also changes the distribution of fluid velocity across the channel, becoming faster at the centre, as discussed in the next section.

2.4.3 Dynamics of capillary driven flow

The motion of the fluid in a capillary can be explained by considering the balance of forces in the capillary. Thus, the governing forces acting on the fluid flow can be given by[41], [45], [47], [49], [50]:

$$(M_a + \rho AZ)\frac{dV}{dt} = \gamma P_W \cos\theta - R(Z,V) \qquad (2.44)$$

The above equation physically represents the Newtonian equation of fluid motion in a capillary. The first and second term on the right-hand side represent the capillary force and viscous drag force, respectively. The term ρAZ represents the mass of the fluid as proportional to the travel distance Z, with ρ indicating the density of the fluid and A denoting the cross-section area. M_a is the added mass coming from the additional fluid entering the microchannel during displacement. From the previous equation, it can be seen that in geometries with a constant cross section, the capillary filling by the pull of the surface tension remains constant. However, increasing viscous resistance with penetration at every point causes the fluid velocity to drop. Washburn in 1921 [51] made a great attempt to understand the fluid flow in capillaries for practical applications. Using the balance of forces in a cylindrical capillary, which can be applied to any capillary system, his equation states that the interface line position is proportional to the square root of time. Recently, special attention has been given to estimating the influence of viscous resistance in the flow's velocity and the velocity profile changes slightly further downstream in capillaries. For example, Wei et al. 2001 [49] have carried out a simulation analysis that shows the velocity profile into a capillary from a droplet. Ideally, at the entry section and immediately before the drop of liquid enters the microchannel, $Z = 0$ when $t = 0$, the liquid is not subjected to friction at the walls. Therefore, the flow can be considered as an irrational or potential

flow with vanishing velocity far away from the entrance. As mentioned earlier in this work, when the drop of liquid touches the microchannel, the flow is influenced by the surface tension. The first action of the surface tension is to take the shape of a curved meniscus. At the front end of the meniscus, the average velocity is equal to:

$$V(t) = \frac{dZ}{dt}, \tag{2.45}$$

when t is small, Z and V are small, Equation 2.44 can be expressed as:

$$M_a \frac{dV}{dt} = \gamma P \cos \theta, \tag{2.46}$$

taking the integration of Equations 2.46 and 2.45 for a very small time, for example at $0 \leq t \leq t_1$, yields

$$V = \frac{\gamma P \cos \theta}{M_a} t,$$

$$\tag{2.47}$$

$$Z = \frac{\gamma P \cos \theta}{2M_a} t^2,$$

The relations above show the importance of the finite added mass, for example, if $M_a = 0$, the initial acceleration would be infinite, and the beginning of the motion would be indeterminate. While with a finite value of M_a, the initial velocity is zero, V increases with t, and Z increases with t^2. However, when t and Z increase, viscous resistance at the wall comes into play, causing acceleration to decrease. The acceleration becomes zero when the right-hand side of Equation 2.44 vanishes: let us say at t_2. Then, at $t > t_2$ the acceleration can be negative. This is the time period where the high-speed camera used cannot observe or record useful information, as discussed in the following chapter. Then, as the fluid advances, it is apparent that the flow would be subjected to additional local resistance further downstream which would change its velocity profile. In other words, considering the balance of forces in the system, the capillary force might only present at the fluid front, so that behind the advancing meniscus, the fluid flow and so the suspended microparticles become faster at the centre of the capillary fill fluid delivery system due to the greater friction at the side walls. The result achieved are presented in Chapter 5.

Few theoretical studies have been made to estimate the development of flow in the entry region of either circular or narrow rectangular capillaries and changes in velocity

vectors downstream [52][53][49]. For example, Wei et al. [49] have suggested that the flow developed in a microchannel can be divided into three different regimes based on the assumed behaviour of surface tension and classical flow mechanics. The suggested regions are; i) entry regime, ii) Poiseuillean regime and iii) surface traction regime, and the length of these regions are denoted by L_3, L_2 and L_1, respectively.
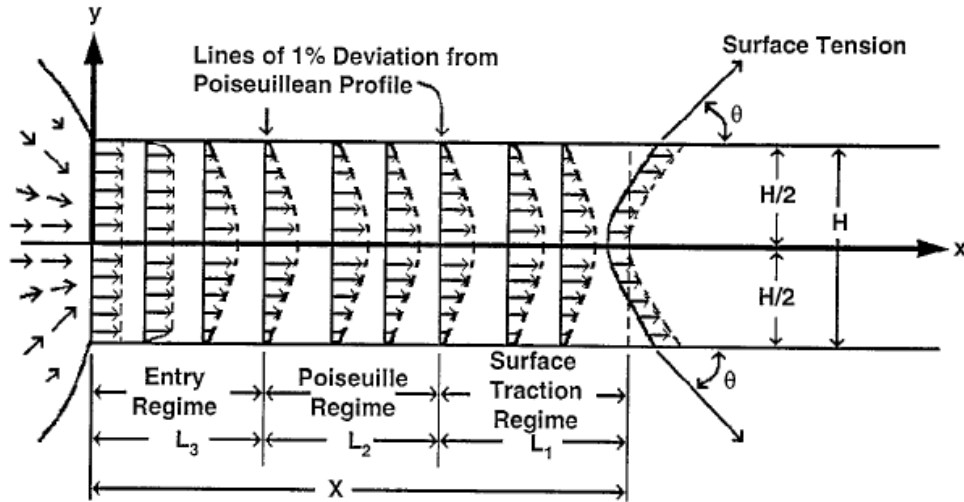
Figure 2-5 changes of velocity profile in flow into a microchannel from a droplet with a dimensionless downstream distance [49].

When a fluid comes into contact with a microchannel with hydrophilic walls, the first action is to create the meniscus profile. At this stage, the entry and surface traction regimes interact together. Then, as the fluid advances to the right, the so-called poiseuillean region starts to come into play, as shown in Figure 2-5, and it needs to be considered. The Poiseuillean region as reported in Wei et al.'s work is expected to start when the location of the general section x is bigger than 0.7 times the half thickness of a rectangular channel, $x > 0.7 \left(\frac{H}{2}\right)$, and ends when $2x/H > [(2X/H) - 0.7]$, where X is the total length of the fluid column in the microchannel. If X/H lies between 0 and 0.7, then there is no Poiseuillean region, $L_2 = 0$, and the entry region and the meniscus traction region interact together. Thus our experimental work presented in Chapter 5 reveals good agreement with the theoretical work reported in Wei et al [49], that the microparticles are flowing faster in the centre of the capillary microsystem.

2.5   Laser source and detector

Since the invention of the laser in the 1960s, lasers have become the light source for conventional and most commercial optical on chip flow cytometers, mainly because they are monochromatic, coherent and provide a high-quality beam profile. The predictable excitation beam shape makes it easier to provide a predictable and highly reliable detection signal intensities across the sample stream, which is of fundamental importance for optical excitation and detection in flow cytometer applications. Each different sample's characteristics will interact with the light differently. Being able to detect this interaction (unique optical signature) will allow unique conclusions about the analyte of interest to be made.

Monolithically integrated strategy aims to facilitate the complete system on single board or substrate, so the final microfluidic device would have a small form factor and portability. By using a compound semiconductor, the optically active region on the substrate can consist of many layers of epitaxial growth that encompass a wide range of functionalities that include, for example; light source, amplifier and detector. Therefore, it is essential to understand the general principles of semiconductor lasers, as presented in the following section.

2.6   Basic principles of a laser diode

2.6.1   Components of a laser

The three fundamental elements that should be available to produce a laser, as shown in Figure 2-6, are; i) a gain medium that is capable of amplifying the incident light by stimulated emission (see the next section), ii) a pump source, either electrically or optically, to achieve amplification rather than absorption, and iii) a laser resonator to ensure the probability of stimulated emission is great than the probability of spontaneous emission by increasing the light level in the material.
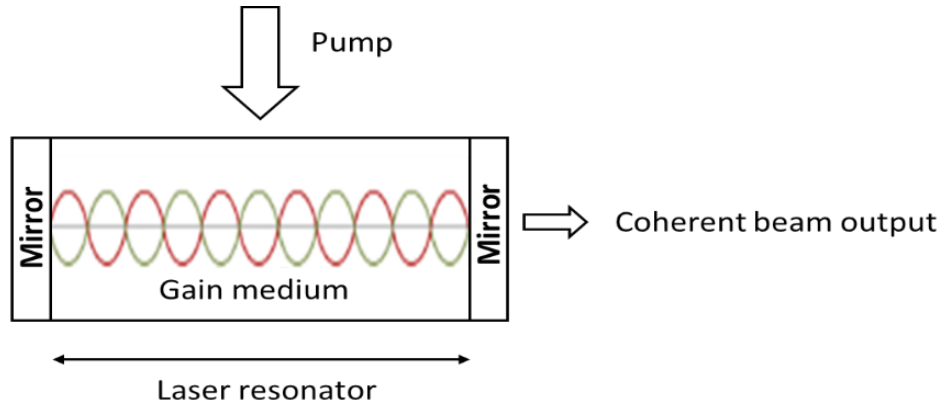
Figure 2-6 Illustration of the essential components of a laser diode; the gain medium, the pump source and the resonant cavity. At each end of the active medium, there is a mirror, which is formed by the cleaved or here etched semiconductor to air / liquid interface. The mirrors are partially reflecting, which allow some of the coherent light to be emitted.

The gain in light intensity is fundamental to overcome the losses generated by the resonant cavity and for any laser output to be produced. The optical modal gain (G) can be defined as the fractional increase in the energy in a light beam, E, per unit distance travelled through the medium, L [54]:

$$G = \frac{1}{E}\frac{\Delta E}{\Delta L},$$ (2.48)

where $E = N_P h\nu$, $h\nu$ is the photon energy (h is Planck's constant ($6.626 \times 10^{\wedge 34}$ m^{2}Kgs^{-1}) and ν is the frequency of the resulting photon), N_P is the number of photons and ΔE is the increase in energy that only occurs in the quantum well layer. The experimental devices in this work were fabricated from III-V quantum well (QW) semiconductor material. QW structures reduce the dimensional form of the system from three to two dimensions, since they perform quantization in the normal direction to the surface of the layer. The following sections provide a brief description of the fundamental components of the laser diode.

2.6.2   Einstein absorption, spontaneous and stimulated emission

In semiconductors, three important radiative transitions can take place between high and low energy bands within the crystal that produces photons. These three processes, which involve absorption, spontaneous and stimulated emission, are illustrated schematically in Figure 2-7.
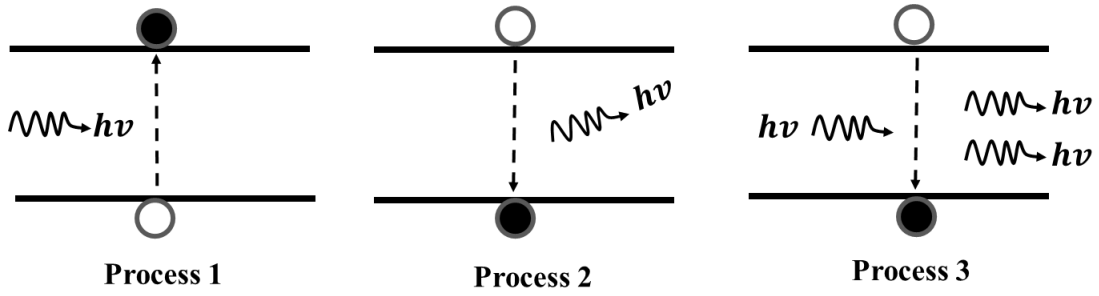
Figure 2-7 Illustration of the possible distribution of the electrons between two energy levels E_1 and E_2. The initial state of the electron is represented by a solid circle and the final state by an open circle.

In stimulated absorption, an incident photon is absorbed and results in the transition of an electron from the lower state E_1 to the upper empty state E_2, leaving a hole in the lower state (this process is used in the photo-detection of light). This gives an absorption total rate of [55]

$$R_{12} = B_{12}f_1(1 - f_2)\rho(hv), \qquad (2.49)$$

where B_{12} is the transition probability (a measure of the strength of electron-photon interaction), f_1 is the number of electrons in the lower energy level, $1 - f_2$ is the number of empty states in the upper energy level and $\rho(hv)$ is the density of photons per unit volume at $hv = E_2 - E_1$.

In spontaneous emissions, which are shown as process 2 in Figure 2-7, an electron occupying an energy state at the upper level E_2 spontaneously falls down into a lower energy state E_1, even with the absence of an external trigger. The recombination of an electron-hole pair results in the spontaneous emission of a photon with a frequency corresponding to the energy difference between the two states $(E_2 - E_1 = hv)$. Whereas the frequency of the photon is well defined, its direction, phase and polarisation are random. The rate of this transition can be given as

$$R_{21}(spon) = A_{21}f_2(1 - f_1), \qquad (2.50)$$

where A_{21} is the transition probability of a spontaneous emission. From the above equation, it is clear that the spontaneous process is independent of the photon density within the system, and it is only dependent on the relative distribution of the electrons between states. In other words, this process is only controlled by the number of electrons in the upper state and available lower state empty of electrons.

In the case of stimulated emission, describing process 3 in Figure 2-7, incident photons induce downward electron transition. As with the spontaneous downward transition, as the electron recombines with a hole in the lower state it release its energy in the form of a photon. This time, the photon has the same phase and direction of travel as that of the started the transition. If these photons are stimulated further downward, the process results in coherent photons (this coherent amplification of light is the basis of laser action). The rate for this stimulated emission process is given by

$$R_{21}(stim) = B_{21}f_2(1 - f_1)\rho(hv), \qquad (2.51)$$

where B_{21} is the transition probability of a stimulated emission.

In equilibrium conditions, the rate of downward transition must be equal to the rate of upward transition so that,

$$R_{12} = R_{21}(spon) + R_{21}(stim). \qquad (2.52)$$

Where we have a number of states at the same energy, in for example the conduction band, the number of electrons becomes the probability of a state being occupied multiplied by the number of states. The probability of an electron occupying a state of energy E_n, in the conduction band (CB) or valance band (VB), at temperature T (K), can be given by Fermi-Dirac statistics:

$$f(E_n) = \frac{1}{1+exp\left(\frac{E_n - E_F}{K_B T}\right)}, \qquad (2.53)$$

where E_F is the Fermi energy (eV), and K_B is the Boltzmann constant (eV/K).

In thermal equilibrium, the fermi energy is close to the middle of the band gap, $E_g = E_c - E_v$. Since $E_g \gg K_B T$, there is a very small number of electrons in the CB compared to the VB. However, in order to achieve amplification of light as it propagates through the material, the stimulated emission rate must dominate over the absorption and spontaneous emission rates and a condition known as population inversion must be achieved. This means there must be more occupation probability of carriers in the upper level, f_2, than that of the lower one, f_1, or in other words, $f_2 > f_1$. Before returning to this we need to understand how population inversion is achieved.

2.6.2.1   The p-n junction semiconductor diode

A p-n junction diode is a two-terminal, positive and negative, semiconductor device, which allows the electric current flow in only one direction, while it blocks it in the reverse or opposite direction. If the diode is forward biased (negative to the n-side and positive to the p-side), it allows the electric current flow. On the other hand, if the diode is reverse biased, it blocks the electric current flow. The p-n junction semiconductor device is formed when a p-type and an n-type semiconductor material are joined to make one piece of the semiconductor.

The intrinsic semiconductor used to create n- and p-type material is doped with impure atoms that contribute free charge carriers to the crystal lattice. In the n-type, the Fermi level is close to the CB and the dopant atoms can donate free electrons to the CB. Alternatively, in p-type, the Fermi level is close to the top of the VB and the dopant atoms are able to accept holes from the VB. When the two materials are brought into contact with each other, free electrons and holes in the vicinity of the interface can diffuse across it and recombine with each other, leaving negatively charged donor ions on the n-material side and positively charged acceptor ions on the p-material side. The voltage difference of n- and p- sides produces a region depleted of any free charge carriers. The more charge carriers recombine, the greater the depletion region and thus the potential difference of n- and p-side material.

If no external voltage is applied and the system is in equilibrium, the Fermi level of each material is near the middle of the band gap. However, when an external forward bias is applied across the device, the potential energy of electrons on the n-side increases with respect to those on the p-side. This effectively separates the Fermi level of each and decreases the built-in junction potential. We now have two quasi fermi levels defined as E_{F1} and E_{F2} and since $f_2 > f_1$.

$$exp\left(\frac{E_2 - E_{F2}}{K_B T}\right) < exp\left(\frac{E_1 - E_{F1}}{K_B T}\right), \tag{2.54}$$

and this yields

$$\Delta E_F = E_{F2} - E_{F1} > E_2 - E_1 > h\nu. \tag{2.55}$$

This non-equilibrium condition is known as population inversion. It shows that for population inversion to occur, the quasi-Fermi level separation must be larger than the photon energy, $h\nu$.

This condition can be maintained by electrically injecting carriers into the semiconductor material through a p-n junction, as described above. Electrons and holes can now continuously move into this region where they are able to radiatively recombine by emitting a photon. These photons are released with energy hv. In order to achieve optical gain at photon energy hv, the quasi Fermi level separation produced by the applied potential must exceed that photon energy, as the condition set by Equation 2.55 [56].

2.6.3   Threshold gain and optical loss

For a semiconductor diode laser, the thin central region where population inversion occurs is the gain medium. The coherent amplification of light and the direction that characterises the stimulated emission are maintained within a laser chip by placing the gain medium inside an optical cavity. The optical resonator is formed by cleaving, or in our case, etching the semiconductor material along crystal planes to form two parallel facets with reflectivity (R_1 and R_2) to provide the optical feedback. Light circulating in a resonator without any optical gain will undergo losses due to all the optical losses that arise from absorption, scattering and etched facet surface roughness, in addition to mirror loss (α_m) during the round trip of the laser's optical resonator. However, as population inversion is produced in the material by pumping, the resultant gain begins to recompense for the loss. All losses except transmission through the mirrors are known as internal optical loss (α_i), which can be defined as the loss of light from the lasing optical mode of the laser as it propagates down the waveguide structure. When the optical gain of the laser medium matches the losses, then oscillation can occur, and lasing begins. Considering a beam of light of initial intensity I_0, as it propagates down the waveguide structure, as shown in Figure 2-8,
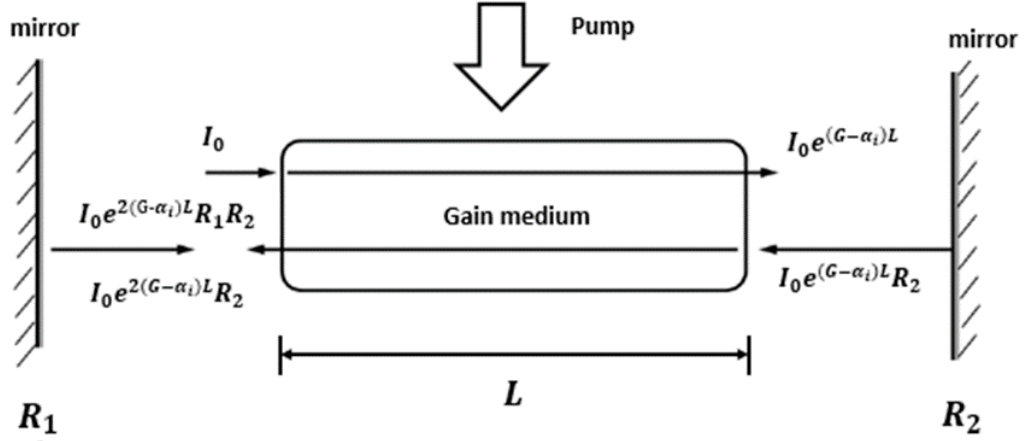
Figure 2-8 Schematic illustration of a round trip condition in the resonator cavity of a semiconductor laser where the net gain over each pass of the cavity equates to the light lost from the mirrors. Note that this set up for general laser but in a laser diode such us the one we build in this work the gain medium fills the whole of the space between the mirrors (the space between the etched facet)

it experiences a net gain, and the intensity can be written as:

$$I_0 exp(2GL),\qquad(2.56)$$

and after reflection from the right and left-hand mirror, the intensity becomes:

$$I_0 exp[2(G - \alpha_i)L]R_1 R_2.\qquad(2.57)$$

For steady-state operation, we require that there is no change after one round trip, so that

$$exp[2(G - \alpha_i)L]R_1 R_2 = 1.\qquad(2.58)$$

Solving the previous equation for G_{th}, modal gain threshold requirement for the device to just balance the total losses and to maintain laser action:

$$G_{th} = \frac{1}{2L}\ln\left[\frac{1}{R_1 R_2}\right] + \alpha_i = \alpha_m + \alpha_i,\qquad(2.59)$$

From the above equation, α_m is the mirror loss (the fraction of light that is lost purely due to facet reflectivity): however, this can only be seen as an approximation because the effect of spontaneous emission was ignored. It shows that the modal gain of the laser is dependent on the length of its cavity.

As mentioned earlier in this work, the two partially reflective parallel mirrors are created by chemically etching the substrate to produce a vertical profile. If the light is

at normal incidence to the mirror, then the reflectance (R) at one semiconductor-air interface can be written as[57]

$$R = \left(\frac{n_{sc}-n_{air}}{n_{sc}+n_{air}}\right)^2, \tag{2.60}$$

where n_{air}, $n_{air} = 1$ is the refractive index of air and n_{sc} is the refractive index of the semiconductor. Only light perfectly perpendicular to the axis of the cavity is restricted in its propagation on both sides of the active medium and it therefore propagates back and forth. The refractive index in Equation 2.60 can be replaced with those of other materials based on the type of interface.

2.6.4   Density of states and population of states

A quantum well is formed when the dimension of the semiconductor in one (the z-) direction is reduced to a thin sheet, then correspondingly the number of states available in the conduction and valence bands reduces to a set of discrete energy levels. In the K-space diagram, each allowed state in the well corresponds to a wavevector K, and since every K must have three components (K_x, K_y, K_z), in this sheet, an electron or hole wave propagating through the sheet has to have three components (K_x, K_y, K_z). The first component of K_z non-zero is $K_z(n = 1)$ where $(n = 1, 2, 3, ...)$, which means every K value that can be thought of must have one value of K_z (K_z =constant) but a very large number of allowed points (states) with different values of K_x and K_y,

$$K = K_x + K_y + K_z. \tag{2.61}$$

For simplicity, let $K_x + K_y$ be written as a transform single wavevector K_{xy} of the two components x and y in plane motion, so,

$$K = K_{xy} + K_z, \tag{2.62}$$

and energy (for the typical EK-diagram, every value of K there is a corresponding value of E):

$$E = E_{xy} + E_z. \tag{2.63}$$

The time independent Schrödinger equation can be used to determine the wave-functions, and the energy of the confined states in a QW can be written as [55],

$$E = \frac{\hbar^2 |K_{xy}|^2}{2m_w^*} + E_z, \tag{2.64}$$

where ℏ is the reduced Planck constant and m_w^* is the effective mass of the electrons or holes confined within the well, and

$$\left|K_{xy}\right|^2 = K_x^2 + K_y^2. \tag{2.65}$$

From equation 2.64 can be seen that there is a large number of degenerate states with different combinations values of K_x and K_y but the same value of $\left|K_{xy}\right|$ and E_{xy}. Due to relationship in Equation 2.62, these allowed states lie on a constant energy circle in the (K_x, K_y) plane with radius $\left|K_{xy}\right|$ and width $\Delta K_{xy}(\Delta K_{xy} \ll \left|K_{xy}\right|)$, as shown in the figure below.
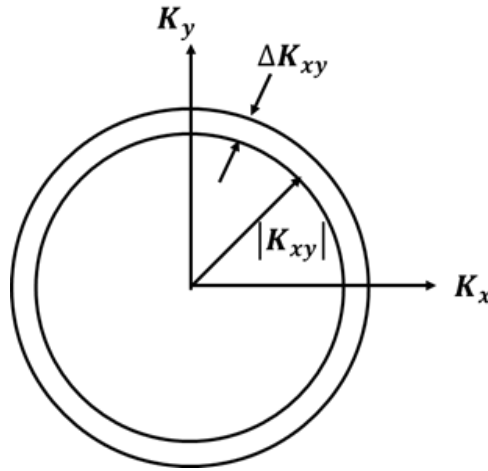
Figure 2-9 ***K*-space diagram of allowed states associated with electron motion in-plane represented by travelling waves. A large number of different states all have the same energy lie on a circle in the(K_x, K_y) plane with radius $\left|K_{xy}\right|$) and width ΔK_{xy}.**

Electron motion in the plane can be described by traveling waves in both positive and negative directions with cyclic boundary conditions, also known as Born-von Karman boundary conditions. These cyclic boundary conditions require an integer number (n), as are n_x and n_y, of the wavelength in the circumference of the circle that gives the allowed value of the K-vector for each direction, $K(n) = \mp n\frac{2\pi}{L}$. Therefore, the spacing of the allowed values of K_x and K_y can be written as:

$$\Delta K_x = \frac{2\pi}{L_x} \qquad and \qquad \Delta K_y = \frac{2\pi}{L_y}. \tag{2.66}$$

Each state therefore occupies an area in K-space of $(2\pi/L_x)(2\pi/L_y)$. The area of annulus in the K-space divided by area occupied by one state will give the number of states. Since the annulus is a full circle covering positive and negative components of

K_{xy}, with circumference $2\pi|K_{xy}|$, the number of states with energy E_{xy} can be written as:

$$N_{xy} = \frac{2\pi|K_{xy}|\Delta K_{xy}}{(2\pi/L_x)(2\pi/L_y)}. \tag{2.67}$$

Expressing the above equation in terms of energy, ΔE_{xy}, yields

$$N_{xy} = \frac{m_w^*}{2\pi\hbar^2}(L_x L_y)\Delta E_{xy}, \tag{2.68}$$

Multiplying Equation 2.68 by 2 to account for two degenerating states of opposite electron propagation at each energy level, this per unit ample area $(L_x L_y)$ per unit energy interval will give the density of states within one sub-band for both spins as:

$$\rho(E) = \frac{m_w^*}{\pi\hbar^2}. \tag{2.69}$$

From the above equation, the density of states in a quantum well is independent of energy. This contrasts with a bulk semiconductor material, where the density of states is proportional to the square root of the energy, $E^{1/2}$. Density of states can be calculated for both the conduction and valance bands, $\rho_c(E)$ and $\rho_v(E)$, by substitution of electron and hole effective mass, m_c^* and m_v^*, respectively for m_w^*. Summing the contributions from each of the available sub-bands produces a step-like function, as in Figure 2.10.
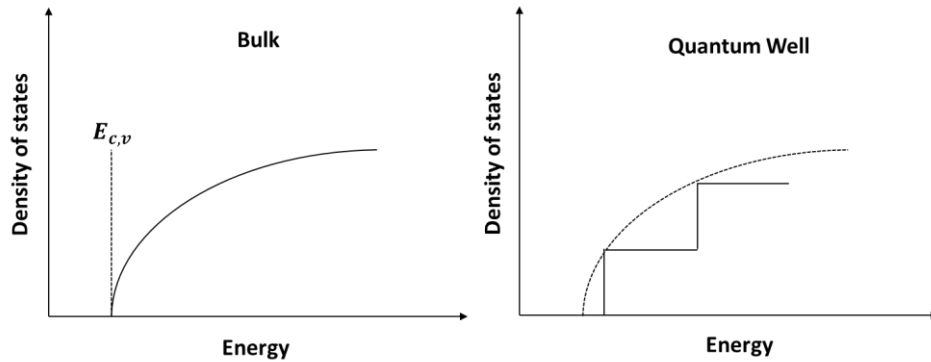
Figure 2-10 Schematic showing density of states for bulk semiconductor material and quantum well with confinement in one direction, z.

With the knowledge of the density of states, the carrier concentration $n(E)$ in the well can be determined by the available states $\rho(E)$ multiplied by the probability of occupation $f(E)$. The probability of occupation is given by the Fermi functions for conduction and valance bands. In a QW, the constant density of states results in carrier

probabilities that are higher at the edges of the conduction and valence bands compared to bulk materials. The decreased occupation of high above lying energy states narrows the spontaneous emission spectrum of the QW material. Consequently, QW lasers have lower threshold current densities in competition with that made from bulk semiconductors.

2.7   Light Scattering

2.7.1   Light scattering of microparticles

When a light beam strikes an object in a medium, light can be scattered or absorbed, or both, based on the wavelength of the light source and the optical characteristics of the material (see Figure 2-11). Scattering can be defined as the process where light is reflected off a sample's features due to the refractive index differences between the piece of matter and the surrounding medium.
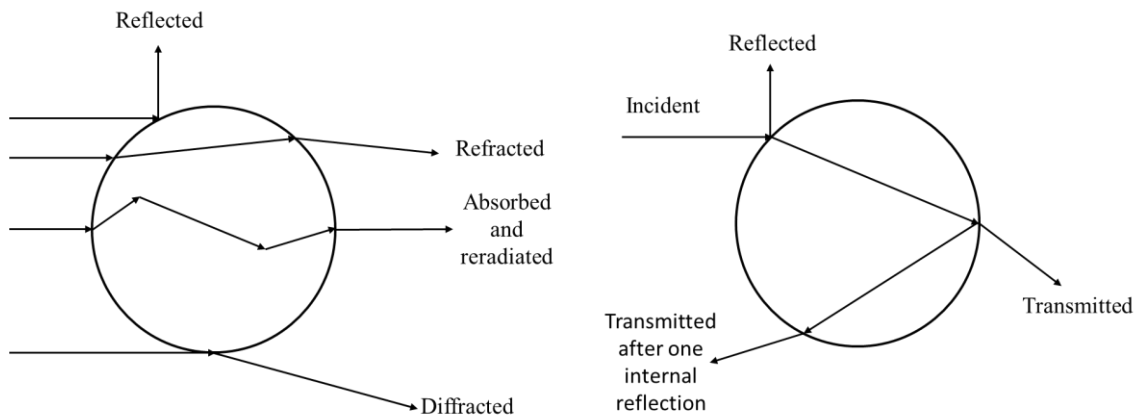
Figure 2-11 Ray tracing diagram

In this work, the designed microfluidic platform has considered laser/detection sections in-line for on chip small angle scattering measurements. The excitation laser beam and the fluidic microchannel have an intersect angle of 90^0. As a flowing microsphere that has been focused in a single stream, by the influence of applied DEP force, passes through the interrogation beam, scattered light from it will radiate at all angles. The surface of the sample (blood cells) that the device aims to analyse in the future is not a smooth surface, but instead it has a granular texture, and each different cell varies in terms of internal structure. Therefore, there will be many different points of reflection and the resulting scattering of light will be a complex process that needs

to account for all the refractive index contrasts in a sample as well as the different surface directions. However, in this work, polystyrene microbeads are used, and these microspheres are uniform, meaning that the scattering from each same-sized microparticle will be uniform as long as they are aligned in an equilibrium position within the fluidic microsystem. In traditional, bench scale flow cytometers scattering is divided into two main types based on photon deviation from the initial direction of propagation; forward scatter (FSC) and side (orthogonal) scatter (SSC). Both types disclose different information about the sample of interest because the direction of the scattered light is linked directly to microparticle (cell) characteristics (cell size, structure, granularity and surface roughness), as presented in the following sub-sections.

2.7.1.1   Forward scatter

Forward scattered light is the measure of light that deviates within a small angle with respect to the incident beam axis, typically 0.5 – 5 degrees [58]. The intensity of this forward light scattering is dependent on the size of the microparticle (due to the amount of interface the sample has with the excitation beam) and on the refractive index difference between the microparticle and the surrounding fluid. The larger the cell, the more light is scattered in the small angle, resulting in higher collection intensity peaks. However, due to the in-line axis geometry of this detection with the excitation beam, FSC is a more complex parameter to differentiate from background noise. Forward scatter has been used in another work [59] to detect the viability of cells and thus discriminate between dead and live cells. This is based on the refractive index of dead cells more closely approximating to that of the surrounding fluid.

In most cytometers, a blocking (obscuration) bar is placed immediately in front of the incident laser beam to block any of the direct input light, to increase the signal-to-noise ratio (SNR) of the FSC signal. The greater the signal amplitude from a microparticle or cell compared to the noise amplitude on the detector, the more likely for an event to actually occur.

2.7.1.2 Side scatter

Side scattered light is the measure of the light that deviates significantly with respect to the incident beam direction. There are a wide range of angles (30° -90°), but it is typically collected at 90° to the sample flow and the beam axis, for significantly greater lowering of the noise that is simultaneously collected. Specific angles will have a unique optical signature; but it is quite difficult to collect light from these specific angles, mainly because the orientation of the sample is not fixed in the flow stream. This parameter is used to provide insight into the internal structure and granularity of the cell [59]. In general, the side scatter is much less intense than that of the forward scattered light, due to the many scattering centres, as a cell with internal structures can be presented as several dielectric objects made of different materials with various optical properties, and can have different sizes and shapes.

2.8   Summary

This chapter has introduced background theory regarding the principles of dielectrophoretic force, capillary flow in microchannels, laser diode and light scattering of microparticles. It has provided the relevant theory and equations necessary to understand and explain the experimental results shown in the following chapters. The chapter starts with the force on a dipole in an electric field and the DEP force of a uniform sphere in a non-uniform electric field. Clausius-Mossotti factor and its two numerical regimes, positive and negative, based on applied frequencies were introduced. The most important concepts in laser diode, such as absorption, spontaneous and stimulated emission, threshold gain and optical loss as well as density of states and population of states, were introduced. Finally, this chapter described the light scattering of microparticles.

2.9 Bibliography

[1]   H. A. Pohl, K. Pollock, and J. S. Crane, "Dielectrophoretic force: A comparison of theory and experiment," *J. Biol. Phys.*, vol. 6, no. 3–4, pp. 133–160, 1978, doi: 10.1007/BF02328936.

[2]   K. Khoshmanesh, S. Nahavandi, S. Baratchi, A. Mitchell, and K. Kalantar-zadeh, "Dielectrophoretic platforms for bio-microfluidic systems," *Biosens. Bioelectron.*, vol. 26, no. 5, pp. 1800–1814, 2011, doi: 10.1016/j.bios.2010.09.022.

[3]   H. A. Pohl, "Some effects of non-uniform fields on dielectrics," *J. Appl. Phys.*, vol. 29, no. 8, pp. 1182–1188, 1958, doi: 10.1063/1.1723398.

[4]   B. Cetin and D. Li, "Effect of Joule heating on electrokinetic transport," *Electrophoresis*, vol. 29, no. 5, pp. 994–1005, 2008, doi: 10.1002/elps.200700601.

[5]   J. Voldman, "Electrical Forces for Microscale Cell Manipulation," *Annu. Rev. Biomed. Eng.*, vol. 8, no. 1, pp. 425–454, 2006, doi: 10.1146/annurev.bioeng.8.061505.095739.

[6]   A. Aliano *et al.*, *AC Electrokinetics: colloids and nanoparticles*. 2003.

[7]   H. Bruus, "Theoretical Microfluidics (Oxford Master Series in Physics)," vol. 18, 2007, doi: 10.1017/CBO9781107415324.004.

[8]   Peter R. C. Gascoyne and J. Vykoukal, "Particle separation by dielectrophoresis," *Electrophoresis*, vol. 23, pp. 1973–1983, 2002.

[9]   THOMAS B. JONES, *Electromechanics of particles*. 1995.

[10]   L. Cui and H. Morgan, "Design and fabrication of travelling wave dielectrophoresis structures," *J. Micromechanics Microengineering*, vol. 10, no. 1, pp. 72–79, 2000, doi: 10.1088/0960-1317/10/1/310.

[11]   Y. Huang, X. B. Wang, J. A. Tame, and R. Pethig, "Electrokinetic behaviour of colloidal particles in travelling electric fields: studies using yeast cells," *J. Phys. D. Appl. Phys.*, vol. 26, no. 9, pp. 1528–1535, 1993, doi: 10.1088/0022-3727/26/9/030.

[12]   O. Parkash, D. Kumar, and C. D. Prasad, "A unified theory of dielectrophoresis and travelling wave dielectrophoresis," *J. Phys. D. Appl. Phys.*, vol. 27, no. 7, pp. 1509–1512, 1994, doi: 10.1088/0022-3727/27/7/025.

[13]   T. Z. Jubery, S. K. Srivastava, and P. Dutta, "Dielectrophoretic separation of bioparticles in microdevices: A review," *Electrophoresis*, vol. 35, no. 5, pp. 691–713, 2014, doi: 10.1002/elps.201300424.

[14]   D. Holmes, H. Morgan, and N. G. Green, "High throughput particle analysis: Combining dielectrophoretic particle focussing with confocal optical detection," *Biosens. Bioelectron.*, vol. 21, no. 8, pp. 1621–1630, 2006, doi: 10.1016/j.bios.2005.10.017.

[15]   Z. Wang *et al.*, "Dielectrophoresis microsystem with integrated flow cytometers for on-line monitoring of sorting efficiency," *Electrophoresis*, vol. 27, no. 24, pp. 5081–5092, 2006, doi: 10.1002/elps.200600422.

[16] C. Qian *et al.*, "Dielectrophoresis for bioparticle manipulation," *International Journal of Molecular Sciences*, vol. 15, no. 10. pp. 18281–18309, 2014, doi: 10.3390/ijms151018281.

[17] D. R. Gossett *et al.*, "Label-free cell separation and sorting in microfluidic systems," *Anal. Bioanal. Chem.*, vol. 397, no. 8, pp. 3249–3267, 2010, doi: 10.1007/s00216-010-3721-9.

[18] R. Pethig, "Dielectrophoresis: Status of the theory, technology, and applications," *Biomicrofluidics*, vol. 4, no. 2, pp. 1–35, 2010, doi: 10.1063/1.3456626.

[19] M. Li, W. H. Li, J. Zhang, G. Alici, and W. Wen, "A review of microfabrication techniques and dielectrophoretic microdevices for particle manipulation and separation," *J. Phys. D. Appl. Phys.*, vol. 47, no. 6, 2014, doi: 10.1088/0022-3727/47/6/063001.

[20] P. R. C. Gascoyne and S. Shim, "Isolation of circulating tumor cells by dielectrophoresis," *Cancers (Basel).*, vol. 6, no. 1, pp. 545–579, 2014, doi: 10.3390/cancers6010545.

[21] A. J. Smith *et al.*, "Rapid cell separation with minimal manipulation for autologous cell therapies," *Sci. Rep.*, vol. 7, no. February, pp. 1–15, 2017, doi: 10.1038/srep41872.

[22] G. Fuhr, H. Glasser, T. Müller, and T. Schnelle, "Cell manipulation and cultivation under a.c. electric field influence in highly conductive culture media," *BBA - Gen. Subj.*, vol. 1201, no. 3, pp. 353–360, 1994, doi: 10.1016/0304-4165(94)90062-0.

[23] F. E. H. Tay, L. Yu, and C. Iliescu, "Particle manipulation by miniaturised dielectrophoretic devices," *Def. Sci. J.*, vol. 59, no. 6, pp. 595–604, 2009, doi: 10.14429/dsj.59.1564.

[24] A. Mortadi, E. G. Chahid, and O. Cherkaoui, "Studies of the clausius – Mossotti factor," no. May 2017, 2016.

[25] R. Murugesan and J. H. Park, "Electrophoretic and dielectrophoretic trapping of molecular objects in planar quadrupole electrode configuration at room temperature," *J. Mech. Sci. Technol.*, vol. 31, no. 3, pp. 1331–1339, 2017, doi: 10.1007/s12206-017-0233-y.

[26] W. M. Arnold, H. P. Schwan, and U. Zimmermann, "Surface conductance and other properties of latex particles measured by electrorotation," *J. Phys. Chem.*, vol. 91, no. 19, pp. 5093–5098, 1987, doi: 10.1021/j100303a043.

[27] K. Khoshmanesh *et al.*, "Dielectrophoretic manipulation and separation of microparticles using curved microelectrodes," *Electrophoresis*, vol. 30, no. 21, pp. 3707–3717, 2009, doi: 10.1002/elps.200900079.

[28] K. Khoshmanesh *et al.*, "Size based separation of microparticles using a dielectrophoretic activated system," *J. Appl. Phys.*, vol. 108, no. 3, 2010, doi: 10.1063/1.3457226.

[29] M. Dürr, J. Kentsch, T. Müller, T. Schnelle, and M. Stelzle, "Microdevices for manipulation and accumulation of micro- and nanoparticles by dielectrophoresis," pp. 722–731, 2003.

[30]   T. Schnelle, T. Müller, S. Fiedler, and G. Fuhr, "The influence of higher moments on particle behaviour in dielectrophoretic field cages," *J. Electrostat.*, vol. 46, no. 1, pp. 13–28, 1999, doi: 10.1016/S0304-3886(98)00055-2.

[31]   J. Vanderlinde and D. E. Neuenschwander, *Classical Electromagnetic Theory*, vol. 62, no. 7. 1994.

[32]   U. Kim, J. Qian, S. A. Kenrick, P. S. Daugherty, and H. T. Soh, "Multitarget dielectrophoresis activated cell sorter," *Anal. Chem.*, vol. 80, no. 22, pp. 8656–8661, 2008, doi: 10.1021/ac8015938.

[33]   J. C. T. Eijkel and A. Van Den Berg, "Young 4ever - The use of capillarity for passive flow handling in lab on a chip devices," *Lab Chip*, vol. 6, no. 11, pp. 1405–1408, 2006, doi: 10.1039/b613839j.

[34]   C. C. Chen, P. H. Lin, and C. K. Chung, "Microfluidic chip for plasma separation from undiluted human whole blood samples using low voltage contactless dielectrophoresis and capillary force," *Lab Chip*, vol. 14, no. 12, pp. 1996–2001, 2014, doi: 10.1039/c4lc00196f.

[35]   P. F. Man, C. H. Mastrangelo, M. A. Burns, and D. T. Burke, "Microfabricated capillarity-driven stop valve and sample injector," pp. 45–50, 1998.

[36]   L. J. Yang, T. J. Yao, and Y. C. Tai, "The marching velocity of the capillary meniscus in a microchannel," *J. Micromechanics Microengineering*, vol. 14, no. 2, pp. 220–225, 2004, doi: 10.1088/0960-1317/14/2/008.

[37]   P. G. de Gennes, "Wetting: statics and dynamics," vol. 57, no. 3, 1985.

[38]   N. Ichikawa, K. Hosokawa, and R. Maeda, "Interface motion of capillary-driven flow in rectangular microchannel," *J. Colloid Interface Sci.*, vol. 280, no. 1, pp. 155–164, 2004, doi: 10.1016/j.jcis.2004.07.017.

[39]   W. Van Der Wijngaart, "Capillary pumps with constant flow rate," *Microfluid. Nanofluidics*, vol. 16, no. 5, pp. 829–837, 2014, doi: 10.1007/s10404-014-1365-3.

[40]   H. Cho, H. Kim, J. Kang, and T. Kim, "Capillary passive valve in microfluidic systems," *Tech. Proc. …*, vol. 1, no. 3, pp. 263–266, 2004.

[41]   I. Publishing *et al.*, "The Dynamics of Spontaneous Capillary Flow in Confined and Open Microchannels," vol. 183, no. 12, pp. 123–128, 2014.

[42]   J. Berthier, K. A. Brakke, D. Gosselin, F. Navarro, N. Belgacem, and D. Chaussy, "Spontaneous capillary flow in curved, open microchannels," *Microfluid. Nanofluidics*, vol. 20, no. 7, pp. 1–9, 2016, doi: 10.1007/s10404-016-1766-6.

[43]   Y. Zhu and K. Petkovic-Duran, "Capillary flow in microchannels," *Microfluid. Nanofluidics*, vol. 8, no. 2, pp. 275–282, 2010, doi: 10.1007/s10404-009-0516-4.

[44]   D. Yang, M. Krasowska, C. Priest, M. N. Popescu, and J. Ralston, "Dynamics of capillary-driven flow in open microchannels," *J. Phys. Chem. C*, vol. 115, no. 38, pp. 18761–18769, 2011, doi: 10.1021/jp2065826.

[45]   J. Berthier *et al.*, "Whole blood spontaneous capillary flow in narrow V-groove microchannels," *Sensors Actuators, B Chem.*, vol. 206, pp. 258–267, 2015, doi:

10.1016/j.snb.2014.09.040.

[46]   J. Berthier *et al.*, "Spontaneous capillary flows in piecewise varying cross section microchannels," *Sensors Actuators, B Chem.*, vol. 223, pp. 868–877, 2016, doi: 10.1016/j.snb.2015.10.023.

[47]   J. Berthier, D. Gosselin, and E. Berthier, "A generalization of the Lucas–Washburn–Rideal law to composite microchannels of arbitrary cross section," *Microfluid. Nanofluidics*, vol. 19, no. 3, pp. 497–507, 2015, doi: 10.1007/s10404-014-1519-3.

[48]   E. Delamarche, D. Juncker, and H. Schmid, "Microfluidics for processing surfaces and miniaturizing biological assays," *Adv. Mater.*, vol. 17, no. 24, pp. 2911–2933, 2005, doi: 10.1002/adma.200501129.

[49]   W. Huang, R. S. Bhullar, and Y. C. Fung, "The Surface-Tension-Driven Flow of Blood From a Droplet Into a Capillary Tube," *J. Biomech. Eng.*, vol. 123, no. 5, p. 446, 2001, doi: 10.1115/1.1389096.

[50]   S. Chakraborty, "Dynamics of capillary flow of blood into a microfluidic channel," *Lab Chip*, vol. 5, no. 4, pp. 421–430, 2005, doi: 10.1039/b414566f.

[51]   E. W. Washburn, "The dyanmics of capillary flow," *Phys. Rev.*, vol. 17, pp. 273–283, 1921.

[52]   H. S. Lew, Y. C. Fung, and S. Diego, "Entry Flow Into Blood Vessels," vol. 3, pp. 23–38, 1970.

[53]   H. S. LEW and Y. C. FUNG, "ON THE LOW-REYNOLDS-NUMBER ENTRY FLOW INTO A CIRCULAR CYLINDRICAL TUBE," vol. 2, no. 1968, 1969.

[54]   L.A. Coldren and S.W. Corzine, *Diode Lasers and Photonic Integrated Circuits*, 1st Editio. Wiley Series in Microwave and Optical Engineering, NewYork, 1995.

[55]   P. Blood, *Quantum Confined Laser Devices*, 1st Editio. Oxford University Press, Oxford, 2015.

[56]   M. G. A. BERNARD and G. DURAFFOURG, "Laser Conditions in Semiconductors," *Essentials of Lasers*, no. 1, pp. 178–185, 1969, doi: 10.1016/b978-0-08-013320-1.50021-x.

[57]   Eugene Hecht, *Optics*, 5th editio. Pearson Education, 2017.

[58]   H. M. Shapiro, "Practical Flow," *John Wiley Sons, Inc.*, p. 724, 2003.

[59]   J. R. Mourant *et al.*, "Light scattering from cells: the contribution of the nucleus and the effects of proliferative status," *J. Biomed. Opt.*, vol. 5, no. 2, p. 131, 2000, doi: 10.1117/1.429979.

Chapter 3

MATERIALS AND DEVICE FABRICATION

3.1   Introduction

One of the main objectives of this research is to develop and demonstrate the achievability of an approach: combining a dielectrophoretic microparticle manipulation technique with an integrated photonics platform for chip-based flow cytometry. The device consists of three elements; a fluidic network for an introduction and delivering of fluid and its microparticles or cells, a focusing section for confining these microparticles to the centre of the microchannel, and an optical system for illumination of microparticles and detection of scattered light (particularly the forward scatter (FSC)). While the most advanced monolithic integrated capillary driven microfluidic device with its lasers and photo-detectors has been achieved in previous work from Cardiff's optoelectronics group [1], variation in the microparticle's position and so velocity across the fluidic microchannel, results in significant variations in measured signal intensities from the similarly sized microparticles. Thus, for counting and sorting, the result requires complicated data analysis and shows a reduction in sorting accuracy and purity.

Focusing microparticles to the centreline of the capillary fill delivery network is in need to address these issues. In pump driven microfluidics several techniques exist to physically manipulate microparticles by using optical [2], magnetic [3], hydrodynamic [4] and electric [5] means. Among these, we found dielectrophoretic (DEP) microparticle manipulation to be the most convenient technique for our application. This is because it is compatible with microparticles and biological samples that are commonly used in diagnostics assays and it can be performed employing a relatively simple fabrication technique and experimental setup.

This chapter begins with a device concept and its required functionalities; followed by sections describing the design and fabrication work that has been undertaken during the research to develop a prototype chip that forms the basis of the experimental work presented in the following chapters. All the devices discussed in this work were fabricated using the microfabrication tools in a class 1000 cleanroom within the School of Physics and Astronomy at Cardiff University. The design is a consideration of the three main components believed to be necessary to provide a cell sorter system; especially that could have a significant impact on point-of-care diagnostics. The first component is the flow microchannel to deliver the target sample through microelectrode focusing section integrated on chip with lasers and detectors for scattering measurements. The second component is the microelectrode structure to control the microparticle's position within a flowing fluid stream using DEP technology. The third component is the laser sections, which are arranged perpendicular to the fluidic microchannel for forward light scatter measurements. The optical microscope image of a fabricated device, capillary fill fluid delivery system with n-DEP microparticle focusing system and integrated laser/detector sections, was presented in Chapter 1, Figure 1-3. The microfluidic devices were fabricated using standard lithography and etching methods. The main procedures used to build up our devices include: metal deposition, photolithography and chemical etching and along with the required equipment developed to control the prototype during the project, and the necessary sample handling will be presented in this chapter.

3.2   Device concept

DEP microparticle manipulation and control for integrated optoelectronic capillary driven microfluidics provides an opportunity to integrate functional components onto a single chip, with a minimal increase in fabrication timescale. This is important to reduce the dependence on external equipment while maintaining performance. The achievable highly integrated platform adds to the overall prototype performance and functionality. In particular, how well different parts will fit in the final device are critical to deliver a high quality device for and not limited to bioapplications including diagnostics [6]. The processing techniques for combining DEP capillary driven microfluidics with semiconductor photonic circuits are compatible with wafer scale manufacturing; which would promote a mass-producible device at potentially low cost, that would widely accessible to research laboratories and point-of-care clinics. Note that, while the most advanced DEP for semiconductor integrated optoelectronic microfluidics has been realized in this work, the control electronics are not currently integrated on-chip. We believe that the development in direct growth of compound semiconductor on silicon [7], would allow further advancement toward true complete system ready to replace benchtop cytometers in clinics while reducing costs.

The purpose here is to provide an experimental platform with which to study the strength of generated n-DEP focusing mechanism, and its potential with capillary driven applications to offer fast and efficient microparticle sorting as they pass through the coupling between paired in-plane laser cavities compared with those without DEP effect [1]. Thus, we will use a fluidic delivery network with inlet and outlet reservoir connected via the 3D embedded microchannel along with a microelectrode focusing section and all integrated on an optically active semiconductor material. A deep foundation for the fluidic network, along with the adhesion and physical insulation layers required to build up our sample, is etched through the compound Gallium arsenide (GaAs) substrate and between the paired lasers and photo-detectors. This is done to ensure that the optical axes of the lasers and photo-detectors will intersect the centreline of the microchannel. The microelectrodes are placed with respect to the microchannel's centre. Precise alignment is required for these three components, which can be achieved through standard lithography techniques.

3.3 Device Materials

Devices were fabricated using materials and fabrication techniques which are commonly used in the fabrication of compound semiconductor devices. This section presents the basic materials along with their desirable properties from which all experimental devices have been fabricated.

3.3.1 Fluidic network material

The embedded 3D microfluidic delivery system was created using Microchem SU-8 2050 negative tone photo-epoxy. SU-8 has some desirable properties that make it a favourable material for defining microchannels for microfluidic applications; it is electrically insulating, biocompatible, chemically and thermally stable and transparent over much of the visible and near ultra violet (UV) regime, which allows for thick layers and nearly vertical exposure profiles to be patterned over deeply etched surfaces [8][9][10]. Using SU-8 creates some challenges as the polymer in its native state is hydrophobic, which makes a capillary fill system difficult to achieve and it adheres poorly to many commonly used processing materials [11]. To overcome the adhesion problem, thinner formulation of the SU-8 (SU-8 3005 and 2002) were used to promote adhesion between the thicker SU-8 2050 and other materials and offer electrical isolation and physical separation from the GaAs surface and microelectrode structure.

3.3.2 Microelectrode material

The microelectrodes were made of chrome-gold (Cr-Au) metals. Au is one of the most commonly used metals to build up microelectrodes structure because of its low resistance and biocompatible nature [12]. However, the adhesion of the Au to SU-8 photo-epoxy, the material used to define both the base of the microelectrodes structure and capillary fill fluid delivery system, is particularly poor. Cr, on the other hand, adheres well to SU-8 and has been employed to overcome this inherent adhesion problem [13].

3.3.3 Quantum Well material

The fully integrated devices used throughout this project were fabricated from wafers obtained from IQE. The epitaxial layers are grown on an n-doped GaAs substrate in which the active region consists of three strained GaInP QWs, each being 6.5 nm thick and separated by a 7 nm $(Al_{0.5}Ga_{0.5})_{0.51}In_{0.49}P$ barriers and emitting visible red light at around 650 nm. The semiconductor wafer was commercially grown by IQE using metal-organic chemical vapour deposition (MOCVD). The exact layer structure of the wafer belongs to the manufacturer and therefore cannot be included.

3.3.4 Glass substrate

Microscope slides cover glass of size (18 mm $\times$ 18 mm $\times$ 0.5 mm) were used as substrates for testing the microfluidic and DEP parts of the structure before full integration. This minimised the fabrication workload and the unnecessary use of compound semiconductor material.

3.4 Device design

The device design is composed of three key components that are in need to develop a true chip scale flow cytometer; i) a microfluidic system that promotes laminar flow through both the focusing and interrogation zone, ii) a microelectrode configuration for the purpose of achieving the most effective DEP focusing in a pump free system, and iii) a monolithically integrated laser/photo-detector array for forward light scatter measurements. All the photomasks included in this PhD research have been created with e_LiNE (Raith) software. The designs were saved as GDSII format before they were sent to be printed on anti-reflective chrome on soda Lime substrate of 4″ $\times$ 4″ inches. In the following subsections, all the designs are presented in detail.

3.4.1 Microfluidic system design

The microfluidic capillary driven system design can be seen in Figure 3-1. In its simplest form the capillary driven fluid flow system is made of three main parts; i) an inlet reservoir, ii) a 3D microchannel, and iii) an outlet reservoir. The inlet reservoir is

a rounded hole with a diameter of approximately 1500 µm into which the sample fluids are deposited. The 3D microchannel that promotes laminar flow has a width of 50 µm and a length of 1410 µm (or the channel is 60 µm wide and 2660 µm long in the final fully integrated device with laser/photo-detector sections). The width of the microchannel was chosen not only taking into account the size of the target microparticles that the devices aim to handle in the future (as large as 20 µm in diameter as this is a similar diameter of the largest type WBCs) but also to reduce the likelihood of blockages of the 3D microchannel. The length is proposed and designed so that it can accommodate the microelectrodes and other functional components (laser/photo-detector pairs that can be patterned to collect scattered light at a wide range of angles to the excitation line). The microelectrodes have to be sufficiently long to move the particles to the centre of the channel in the time they are passing them and the channel has to also be long enough to also accommodate two laser/photo-detector pairs to allow for forward scattering measurements. This is the minimum number of required forward scatter measurements that would allow for error checking results and also allows for computing the microparticle velocity at the point of interrogation. In addition, increasing the length of the 3D microchannel to 2660 µm provides the capacity for increasing the number of lasers for large-angle side scatter measurements on a single microchip. A microchannel longer than this would be a waste of III-V active substrate, increasing the total cost and size per device. The outlet reservoir consisting of an open-end roofless spiral microchannel that provides a continuing pull on the advancing fluid and also allows for easier microchannel cleaning.

Figure 3-1 shows that, in terms of the shape, the inlet reservoir has been designed with the same diameter as the outlet; also, the spirals are constructed from half-circular arcs simply to reduce the waste of real-estate of the III-V semiconductor substrate, to avoid any sudden change in flow direction also for the aesthetic end. In addition, the small triangle at the entrance of the 3D microchannel has been proposed and designed to prevent large clumps of microparticles blocking the main 3D entry and producing a problem with microchannel cleaning.
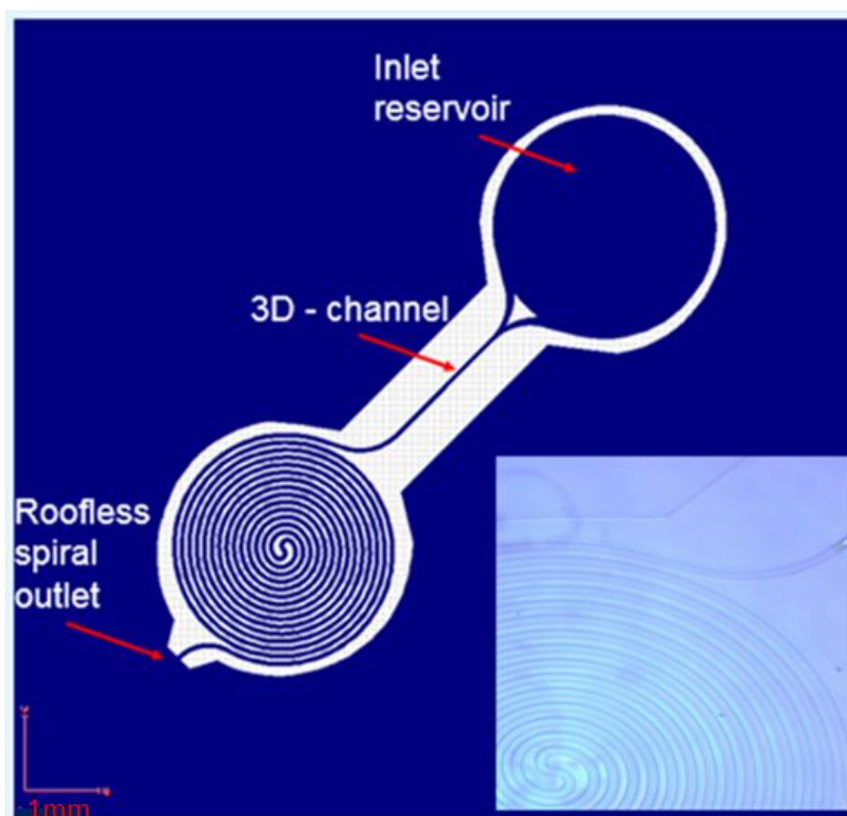
Figure 3-1 A Schematic shows the design of the microfluidic system and a closeup microscope image of the fabricated in-out roofless spiral (bottom right).

The height of the 3D microchannel can be targeted depending on analyte size, however, in this work, a standard height of 27- 30 µm was used to allow a range of tests samples to be used. The work in chapter 4 and 5 focuses on 6 and 10 µm in diameter polystyrene microparticles, while in chapter 6 the 15 µm in diameter polystyrene microparticles are also used for better sensitivity (increased difference in detected signal intensity from background) and to mimic a range of cell sizes.

3.4.2   Triangular-shaped microelectrodes

Figure 3-2 shows a top, side and cross-sectional view of the designed microelectrodes to be powered with an AC signal. This design would create a non-uniform electric field required to generate n-DEP force. To drive flowing microparticles within the fluid flow, regardless of their size, into the same reference position within microchannel cross section, two pairs of a triangular-shaped microelectrodes face-to-face below and above surfaces of the microchannel are required.

In such a design, the opposite microelectrodes had an original gap of 48 µm which shrinks to 8 µm at the end of the microelectrode structure. This smallest gap between opposite microelectrodes at the centreline of the microchannel is to guide the microparticles to move in a single stream in the microchannel centre, taking into account the size of microparticles that the device aims to address in the future (6 µm in diameter is the size of the smallest type WBCs). The vertical spacing between the two pairs of the microelectrodes, on the top and under the bottom surface of the microchannel, is the targeted height of the fabricated microchannel, which is typically 27 - 30 µm. Owing to their triangular shape, the microelectrodes create a strong spatially non-uniform electric field at the edge, which is crucial to create a DEP force. The microelectrodes design was made to be 380 or 300 µm in length, a design we believe can provide enough exposure time for the microparticles in flow to be moved under the influence of DEP force. For comparison, a design with a reduction in the length of the microelectrodes is proposed as this would reduce the final chip size and so is advantageous.
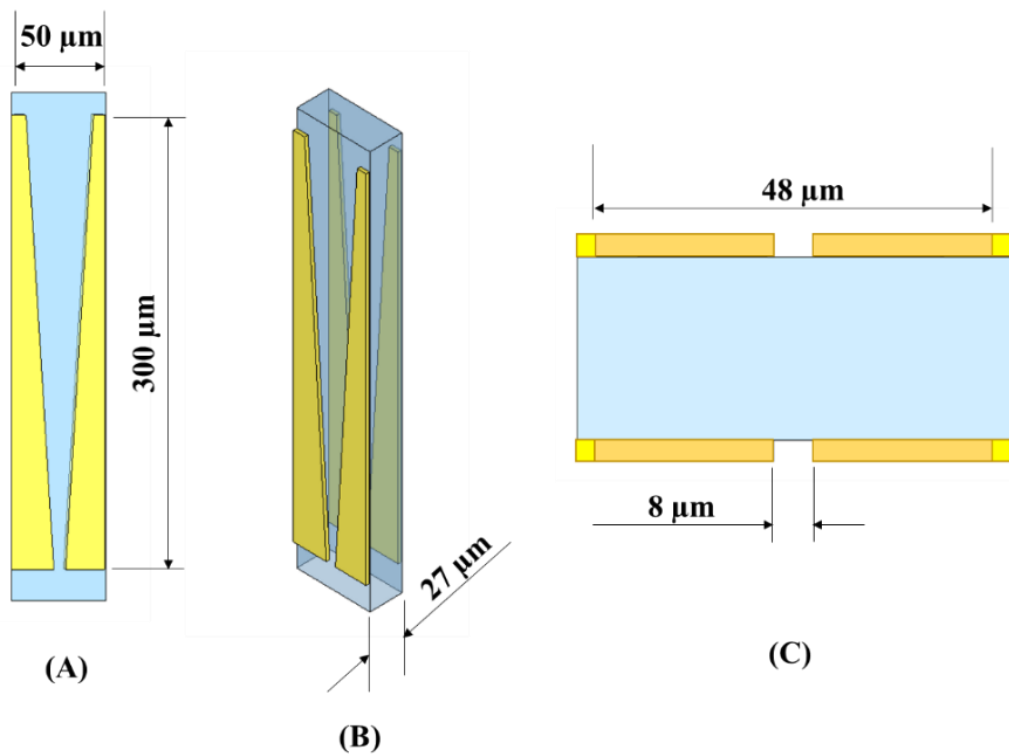
Figure 3-2 A large view shows the structure of microelectrodes along with the straight 3D microchannel and dimension of DEP platform. (A) top-view, (B) side-view and (C) cross-sectional view.

While independently conceived I note that the developed DEP platform is very similar to one found in the literature, there targeted at a pump driven system [14] as opposed to the passive microfluidic system used here. The microfluidic device of Holmes et al. (2006) is shown in Figure 3-3 (A), the device itself is a sandwich of two glass substrates. In their experiment, latex particles with a 6 µm diameter suspended in DI water, are used for applied voltages of 0 V_{p-p}, 5 V_{p-p}, 10 V_{p-p}, 15 V_{p-p} and 20 V_{p-p}. Holmes et al. (2006) have provided the trajectories of latex microparticles near the end section of the microelectrode. It is clear to see in Figure 3-3 (B) that the microparticles are focused at the centre of the microchannel for an applied voltage of 20 $V_{p-p,}$ this was in the microelectrode region and also at the end of the microelectrode section. In their experiment the maximum flow rate after focusing is mentioned to be ~1 mm/s for an applied voltage of 20 $V_{p-p.}$ In this work, because of the capillary drive approach, the fluid rate and hence microparticle velocity is not controlled externally but measured, however, a sufficient focusing of polystyrene microparticles is achieved and the results are presented in the following chapters.
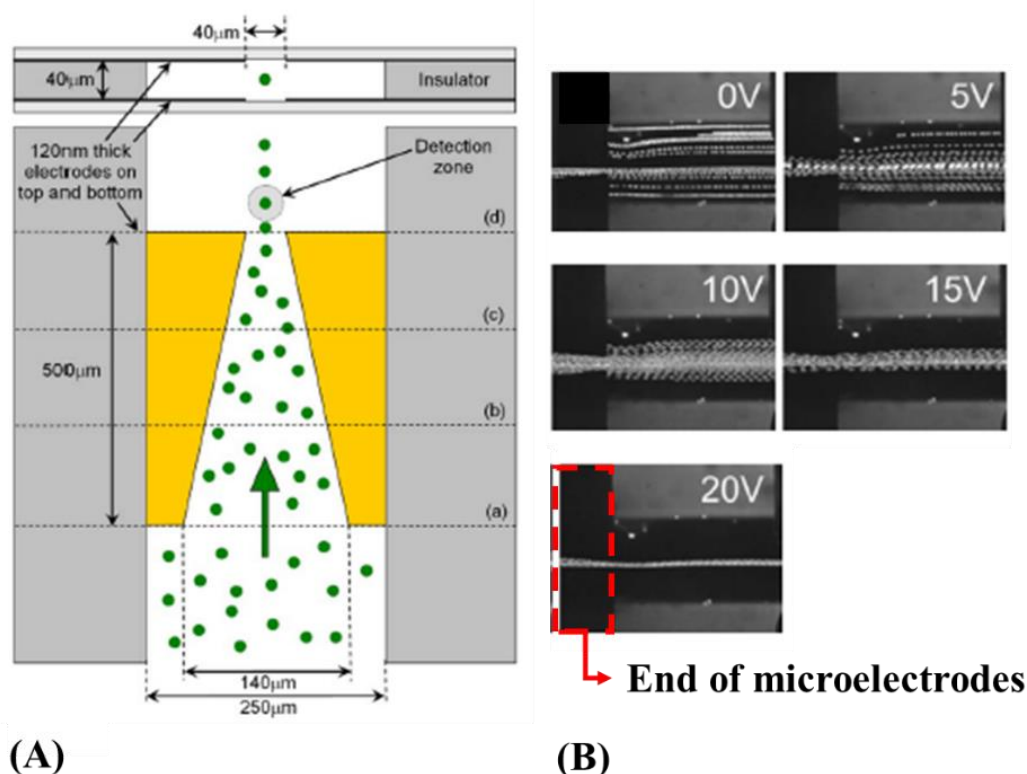
Figure 3-3 (A) Schematic of the flow cytometer chip of Holmes et al. (2006), and (B) lateral movement of the microparticles as a function of applied voltage can be followed through the image sequence. It is clear that increasing the applied voltage causes the latex microparticles to focus into a tight width at 20 V_{p-p} [14].

Compared with [14] microelectrodes fabricated onto a single substrate, this approach would reduce much of the time consuming, expensive work and the probability of a failure in alignment. Furthermore, the smallest gap distance in this work is smaller than the minimum gap distance has been included in Holmes et al. (2006), and it is also smaller than the minimum gap that has been used with curved microelectrodes in Khoshmanesh et al. (2009) [15] and Morgan et al. (2003) [16]. However, no damage to the microelectrodes' structure was observed when an AC potential of 40 V was applied; the results we have seen are shown in the next chapter.

3.4.3   Light source/detector design

An array of 30 µm wide oxide stripe laser pairs patterned on 150 µm wide etched mesas are set 100 µm apart either side of the 3D microfluidic capillary driven channel. The channel is in the range of 27 - 30 µm deep and is etched into the surface of an active GaAs crystal and deposited SU-8 so that the optical axis of the lasers/photo-detectors will intersect with the middle point of the microchannel. The lasers/photo-detectors themselves are arranged perpendicular to the microchannel and face each other from opposite sides. This allows for FSC measurements to be made on an analyte of choice. In this work, in order to reduce the width of the diverging laser beam to create more efficient illumination of the microparticles and allow convenient detection of the emitted light, a maximum gap of 100 µm is chosen [17][18]. The two laser and photo-detector pairs are spaced 300 µm apart along the length of the microchannel and fixed at 300 µm away from the end of the microelectrodes, which is the minimum required space for the laser contact pads.

Each laser on chip can operate as a laser light source while the others can act as photo-voltage detectors. By operating the lasers in sequence, a microparticle passing through the laser beam causes a perturbation to the light signals. Beam transit events are captured from both sides of the microchannel in separate but sequential events allowing for on chip light-current curves measurement for characterisation of each laser section. This system also will allow for on chip microparticle velocity to be measured at the point of interrogation. Under an efficient focusing of the microparticles, which should lead to reduced variations in the intensity of the detected signals, faster sorting of the different sized polystyrene microparticles is expected

compared to those without DEP effect reported in [1] while using a much wider laser beam.

3.5   Fabrication

This section contains the detailed process flow that is used and developed to build up the microfluidic devices to be used in the experimental test throughout this research.

3.5.1   SU-8 microfluidics fabrication

3.5.1.1   Deep etched microchannel

To achieve a platform that combines array of lasers and detectors for photovoltage transduction with an on chip capillary fill fluid delivery system and integrated microelectrodes, a deep foundation microchannel must be etched into the GaAs substrate between the laser/detector sections. This is done using a photo mask consisting of the adhesion promoter HMDS and the positive photoresist S1813. All the laser/detector sections are covered by the photoresist leaving the rest of the semiconductor substrate of the chip exposed to the light from the ultra violet (UV) Karl Suss MJB3 Mask Aligner, including a 60 µm width channel between the etched facets of the lasers/detectors. This will provide electrical isolation and reduces the electrical pickup in nearby detector sections [18].

The samples in this study have been etched to a depth of approximately 22 µm. An isotropic chemical wet etch technique is appropriate to achieve this desired depth. Wet etch is faster and more economical than dry etch. In this work, the etch has been controlled with the depth measured every 10 minutes using a Veeco Dektak 3 surface profiler to make sure that the optical axis of the lasers will intersect with the midpoint of the microchannel's height. Sidewall verticality of this feature is not crucial at this stage as it just serves as a foundation for the following layers. Microfluidic channel walls are defined inside this foundation at some later point. The cross section view in Figure 3-4 indicates the position of the laser/photo-detector relative to the centre point of the microfluidic channel. The thickness of the lid and the height of the microchannel can be changed simply by modifying the spin speed of the SU-8 and exposure time respectively.

1 GaAs substrate	**2** SU-8 3005/ adhesion promoter and electrical isolation layer	**5** SU-8 2050
3 Cr/Au	**4** SU-8 2002	**6** Active region
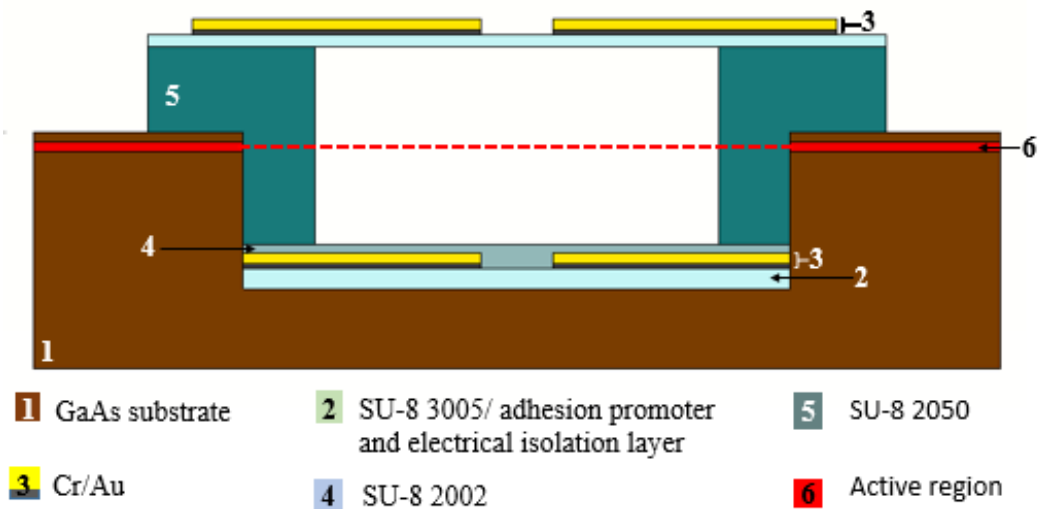
Figure 3-4 Cross section of the device showing the 3D microfluidic channel, Cr/Au microelectrodes, the adhesion promoter and electrical isolation layers of SU-8 3005 and 2002. The optical axis of the lasers intersects the microchannel at the middle of its hight. The drawing is a cutting plane taken through the microsystem (presented in chapter 1). The microsystem is imagined as being cut through at the microelectrodes region and where the laser sections are in the final device.

3.5.1.2   SU-8 microfluidic channel

The integrated microfluidic delivery system fabricated in this work has been achieved using multiple layers of the photosensitive epoxy SU-8, for the reason mentioned in section 3.3.1. The SU-8 layers are applied to the substrate by spin coating and patterned with the light from the Karl Suss MJB3 UV 400 mask aligner using the photolithography technique. Photolithography, also termed optical lithography or UV lithography, is a technique which uses UV light for transferring a geometric pattern from a photomask to a photosensitive material (resist) covering the surface of a substrate. The exposed areas of a positive photoresist or unexposed areas of negative photoresist can be easily washed away when immersed in a developer solution forming a desired pattern in the remaining photoresist. The standard photolithography steps applied in this research are shown in Figure 3-5.
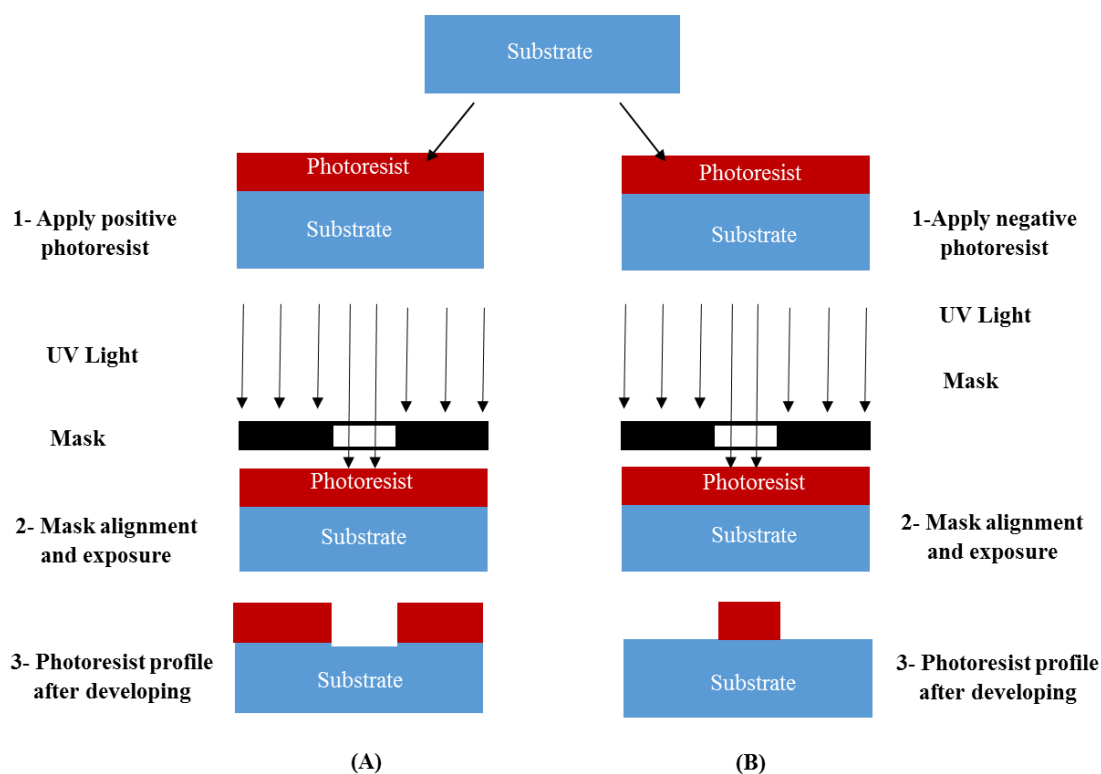
Figure 3-5 Schematic of the photolithography steps followed in processing both types of photoresists.

To create a foundation layer on a glass substrate, or on a previously etched semiconductor surface, a 5 µm thick layer of SU-8 3005 is spun coated on the sample at 6000 rpm for 45 seconds. The coated substrate is then pre-exposure baked by being placed on a hot plate at a temperature of 97°C for 2 minutes. This is an important step, removes as much solvent as possible so that the amount of swelling in the SU-8 membranes is reduced. After that, the sample is patterned, as in step 2 of figure 3-5 using UV exposure for 35 seconds. The structure is completed after cross-linking the polymer by a post exposure bake and developing in Microposit ethylene carbonate (EC) solvent. The sample is hard-baked at 180°C on a hot plate for 20 minutes. This step is essential as it was found to improve the chemical resistance of the SU-8 photo-epoxy by ensuring that it is fully cross-linked and is no longer soluble [8]. This layer not only acts as an electrical isolation but also as an adhesion promoter for the subsequent layers. After exposing and hard baking the sample ready for the bottom microelectrodes to be fabricated. The bottom microelectrodes were fabricated by photolithographic patterning of photoresist, evaporation of metal (Cr/Au) followed by lift-off in acetone, the whole process is presented in the next section.

The next step is to spin coat either a 2 µm thin layer of SU-8 2002 or a 5 µm thick layer of SU-8 3005 onto the sample. The thinner layer of SU-8 can be used in order to reduce the etching depth through the GaAs substrate. The mask for this layer defines the base of the microchannel sealing it from the bottom microelectrodes. In this case the SU-8 3005 shows a good uniformity to be used as microchannel base as well as bottom microelectrodes insulation layer. Spin coater is widely used process for fabrication of MEMS devices. However, the film thickness is affected by spin speed, acceleration and viscosity (fresh SU-8) so it could reduce the tolerance in fabrication that can be acceptable. In this work, there is some variation in the SU-8 thickness but when we set the spin speed we should be able to achieve a repeatable SU-8 thickness subject to have fresh SU-8 and developer.

After exposing, developing and hard baking the isolation layer, the next step is to define the sidewalls and roof of the microchannel. For a successful metallic top microelectrode pattern on the microchannel's roof, a 3005 thick formulation of SU-8 is used onto a 2050 formulation, this layer serves as an adhesion promoter to the next layer of Cr/Au due to the reason mentioned earlier in this chapter. A method, as stated in [1], using a dual wavelength exposure [19], creates a 3D structure microchannel using a single layer of polymer and a double UV exposure. The advantage of this method is that the 3D microfluidic structure is achieved using the conventional photolithography mask aligner. The same method is used here but with two layers of polymer coated on top of each other. The sample is spun coated with a 27 - 30 µm layer of SU-8 2050, after soft baking (incomplete drying of the film) at a temperature of 67°C for 2 minutes followed by 97°C for 6 minutes, a 3 - 5 µm thick layer of SU-8 3005 is spun coated onto the sample. After soft baking this layer, the next step is to define the sidewalls and roof of the microchannel using optical filters to select different emission lines of a single UV light source. A Hoya 370 nm long pass filter used with a photomask, patterns the inlet reservoir, open-end roofless spiral and the sidewalls of the microchannel. At this wavelength the SU-8 is partially absorbing so that the light can penetrate all the way down to the bottom of the SU-8 layer creating thick nearly vertical profile. After this exposure, immediately a second exposure using an Asahi-spectra 340 nm band pass to single out the 334 nm emission line of the UV lamp with the photomask, patterns the roof of the microchannel. At this wavelength SU-8 is highly absorbing and so the light can only cross a very short distance into the polymer.

The processing sequence is shown in Figure 3-6 (A) and (B). Then the final structure in Figure 3-6 (C) is completed after cross-linking of the SU-8 by a post exposure development in EC solvent and hard baking.
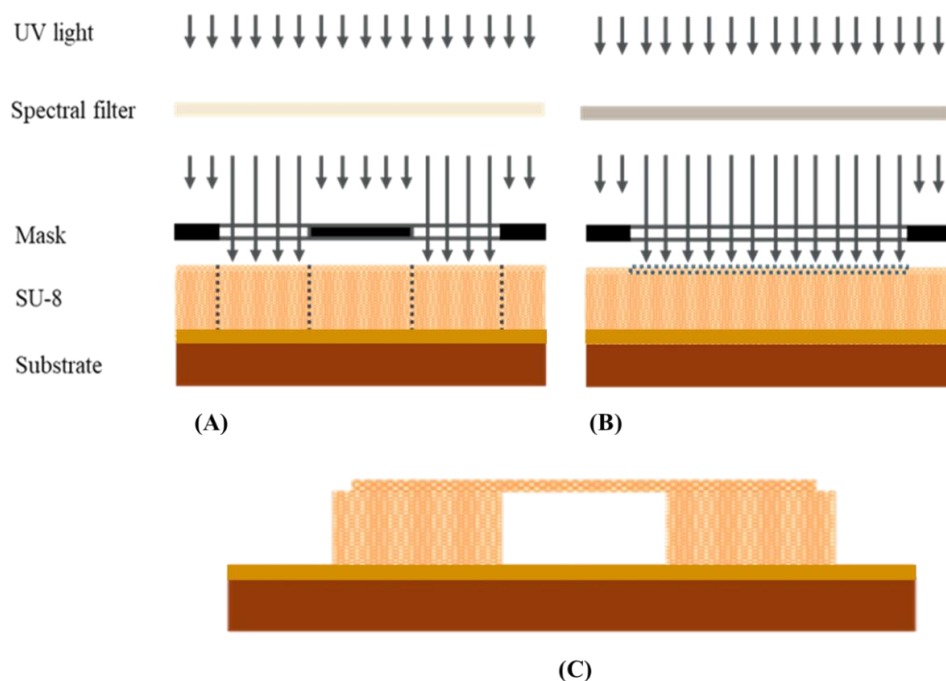
Figure 3-6 Schema of the processing steps in the fabrication of the SU-8 microfluidic channel. (A) Exposure of the SU-8 using light from the UV mercury lamp, a long pass filter and a glass mask patterned with opaque metal to define the sidewalls of the microfluidic network. (B) Exposure of the SU-8 using a shorter wavelength of the UV lamp via bandpass filter and a photomask to pattern the roof of the microchannel. (C) The microchannel structure after the post exposure bake and development. All the regions that were not exposed to the UV light during each of the exposure steps (A) and (B) and through the selected optical filter will wash away (blocked by dark regions of the photomasks) Note that features are not drawn to scale.

The developer removes the unexposed SU-8 starting from the roofless open ends and leaves the inlet and outlet reservoirs connected via the embedded 3D microchannel. The complexity of the pattern and the difference in density of material across the wafer, due to the mixture of open and 3D embedded microchannels, results in a quite different developing time. The development time for different parts of the microfluidic network is checked under the microscope. A range of development times was observed (15 – 60 minutes). After 60 minutes, the inlet, 3D microchannel and roofless open-end spiral are completely developed. The development inside the 3D microchannel is microscopically checked by focusing on both the microchannel base and then the roof, then by using a pipette to drop a small amount of isopropanol (IP) in the inlet and

check it can pass through the 3D microchannel all the way out to the spiral open-end. The sample is then ready for the next step, which is the definition of the top microelectrodes, as it shall be presented in detail in the next section.

3.5.2 Triangular-shaped microelectrode patterning

The triangular-shaped metallic microelectrodes were fabricated using standard photolithography, thermal evaporation of metals (Cr/Au) and lift-off methods. For successful metal lift-off, two resists, PMGI SF11 and S1813, were used to form a bi-layer resist process to provide a suitable resist profile [20]. First, a 0.5 µm SF11 thin film photoresist is spun coated onto the wafer at 5000 rpm for 20 seconds and then soft baked on a hot plate at 103°C for 10 minutes. Immediately followed by a 1.5 µm S1813 thin film spun coated onto the SF11 at 5000 rpm for 20 seconds and then soft baked at 80°C for 5 minutes. Because of the chemical properties of the PMGI SF11, no intermixing occurs with the subsequent photoresist layer. After that, the pattern transfer was achieved using a photo-mask and a UV 400 Karl Suss MJB3 Mask Aligner with an exposure time of 5 seconds. After imaging, the exposed photoresist and PMGI SF11 are developed away in MF319 for 15 – 20 seconds and then rinsed with deionised (DI) water for at least 1 minutes, leaving the desired pattern for metals deposition step as shown in Figure 3-7. This is because once the S1813 photoresist is fully developed and the dissolution of the photoresist stops, the developer continues to remove the PMGI SF11 layer in the open area. This is because PMGI is not photosensitive but freely soluble in developer. Thus by slightly increasing the developer time the SF11 layer undercuts the S1813 layer above. This prevents the subsequently deposited metal from completely sealing allowing access of the developer and the lift-off process to work.
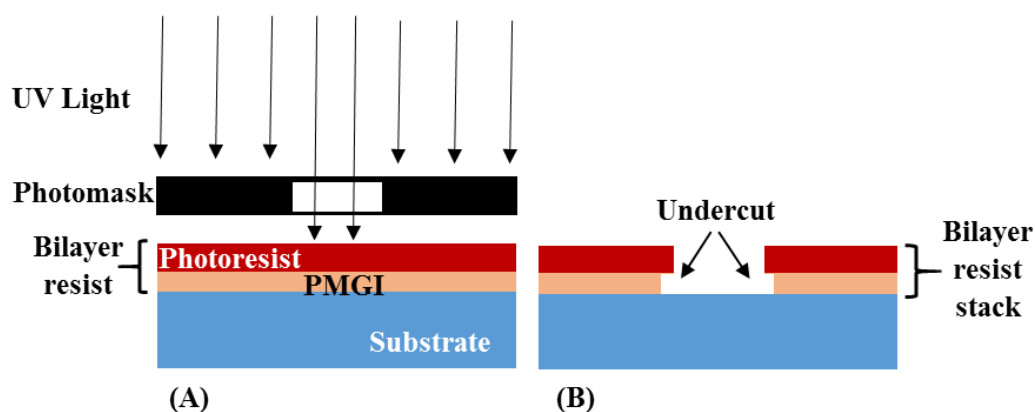
Figure 3-7 The desired bilayer resist profile after exposure and development. The undercut can be defined as the distance between the edge of the photoresist pattern and the edge of the PMGI structure where it contacts the surface of the sample.

For the microelectrodes, to be electrically powered, which is required to generate a n-DEP force, a localised non-uniform electric field, that drives the microparticles in the flowing fluid toward the centreline of the microchannel, a thin film of Cr/Au metals was deposited on the sample by the common thermal evaporation technique. In this technique, the source metal to be evaporated is placed in a resistive heat source under a high vacuum environment (at least 1×10^{-6} mbar). The metal temperature is raised gradually by Ohmic heating, passing a high current through the source, until the source metal vaporises in all directions and condenses on the cold substrate as well as the deposition chamber (glass bell jar). A quartz crystal was used to monitor the film thickness. In this work, two layers of metals, Cr/Au (10 nm/250 nm), were deposited onto the patterned photoresist using an Edwards E306 thermal evaporation vacuum system. For contamination free and good adhesion between Cr/Au films, gold is deposited onto the chromium layer during the same evaporation session under a high vacuum. The microelectrodes are only 260 nm thick, compare to the microchannel height of at least 27 µm, and have no effect on the fluid motion through the microchannel. Once the metal films were deposited onto the patterned photoresist, the wafer was immersed in acetone to dissolve the unexposed photoresist layers. When the unexposed photoresist is washed away it takes with it any metal not directly adhering to the sample, and this technique is known as lift-off. This lifting-off results in a pattern of bottom microelectrodes and the extended parts required for electric contact on the coated substrate. The same process flow has been used to fabricate the top microelectrodes pair with the required extended parts for the electrical contacts.

Upper microelectrodes are built through in house-made shadow mask (see Appendix). The shadow mask is created as it covers the sample and only leaves the top microelectrodes and the extended parts for electric contacts open for metal deposition. The mask is used to create an extra protective layer to protect the coated areas with unexposed bilayer resist from any Cr/Au film to be deposited outside the desired area during the metallization process. The sample is fixed between the shadow mask and carrier after alignment. The carrier is placed upside down in the evaporation chamber and the thin film metal deposition process carried out. Using this metallization method, we have successfully fabricated microchips used in experimental work. This method not only prevents the continuous metal deposition film from forming where it will be hard to remove but also reduces the lift-off processing time which reduces the solvent induced swelling of the SU-8 that previously patterned. However, it is a time consuming and costly single chip process for our research approach.

Therefore, for the ease of manufacture and scalability, SPR 220-7.0 positive photoresist is proposed and used in conjunction with an adhesion promoter HexaMethylDiSilazane (HMDS) to fabricate the top microelectrodes instead of S1813 positive photoresist and without the need of the shadow mask. This is because this photoresist is ideal for thick film applications up to 15 μm with a single coat [21]; however, the alignment is slightly harder. HMDS is commonly used to improve the adhesion at the interfaces [22]. The HMDS is spun coated and then baked on a hot plate at 103°C for 2 minutes. Immediately followed by a thin film of PMGI SF11 resist spun coated onto this layer and then baked as presented earlier in this section. Then, about 8 μm thick layer of SPR 220-7.0 is spun coated onto the PMGI SF11 at 6000 rpm for 40 seconds, then soft baked at 110°C for 3 minutes. The pattern transfer was achieved using a photo-mask and a UV400 Karl Suss MJB3 Mask Aligner with an exposure time of 14 seconds. As a final step, the exposed photoresist is developed away in MF 26 A for 60 seconds, and rinsed with deionised (DI) water for at least 1 minute then hard-baked at 110°C for 3 minutes, leaving the desired pattern for the metal deposition step. Figure 3-8 shows close up photographs of the patterned microelectrodes. The left-hand side image with the white and yellow dashed lines highlighted the outlines of the bottom microelectrodes and some parts of extended metal pattern required for electrical connections and the inner walls of the microchannel, respectively. While the right-hand side image with the white dashed

lines highlighted the outlines of the top microelectrodes together with the extended parts required for electric connections and the white circle highlighted the main entrance of the straight 3D channel.
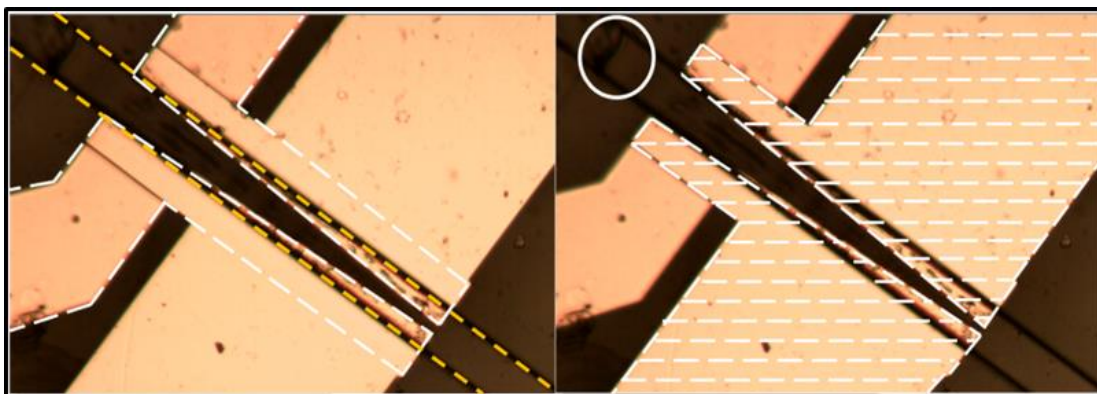
Figure 3-8 Photograph of the patterned microelectrodes with integrated 3D microchannel fabricated on a glass substrate. The yellow dashes lines highlighted the inner walls of the channel, white dashes lines highlighted the bottom, and top microelectrodes geometry and the white circle highlighted the main entrance of the straight 3D channel.

3.5.3   Final microchip

The final fabricated device in Figure 3-9 presents a novel photonic integration platform with capillary fill microfluidics for chip-based flow cytometer. It comprises a monolithic coupled array of lasers and detectors for photo-voltage transduction with an on-chip capillary driven fluid system and integrated microelectrodes. Conductive (Cr/Au) triangular shaped microelectrodes above and below the 3D microchannel, create a non-uniform electric field. These microelectrodes cover a large part of the 3D capillary driven microchannel to gradually deflect the movement of the microparticles within a flowing flow, such as cells, to reach their equilibrium position in the centre of the microchannel via n-DEP. On the glass substrate, the 3D microfluidic network is 50 µm wide and 1410 long. In the final device, fully integrated platform with lasers and photo-detectors, the microchannel is 60 µm wide and 2660 µm long, patterned onto 20 – 30 µm deep etched microfluidic foundation into the GaAs wafer. The lasers themselves are fabricated as in [18] by Gillgrass. The microparticles passed in a focused single stream through the lasers and are counted and sorted according to a photo-voltage output change compared to the normal signal, as it shall be presented in chapter 6.
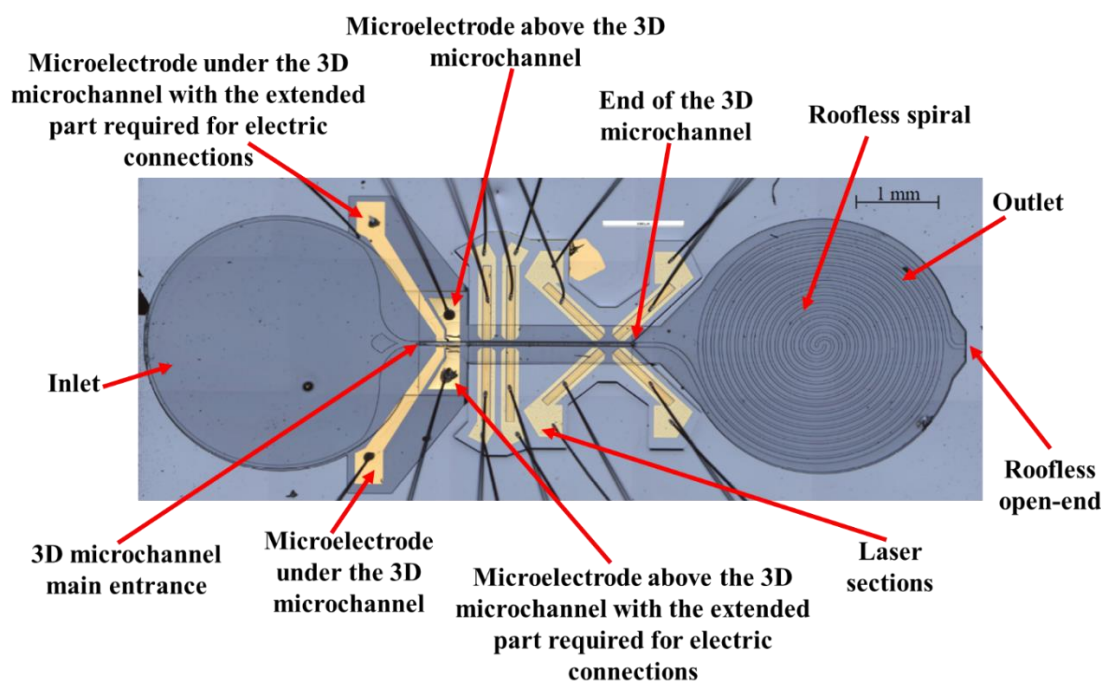
Figure 3-9 Integrated photonics with DEP microparticle focusing system for chip based flow cytometry. The optical microscopic image shows the III-V semiconductor platform that combines array of lasers/detectors for scattering measurements with on-chip capillary driven system and microelectrodes. The black lines are electric connections made to each of lower and top microelectrodes and p- and n-side contacts for the lasers/detectors.

To investigate the integration concept we use a relatively simple p-i-n diode structure, which can be used as a laser or a photo-detector. It is made up of a single GaInP / AlGaInP quantum well (QW) grown within an optical waveguide core and clad with p and n doped AlInP to craft optical wave guiding in the vertical direction. Under electrical forward bias of one section, the resulting light intensity across the gap and coupled into the active region of the opposite section are recorded through a data logger. This device should be simple to use, perform an efficient size based capture, sorting and counting of cells for diagnosis and monitoring diseases without the need for precise alignment of external optical components with the fluidic microchannel and free from any pump or syringe systems.

3.6   Packaging

3.6.1   DEP capillary driven microfluidics

The 18×18 mm^2 fabricated sample onto a glass substrate is placed directly between a flat copper block and a printed circuit board (PCB) and then fixed via two small screws, which compress the PCB with the copper block, as shown in Figure 3-10 (A). The electrical connections are then made using a K&S model 4523 wire bonder to bond 30 μm diameter Al wires from the contact pads of the microelectrodes on chip to a printed circuit board that houses 24-pins electrical connectors. Note that silver loaded epoxy will be applied on the wires to prevent detaching during the experiments. In addition, the 24-pin package allows the bonding of a fully integrated device with lasers and photo-detectors. Then, the chip is plugged directly into an in-house-made holder unit that includes the required electrical connections to the microelectrodes to be powered by an AC signal and an electronic workshop-made-amplifier. The holder unit can be fixed onto the microscope flat stage via a small screw, as shown in Figure 3-10 (B).

(A)   (B)
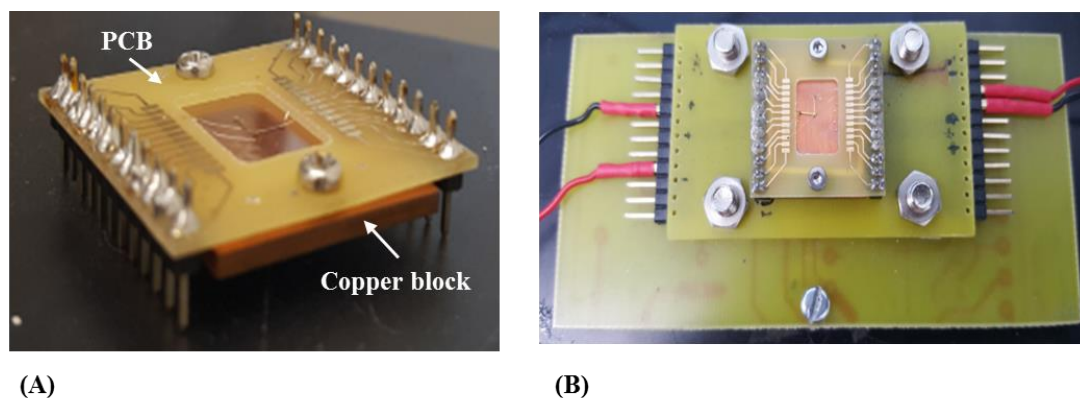
Figure 3-10 Photographs of a full packaged device, the DEP capillary driven microfluidic that built on a glass substrate, and contact arrangement. The fabricated chip fixed between PCB and copper block. The PCB with gold plated pads is used for microelectrodes contacts wirebonds and the 24 way connector pins allows easy electric connection to drive boards in use with final fully integrated device with lasers and photo-detectors. (B) A plugged sample into an in-house-made holder unit and contact arrangement to be powered by an AC signal.

3.6.2   Photonics integrated with DEP capillary fill delivery system

The packaged device pictured in Figure 3-11 shows the most advanced version of the photonic integrated platform with DEP capillary driven system that we have produced to date. The 12×12 mm^2 sample is cleaved to remove any unused III-V semiconductor substrate before the mounting step. This is important to prevent overhang on the copper header that the device will mount directly to and also the electrical connections to the printed circuit board (PCB) are easier. The sample is mounted into a flat copper block using silver loaded epoxy. The copper block is attached to the PCB via small tow screws, which houses the 24 way connector pins. These pins will provide an electric connection from the gold plated pads to the individual p- and n-contacts and the four microelectrode wire bonds. A K&S model 4523 wire bonder was used to bond 25 µm aluminium wires from the gold plated pads onto a printed circuit board (PCB) to the conductive point's on-chip. The sample was plugged directly into a control unit that houses the electronics required to drive the lasers and photo-detectors, and electric connectors to power the microelectrodes focusing section by an AC signal and through the house-made voltage amplifier. The control unit is designed with a low profile so that it can be operated within a working distance of a microscope objective lens, which allows the passage of microparticles to be recorded independently of the chip based scattering measurements using a high speed camera. The camera and microscope are used to characterise the performance of the device and are not a necessity of the final system. The amplified detector outputs are logged externally with a NI 6210 USB data acquisition board (DAQ) and the data from both the DAQ and high speed camera are recorded to a computer. For a completely self-contained system we imagen that the functionality of the DAQ and controller-based electronic circuits would also be integrated on-chip and the system could be controlled and/or monitored by a smartphone.
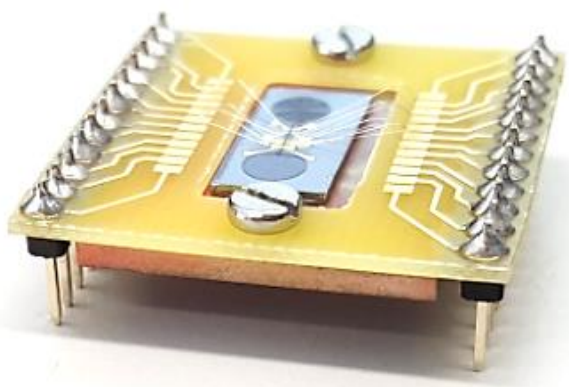
Figure 3-11 A packaged device showing the completed integrated III-V semiconductor that combines an array of lasers and detectors for photo-voltage transduction with an on-chip capillary driven system and integrated microelectrodes for n-DEP focusing force.

3.7   Chip preparation

One of the main objectives of this work is to enable on chip microparticle sensing without the need for external pump or syringe systems. The surface of SU-8 photo epoxy is insufficiently hydrophilic in its native state to enable the capillary driven of, for example, deionized water (DI) or phosphate buffered saline (PBS) based fluids, as these liquids make up the majority of the content in samples based flow cytometry. Therefore, it is necessary to modify the surface of the SU-8 to increase the hydrophilicity. Sobiesierski et al. (2015) have shown that two-stage SU-8 surface treatment can provide long term hydrophilicity [23]. The details of both stages, the first stage that renders the surface of the SU-8 hydrophilic and the second stage that extend the duration of the effect to in excess of 90 days, are as reported in [23]. However, in this work only the first stage oxygen (O_2) plasma treatment has been used, because at this stage of this research there is no need for a long stability treatment. A low-power O_2 plasma was applied to the samples using a reactive-ion etching (RIE) system within the clean room at Cardiff University by an Optoelectronic Devices Physics Group (OEDPG) member who is trained on this process. The sample is directly placed on a 4-inch carrier substrate inside the RIE kit, an O_2 plasma at a chamber pressure of 10 mTorr with an etching power of 100 W is applied to the chip for 60 seconds. The application of the surface treatment enables microfluidic driven by capillary action through the 3D embedded microchannel for water based fluids.

3.8 Cleaning

Normally, several cleaning steps are required during the fabrication stage of the microfluidic chip, before and after its actual test. In this work, following each test, the device was cleaned. It was found that the immediate submersing in the beaker filled with DI water results in an effective cleaning compared with for example only using a pipette to drop a small amount of DI water on the surface of the microchip. The device cleaning step is checked under the microscope, repeated with fresh water if necessary, then the sample placed on a hot plate for ~ 5 minutes to dry before we leave it in room temperature ready for a plasma treatment for the next use. However, we have found that the cleaning procedure depends on whether the surface of the used sample only has become hydrophobic or that the microfluidic chip significantly blocked from a previous test. For example, the microparticles block the main entrance of the 3D microchannel and/or along the length of the microchannel. In some devices the microparticles highly stuck together and to the microchannel's walls which makes not only the above cleaning process but also using the ultrasonic bath for 2 - 10 seconds ineffective. Such a problem is illustrated in Figure 3-12.
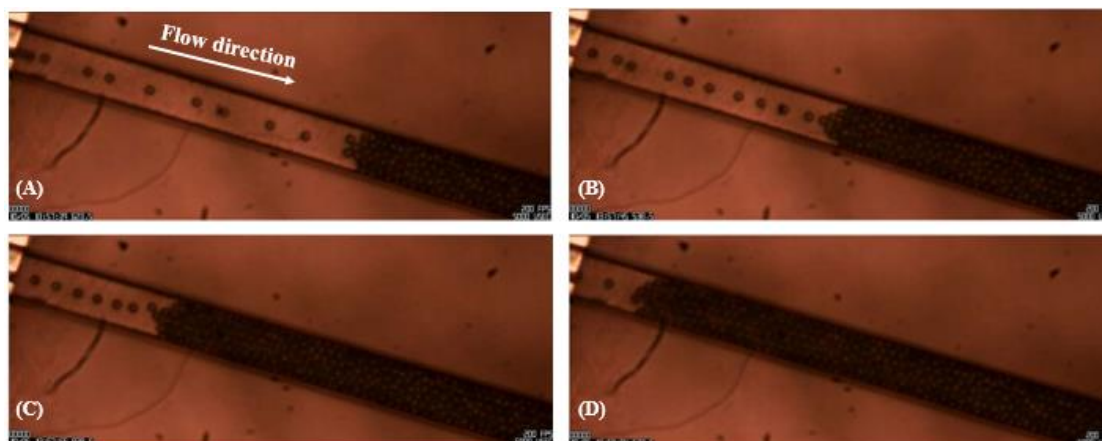
Figure 3-12 Photographs of 10 μm polystyrene microparticles flowing under the n-DEP force. The blockage of the 3D microchannel starts from a point downstream and out of our recorded window, and the microparticles start building up all the way along the length of the microchannel. However with the proposed two stage cleaning process the sample is successfully reused for further research. Photographs are from different frames extracted from the high speed camera. The time on each frame is 13:57:39, 13:57:45, 13:57:56 and 13:58:04 from A to D.

Therefore, a two stage cleaning process is proposed and demonstrated. First, the surface of the SU-8 is modified with an oxygen plasma for 1 minute, which renders

the surface of SU-8 hydrophilic, immediately followed by the use of ultrasound bath for no more than 2 seconds. This is found to be the most effective cleaning step with no damage for the device structure This method of cleaning improves the device lifetime, which allows for reusing it for multiple experiments.

3.9   Summary

This chapter has described the design concept along with the fabrication process steps that have been developed to create microparticle manipulation and control for on-chip integrated optoelectronics. In this work we looked at the key challenge and major improvement toward integrating metallic microelectrodes under and above the 3D capillary driven system that would create a non-uniform electric field, capable of focusing different sizes microparticles in flowing fluid into a single stream via DEP. The target is that in continuous flow microparticles regardless of their different size would have the same reference position relative to the centre of the channel. Key aspects of this work were; i) the use of SU-8 3005 to improve adhesion of Cr/Au layer to the GaAs substrate and critical to define microelectrodes above the 3D microchannel, ii) the use of SU-8 2002 as a base of the microchannel to offer electric isolation and physical separation from lower microelectrodes, and also to reduce the deep etched microfluidic foundation into the GaAs material, iii) the use of SPR 220-7.0 positive photoresist in conjunction with an adhesion promoter HMDS to fabricate the top microelectrodes instead of S1813 positive photoresist and a shadow mask and iv) the development of two stage cleaning process that improves the lifetime of the sample in use and also reduces the timescale and cost per experiment.

3.10   Bibliography

[1]   R. Thomas, A. Harrison, D. Barrow, and P. M. Smowton, "Photonic integration platform with pump free microfluidics," *Opt. Express*, vol. 25, no. 20, p. 23634, 2017.

[2]   H. Cai and A. W. Poon, "Optical trapping of microparticles using silicon nitride waveguide junctions and tapered-waveguide junctions on an optofluidic chip," *Lab Chip*, vol. 12, no. 19, pp. 3803–3809, 2012.

[3]   H. C. Tekin and M. A. M. Gijs, "Ultrasensitive protein detection: A case for microfluidic magnetic bead-based assays," *Lab Chip*, vol. 13, no. 24, pp. 4711–4739, 2013.

[4]   M. Tanyeri, M. Ranka, N. Sittipolkul, and C. M. Schroeder, "A microfluidic-based hydrodynamic trap: Design and implementation," *Lab Chip*, vol. 11, no. 10, pp. 1786–1794, 2011.

[5]   H. R. Nejad, O. Z. Chowdhury, M. D. Buat, and M. Hoorfar, "Characterization of the geometry of negative dielectrophoresis traps for particle immobilization in digital microfluidic platforms," *Lab Chip*, vol. 13, no. 9, pp. 1823–1830, 2013.

[6]   H. Shiono, T. Matsui, T. Okada, and Y. Ito, "Single-step enrichment of basophils from human peripheral blood by a novel method using a Percoll density gradient," *J. Sep. Sci.*, vol. 39, no. 15, pp. 3062–3071, 2016.

[7]   S. Chen *et al.*, "Electrically pumped continuous-wave III-V quantum dot lasers on silicon," *Nat. Photonics*, vol. 10, no. 5, pp. 307–311, 2016.

[8]   Datasheet, "SU-82000DataSheet2000_5thru2015Ver4.pdf," 2015.

[9]   F. J. Blanco *et al.*, "Novel three-dimensional embedded SU-8 microchannels fabricated using a low temperature full wafer adhesive bonding," *J. Micromechanics Microengineering*, vol. 14, no. 7, pp. 1047–1056, 2004.

[10]   B. F. E. Matarèse, P. L. C. Feyen, A. Falco, F. Benfenati, P. Lugli, and J. C.

Demello, "Use of SU8 as a stable and biocompatible adhesion layer for gold bioelectrodes," *Sci. Rep.*, vol. 8, no. 1, pp. 1–12, 2018.

[11]   M. Nordström, A. Johansson, E. S. Noguerón, B. Clausen, M. Calleja, and A. Boisen, "Investigation of the bond strength between the photo-sensitive polymer SU-8 and gold," *Microelectron. Eng.*, vol. 78–79, no. 1–4, pp. 152–157, 2005.

[12]   V. Mulloni *et al.*, "Gold-based thin multilayers for ohmic contacts in RF-MEMS switches," *Microsyst. Technol.*, vol. 18, no. 7–8, pp. 965–971, 2012.

[13]   M. Todeschini, A. Bastos Da Silva Fanta, F. Jensen, J. B. Wagner, and A. Han, "Influence of Ti and Cr Adhesion Layers on Ultrathin Au Films," *ACS Appl. Mater. Interfaces*, vol. 9, no. 42, pp. 37374–37385, 2017.

[14]   D. Holmes, H. Morgan, and N. G. Green, "High throughput particle analysis: Combining dielectrophoretic particle focussing with confocal optical detection," *Biosens. Bioelectron.*, vol. 21, no. 8, pp. 1621–1630, 2006.

[15]   K. Khoshmanesh *et al.*, "Dielectrophoretic manipulation and separation of microparticles using curved microelectrodes," *Electrophoresis*, vol. 30, no. 21, pp. 3707–3717, 2009.

[16]   H. Morgan, D. Holmes, and N. . Green, "3D focusing of nanoparticles in microfluidic channels," *IEEE Proc. nanobiotechnology*, vol. 152, no. 6, pp. 207–211, 2003.

[17]   R. Thomas, "Monolithic coupled-cavity laser diodes for bio-sensing applications," *PhD thesis*, no. Cardiff University, Cardiff, 2012.

[18]   S. Gillgrass, "LASER HAEMOCYTOMETER," *PhD thesis*, no. Cardiff University, Cardiff, 2018.

[19]   J. M. Dykes *et al.*, "Creation of Embedded Structures in SU-8," *Proc. SPIE*, vol. 6465, no. January 2014, pp. 64650N-64650N–12, 2007.

[20]   J. Golden, H. Miller, D. Nawrocki, and J. Ross, "Optimization of Bi-layer Lift-Off Resist Process," *CS MANTECH Conf.*, no. 617, 2009.

[21] S. O. Procedure, "Standard Lithography," *Nanofabrication Handb.*, vol. 73246, no. 617, pp. 2–6, 2012.

[22] P. Lamarre and R. Mctaggart, "A Positive Photoresist Adhesion Prometer for PMMA on GaAs MESFET's," *IEEE Trans. Electron Devices*, vol. 37, no. 11, pp. 2406–2408, 1990.

[23] A. Sobiesierski, R. Thomas, P. Buckle, D. Barrow, and P. M. Smowton, "A two-stage surface treatment for the long-term stability of hydrophilic SU-8," *Surf. Interface Anal.*, vol. 47, no. 13, pp. 1174–1179, 2015.

Chapter 4

THREE DIMENSIONAL DIELECTROPHORESIS CAPILLARY DRIVEN FOCUSING SYSTEM

4.1 Introduction

Capillary driven microfluidic devices have been used to handle fluids [1]–[3] with inherent advantages such as, but not limited to, pumpless systems. Such a system would highly increase the possibility of generating small size and low cost lab-on-chip devices suitable for individual laboratories and point-of-care (POC) applications. However, the fluid motion and the particles' position within the fluidic network is less controlled than those with an external pump [4][5]. Variation or lack of control of the microparticle position will reduce the functionality of the envisaged on chip light scattering measurement due to the probability of two microparticles or a large cluster passing the detection region together. In pump driven microfluidics the dielectrophoretic force has been widely used to move, sort and also to focus particles within a flowing fluid stream either in two or three dimensions and at user defined flow rate [6]–[10]. In this chapter, experiments to investigate the performance of a prototype dielectrophoretic microparticle control system for application with capillary driven microfluidics are described. In particular, the ability of the proposed microelectrode focusing section to generate negative dielectrophoretic (n-DEP) force

perpendicular to the laminar flow and strong enough to align and concentrate microparticles, such as cells, within a flowing fluid stream at the centre of a microchannel for scattering measurements is examined. We will investigate the strength of the DEP force and its potential to align and concentrate microparticles at the centre of the 3D microchannel with the intention of using in a future (final) fully integrated device for laser scattering measurements.

This chapter presents the samples (polystyrene microparticles), experimental setup and data analysis approach for this and the next chapter, and the theoretical and experimental results in which the most effective response of microparticles to the n-DEP force was observed. The experimental results are organized as follows: Section 4.5.2 presents the response of 6 µm polystyrene particles under the negative dielectrophoretic force. This experiment studies n-DEP effect across the width (side – to – side) of the microchannel (n-DEP$_{X\text{-axis}}$). This done to validate the strategy and to compare the performance of the system to those that follow with n-DEP across the width and height of the 3D microchannel. Section 4.5.3 provides information about the influence of any reduction in the length of the microelectrode focusing section on microparticles behaviour. Section 4.5.4 highlight the minimum applied frequency to generate an n-DEP response. Section 4.5.5 displays the toggling effect of applied AC potential on microparticles response to demonstrate the degree of focussing that can be achieved. Section 4.5.6 demonstrates a 10 µm polystyrene particles response to the applied AC potential, and section 4.5.7 presents the 6 µm microparticles distribution to be compared with 10 µm.

4.2 The samples (polystyrene microbeads)

5.7 ± 0.06 µm (hereafter labelled 6) and 9.9 ± 0.09 µm (hereafter labelled 10) diameter polystyrene (PS) beads (also referred to as microparticles in this work) are employed as test samples for the experimental work to examine the prototype performance. The microparticles were purchased from ThermoFisher scientific. They were supplied as part of a non-fluorescent flow cytometry size calibration kit, containing a set of beads of six different diameters each as 1mL suspensions in (deionized) DI water containing 0.05% Tween® 20 and 2 mM sodium azide, at a density of approximately 2×10^7

beads/mL. The DI water used for the samples, according to the manufacturer, has a resistivity of 18 MΩ.m (which means a conductivity of about 0.0556 µS/m).

Here we used 6 and 10 µm polystyrene particles out of the available kit, of 1, 2, 4, 6, 10 and 15 µm in diameter. This is to assess how biological cells, and mainly white blood cells (WBCs) [11] which the prototype aims to analyse in the future, might flow within the fabricated 3D capillary microfluidics based on volumetric similarity. Larger microparticles, within the purchased set, were avoided in order to reduce the possibility of blocking of the main microchannel and creating a problem with microchannel cleaning (increase the lifetime of the chip in use). Although smaller particles are less likely to cause blockage of the main channel, they are harder to monitor and analyse (resolution problem) using only an optical microscope and a high speed camera, due to the resolution limitations of the experimental setup.

4.3   Experimental setup

An optical microscope and a high speed camera (Mega Speed, Model MS60K-AB), connected to a computer with control software, are employed to monitor and record the dynamical behaviour of the microparticles. The viewing area can be chosen to be a maximum of 2304×1720 pixels, which is about 1696×1266 µm when installed on the optical microscope objective lens and calibrated relative to a known dimension on the chip. The dimension used is the width of the microchannel. Using a very high frame rate decreases the available recording time significantly unless the viewing window is decreased. However, with a smaller window, the covered region is unsuitable for subsequent data analysis. In this work, a viewing window of 1280 x 480 pixels with 200 frames per second (FPS) corresponds to about 35 seconds in total recording time, after which the camera system overwrites data. This memory constraint causes limitations in the number of events available to evaluate device performance. In practice, this limits the number of microparticles observed under the influence of the n-DEP force. In addition, we will not be able to record over the full duration of the experiment and therefore may miss information, if for example, the velocity of the fluid changes with time, longer than 35 seconds.

The required AC potential was provided by a function generator (AFG3101C), and an amplifier, which is used to generate a required voltage and current at a given frequency. The prototype fluidic chip is positioned on a copper block and within a space in a printed circuit board (PCB) that houses 24 electrical connectors. The in house-made-amplifier is connected to the microchip chamber via cables. Electrical connections to the individual microelectrodes are made utilizing a wedge wire bonder to bond 30 µm diameter aluminium or gold wires from the chromium/gold (Cr/Au) microelectrode to the PCB. An oscilloscope (Tektronix, TDS 2014) was employed to read the amplified sine wave. A general diagram and a photograph of an overall experimental apparatus can be found in Figure 4-1 and Figure 4-2, respectively. A laboratory micropipette (RAININ) was used to load the solution droplet at the inlet reservoir. Two methods are used to analyse and identify the strength and complexity of mechanisms involved as introduced in the next section.

1. High speed camera
2. Microscope with Objective lens
3. Microchip on holder
4. PC
5. Function generator
6. Oscilloscope
7. Amplifier
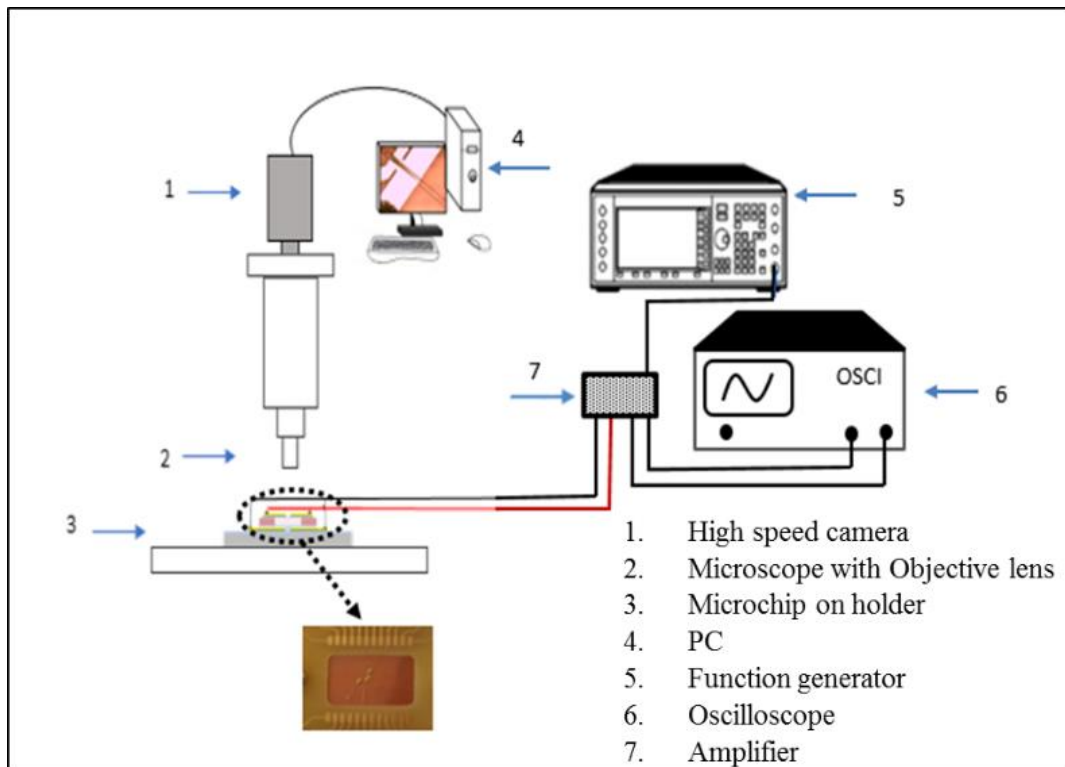
Figure 4-1 A diagram of the experiment setup illustrating general sketches of the connections.
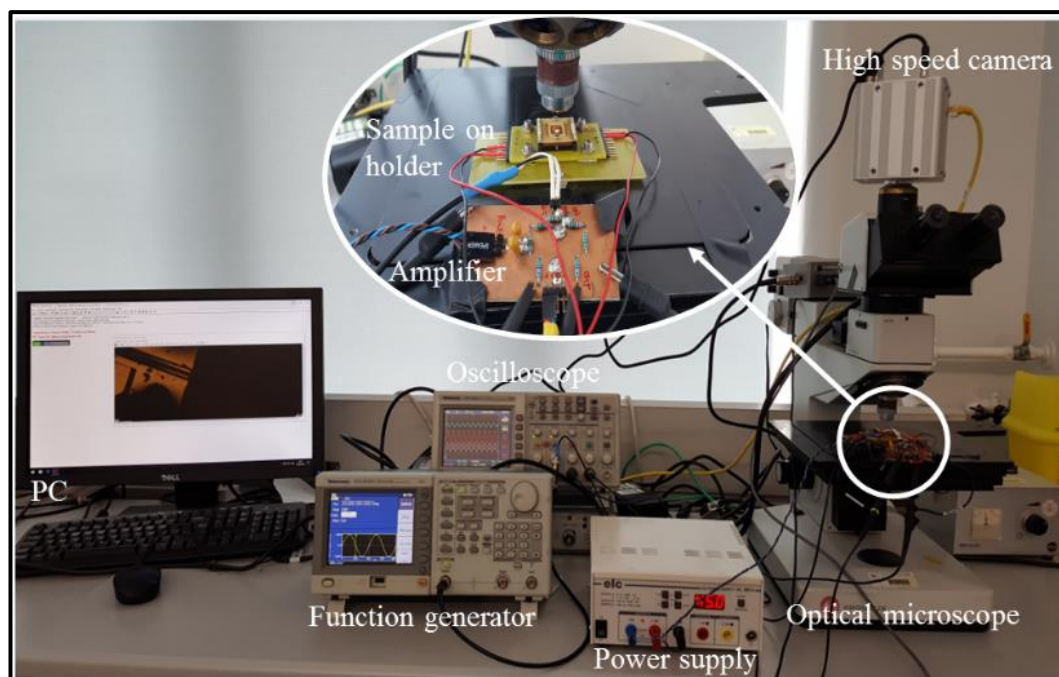
Figure 4-2 A photograph of the experimental setup of the microfluidic prototype.
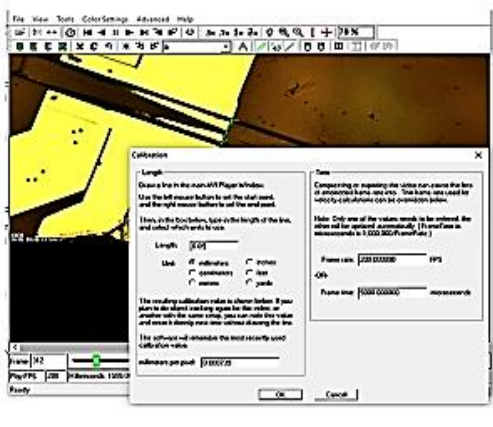
4.4 The case study methods

For the purpose of analysis two methods were used; i) object tracking tool in the camera software and ii) a code written and developed in MATLAB R2018a software. Using the object tracking tool in the camera software, the first step is to calibrate the scale according to a known object length in the recorded video. Then the centre mass of each microparticle was found using the right mouse click at three different points (frames) after the narrower edge of microelectrodes and along the available length of the microchannel in the AVI format. Figure 4-3 shows a flow graph of the tools used in a recorded video for obtaining velocities. The measured velocities of microparticles are plotted and discussed in a later chapter (chapter 5).
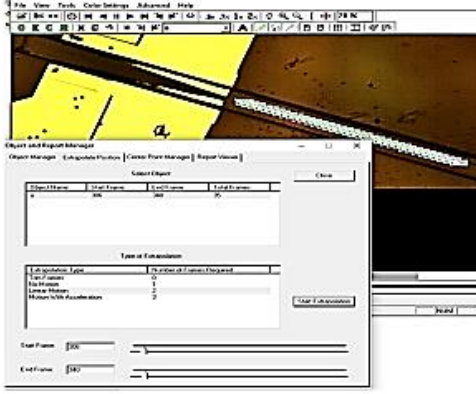
A MATLAB R2018a software was used for the processing of frames from the camera image software. Using in-built software, code written with MATLAB R2018a software, the two dimensional tracking measurements were carried out by detecting the centre mass of each particle throughout two different windows. By calculating the time interval each particle took to cross the distance between the selected windows, the velocity can be calculated.
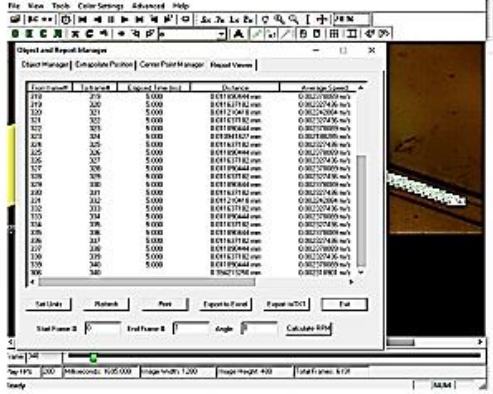
1. Open the 'Calibration' dialog
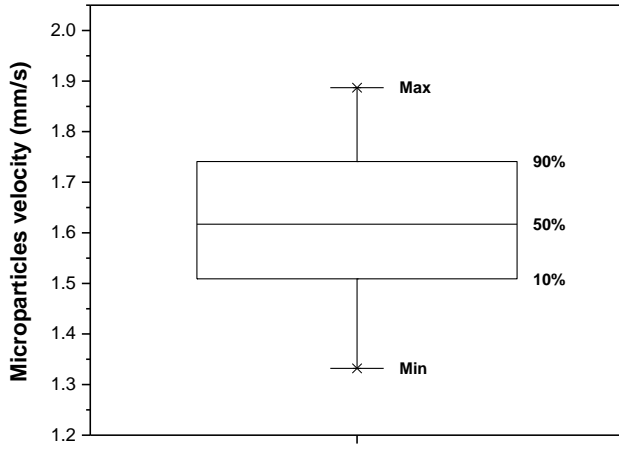
2. calibrate the scale

3. Object tracking points will be assigned to the active object

4. Report with data about the motion of the active object

Export to Origin 2017

Figure 4-3 Procedure for obtaining velocities, using object tracking tool in AVI format.

In our proposed method, Ptrack.m read each frame in JPEG format in order to estimate microparticle horizontal position. The frames were obtained by exporting a recorded video in AVI format to JPEG. To allow for easier data analysis, it is crucial to have the best possible quality video evidence. Therefore, the video data was taken with 200 frames per second. This is because there is a compromise between frame size, image quality and size of the video. The data was a sequence of approximately 6600 1280-by-480 colour JPEG image, because of the limitation of the internal memory of the high-speed camera. The JPEG images had colour values in a RGB (Red, Green and Blue) intensity within [0, 255], and the polystyrene microparticles of 6 and 10 μm in diameter had an observed diameter of approximately 4.5 and 7.4 pixels, respectively. Each image contained a number of distortions, either related directly to an uneven light source or some accidental effects such as touching the device and causing vibrations while injecting the test sample into the inlet reservoir. The device was secured on a flat surface and maintained in a horizontal position as much as possible, but this surface was not vibration-free, and it can be a further source of distortion.

As a part of processing, the individual frames were transformed to grayscale; then they were subtracted from the background image before they were subsequently converted into type uint8 (converts the intensity image "IM" to uint8 and rescaling the data if necessary). The frames were segmented by thresholding. As a result, any pixels above the intensity threshold were labelled as 'object' and the remains as 'background'. The frames were then filtered using the bwareaopen (BW, P) MATLAB function, which removes all distortions whose size is less than P pixels from the image, and hence avoiding unreal particle detection. Figure 4-4 shows the steps proposed for processing the input image. The result of applying the tracking method, for each microparticle, was a position estimate that was derived by computing the coordinates of the centroid. Velocity was computed as the linear displacement between two different frames, in which the coordinates of the centrepoint were located. It is important to mention that the centrepoint may show a larger fluctuation in the case of substantial physical (shape) changes. Finally, computed velocities are plotted and analysed as a function of microparticle position within the channel width, experiment duration or as a function of detected number (frequency) as presented throughout this work.

Background image

Raw image / Input

Spot enhanced image / Output

Substracted image
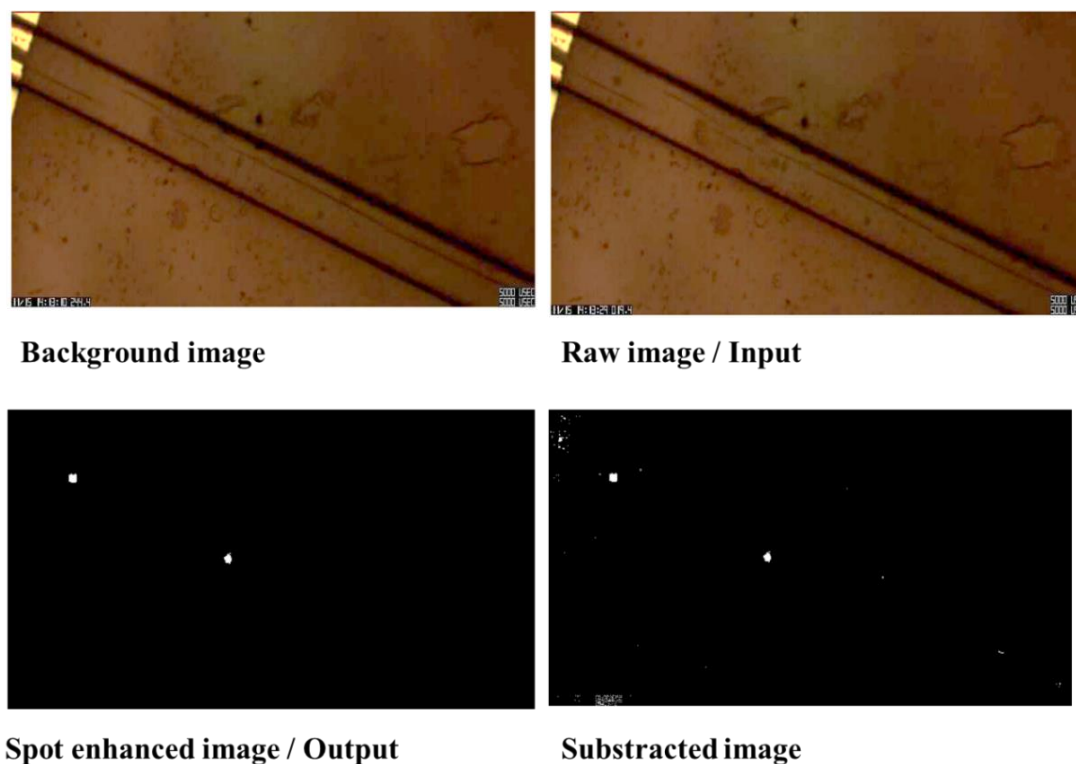
Figure 4-4 Procedure for obtaining the input image for data analysis using self-written software.

Note that, for the position measurements in the rest of this chapter, I will use the built-in software as it is easy to use, significantly faster than the manual testing process and does the job. In the next chapter, where I look at the microparticles velocity, the built-in method does not deal well with the completely random microparticles; the built-in technique does not capture all the points. Therefore, the method can not be used as I can not be sure that the same particle passed through the first window will pass through the second window. Particle's velocity varies based on its position inside the microfluidic channel. In chapter 5, the velocity of randomly distributed microparticles measured using the manual testing process (object tracking tools in the camera software) even though it is time consuming and it is not possible to reuse the manual test.

Also, Origin 2017 64 Bit was performed for some statistical analysis with respect to the number of the events captured. Because the distribution of our data is skewed and to reduce the influence of outliers, all the statistics are given in terms of median instate of the mean. Based on dividing the data set into the intensity for 90th percentile (90%) of events and intensity for 10th percentile (10%) of the events, the boxes enclosed 80%

of the data around the median line (50%), while the whiskers indicate the maximum, minimum, 99% and 1%. If the scale value for the 90% or 10% of data is off-scale, then the robust standard deviation (RSD $=$ $\frac{(\text{intensity at 90\%} - \text{intensity at the median}) + (\text{intensity at the median} - \text{intensity at 10\%})}{2}$), and the robust coefficient of variation (RCV $= \frac{(\text{intensity at 90\%} - \text{intensity at 10\%})}{2 \times \text{intensity at the median}} \times 100$). The experimental circumstances and results of each prototype are presented and discussed in detail in the following sections.

4.5   Results and Discussions

4.5.1   Theoretical calculation

The polarisation of dielectric particles is frequency dependent as described in Chapter 2; therefore particles may experience a force driving them away from the high electric field region at certain frequencies, n-DEP, and may experience the opposite, p-DEP, at other frequencies [12]–[16], while the dielectric properties of the surrounding medium remain unchanged. Herein, the minimum frequency of the applied electric field in which the dielectrophoretic force falls to zero, which refers to the crossover frequency, and switches from p-DEP to n-DEP response, on the behaviour of the microparticles, can be estimated. This is predicted by calculating the real part of the Clausius-Mossotti (CM) factor, after extracting it from equation ($f_{(CM)} = (\varepsilon_p^* - \varepsilon_p^*)/(\varepsilon_p^* + 2\,\varepsilon_m^*)$), as shown in Figure 4-5. In calculating the real part of the CM factor, values of 2.5 and 78 were used for the relative permittivity of the polystyrene microparticles and the DI water respectively. The conductivity of the polystyrene microparticles, σ_p, can be estimated from the sum of the bulk, σ_b, or core conductivity and the surface conductivity, σ_s, [17], [18] The bulk conductivity of the polystyrene microparticles of radius R can be assumed to be zero, the influence of surface conductance can govern over the bulk one for micron-sized particles as mentioned in chapter 2, and hence the particle conductivity, σ_p, can be written as equation ($\sigma_p = \sigma_s = 2K_s/R$), where K_s is the surface conductance of the microparticles. Values of 0.0556×10^{-6} and 1.1×10^{-3} S/m were used for the conductivity of DI water and 6 µm

polystyrene microparticles (using a value of surface conductance of 1.65 nS [17]) respectively.
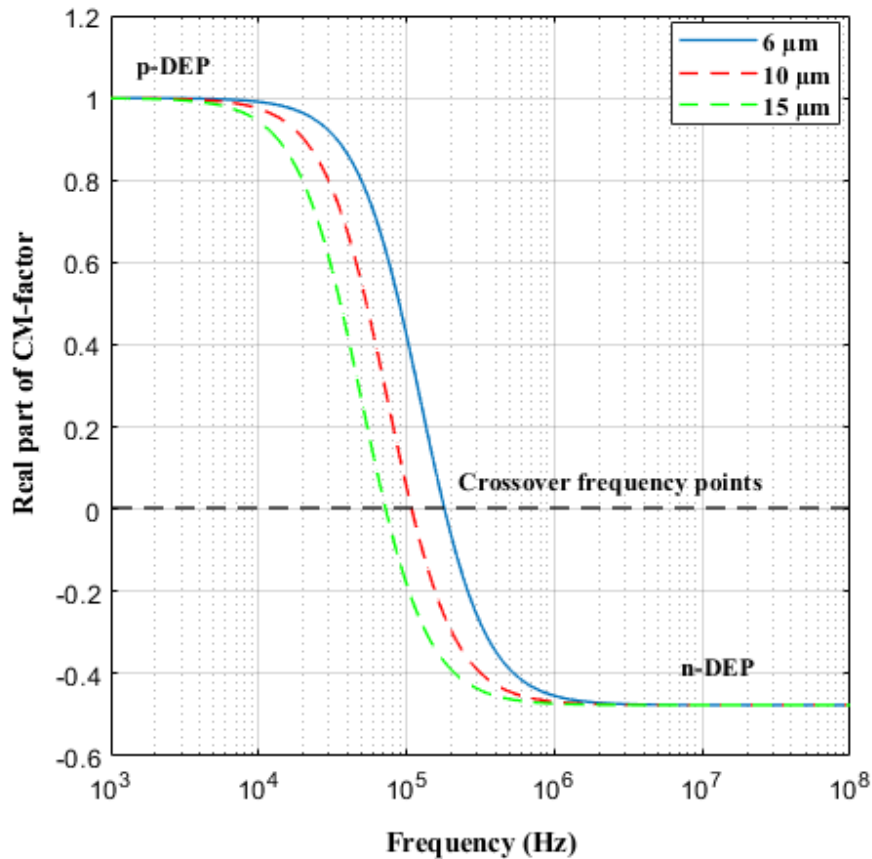
Figure 4-5 DEP and CM-factor as a function of frequency, for 6, 10 and 15 µm polystyrene particles suspended in DI water, calculated with a code written in MATLAB.

The plot shows that the 6 µm, 10 µm and 15 µm particles experience p-DEP force for respective frequencies below about 0.20 MHz, 0.11 MHz and 0.07 MHz, respectively. These are the crossover frequency values of the three different sized microparticles and are indicated by the black dashed line in Figure 4-5. Above these frequencies, all microparticles experience an n-DEP force. It is worth mentioning that the crossover frequency is used to control the separation of different particles, such as cells within a mixture [16]. Although the size dependence is not apparent in the real part of the Clausius-Mossotti equation, it is enclosed within the particle conductivity term, in equation (2.26). Also, the plot shows that the real part of the CM factor is constant and close to - 0.5 at frequencies in the MHz region, in which a strong n-DEP force is expected. Note that, due to the shortage of information, the value of surface conductance of the employed microparticles has been borrowed from [17] even though

it is for microparticle of a different size than the ones used here. The effect that the surface conductance has on the DEP spectrum and crossover frequency is shown in Figure 4-6. Here, the surface conductance value used in CM factor calculation has been varied by $\pm 10\%$, $\pm 25\%$ and $\pm 50\%$ (from 1.65 nS) to compute the effect.
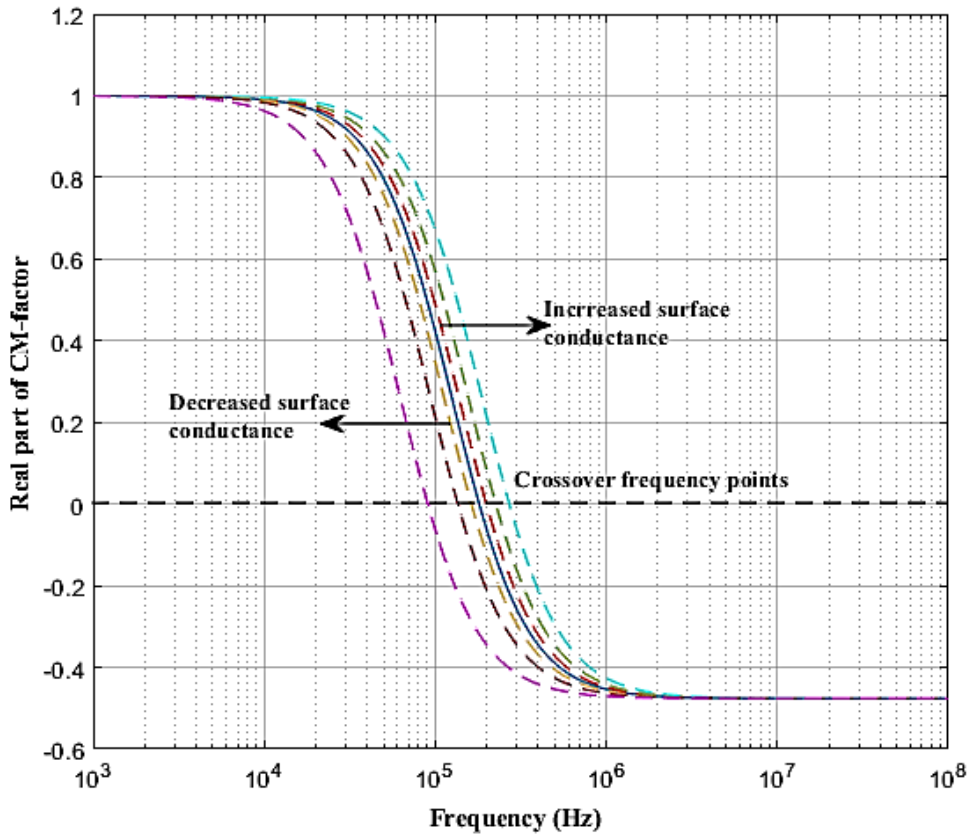
Figure 4-6 Estimation plot showing the DEP spectrum and the variation in crossover frequency for 6μm PS beads with different surface conductance. Value of 1.65 nS used for surface conductance and the DEP spectrum is represented by the blue line. This value then varied by ± 10%, ± 25% and ± 50%. The increase in the surface conductance value and its effect on the DEP spectrum is represented by red, green and turquoise dashed lines. While the decreased in values and the impact on the DEP spectrum is indicated by orange, maroon, and pink dashed lines.

Microparticles with surface conductance of ten, twenty-five and fifty times higher than that of microparticle type A (denoted by the blue line), and their effect on both DEP spectrum and crossover frequency, are presented by red, green and turquoise and black dashed line respectively. While the impact of decreasing surface conductance by ten, twenty-five and fifty times lower than that of the microparticles type A are presented by orange, maroon and purple dashed lines respectively. The simulation shows a very slight shift in the crossover frequency, with these large changes in surface conductance

value; therefore, the uncertainty in this value can be tolerated. In addition, these results highlighted the required range of applied frequency to influence the dynamic behaviour of polystyrene microparticles inside the microchip as it shall be investigated in the next sections.

4.5.2 DEP response on microparticles behaviour

In this section, evidence of the ability of microelectrodes to generate an n-DEP force on microparticles and influence their behaviour is presented. Approximately 1 µL of the sample, with 6 µm polystyrene particles suspended in DI water, is injected into the inlet of the fluidic system. The example advanced into the channel through capillary action. This is achievable, as mentioned in chapter 3, on the SU-8 hydrophobic platform via the oxygen plasma treatment [19]. During the experiment, the combined contribution of laminar fluid flow and n-DEP focusing force is used to position the microparticles. An AC potential of 17.8 volt peak-to-peak, V_{p-p}, at frequencies of 10, 20, 30, and 40 MHz were applied across the microelectrodes (stable sinusoidal voltage output at the frequency of the supply). For 10, 20 and 30 MHz no clear effect was seen, but at 40 MHz, the microparticles interacted with the generated electric field and pushed away from the channel's sidewalls and into the centre. However a wide distribution of approximately 35 µm, was observed. This is shown in Figure 4-7 where D1 and D2 are two selected viewing windows, very close to and further away from the narrow edge of the microelectrode focusing section and along the observed length of the microchannel which covers the whole viewing window from the high speed camera image software. The second window (D2) is chosen to be around the area where the laser sections will be in the final fully integrated device with lasers and photo-detectors for light scattering measurements.

The boxplot shows that, in such devices, 80% of the measured 83 microparticles over about 34 second period were found at a lateral position of about 27.01 ± 9.13 µm around the centre of the microchannel. This measurement is obtained through the first viewing window, D1, which is only few micrometres after the narrower edge of the microelectrodes. The same distribution was observed downstream through D2, about 315 µm further downstream and away from D1. This indicates that the majority of the microparticles were aligned around the centre of the microchannel, at ~ 27 µm (non-

zero, 25 µm, due to fabrication imperfection) and remain within the same streamlines as they are move by the n-DEP focusing force, downstream due to laminar flow. This is along with the available viewing window from the high speed camera and where lasers/photo-detectors might be in our intend device.
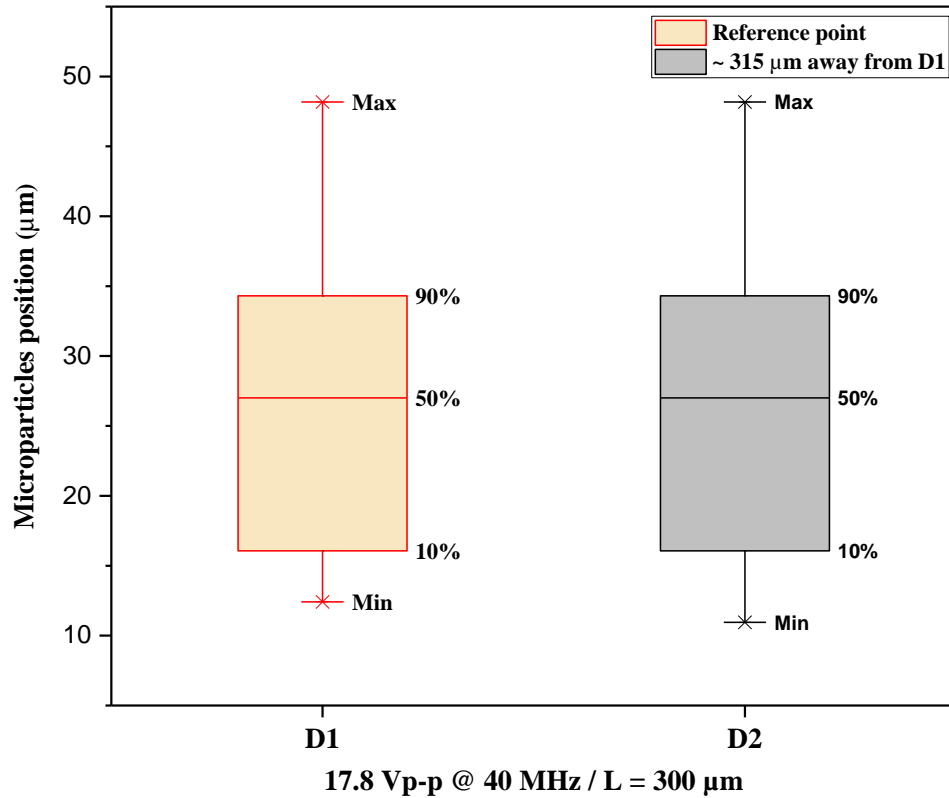
Figure 4-7 6 µm polystyrene microparticles distribution under the n-DEP force, where L is the active length of the microelectrodes and D1 and D2 are two viewing windows along the observed length of the microchannel.

Note that data from behaviour at 10, 20 and 30 MHz is not shown, due to no clear response was seen. This may be a result of insufficient n-DEP force at 17.8 V_{p-p}, even though the applied frequencies are higher than the predicted value within the simulation. In such a capillary system, assuming that in all cases the microparticles experience the same average velocity, the AC voltage may need to be in a higher range (DEP increases rabidly with applied voltage, see Chapter 2 Section 2.3.4) to achieve a better dynamic control during the experiment. The result of increasing the magnitude of the AC sine wave to 27.8 V_{p-p} at a frequency of 40 MHz, through observations of frames from the high speed camera for 6 µm polystyrene particles, are shown in Figure 4-8.
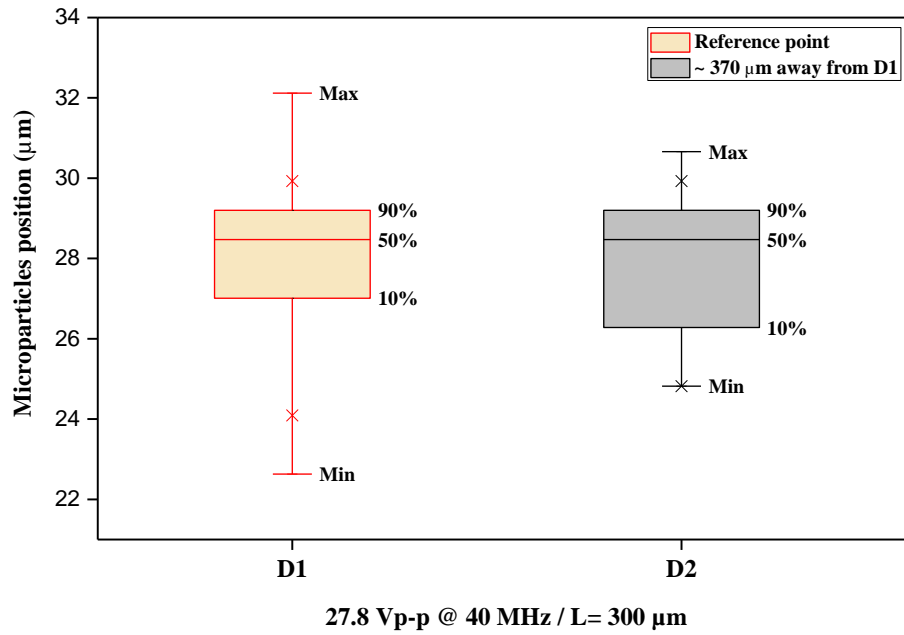
Figure 4-8 6 µm polystyrene microparticles distribution while operating the microelectrodes with an AC potential of 27.8 V$_{p-p}$ at 40 MHz, where L is the microelectrodes active length and D1 and D2 are two viewing windows along the channel's length.

Microparticles were clearly pushed further toward the centreline of the microchannel, and 80% of them were observed around the centre of the microchannel at 28.50 ± 1.10 µm and 28.50 ± 1.50 µm through the selected viewing windows D1 and D2, respectively. This was done for 107 microparticles, which were collected over the experimental duration of about 34 seconds from the used high speed camera. Again, we have shown that the microparticles in flow downstream remain focused after passing the AC potential regime as they are move under the n-DEP focusing force. Therefore, a significant improvement, fast and sufficient sorting and counting is expected compared to those without the DEP reported in [3]. Note that, the microparticles under the influence of DEP force were measured along the X-axis (side-to-side) only, regardless of their position along the Y-axis (vertical position), based on the observations from the extracted frames from the high speed camera. In addition, due to the polarity of the applied voltage across the microelectrodes, the top microelectrodes powered with an AC signal respect to the bottom microelectrodes, which are grounded, the horizontal microparticles position is only under the influence of focusing force. Table 4-1 summarizes the effect of generated n-DEP forces on a microparticle's dynamical behaviour from the calculated median and RSD through selected viewing windows.

Table 4-1 illustrates the measured median and robust standard deviation (RSD) of propagated particles along the channel's length while operating the microelectrodes with selected AC sine wave.

Attempt of experiment 1: 17.8 V_{p-p} @ 40 MHz				
Viewing window Along the channel's length	Distance from the narrow edge of the microelectrodes	Median (µm)	RSD (µm)	No of events
D1	Reference point	27.01	9.13	83
D2	315 µm away from D1	27.01	9.13	83
Attempt of experiment 2: 27.8 V_{p-p} @ 40 MHz				
D1	Reference point	28.50	1.1	107
D2	370 µm away from D1	28.50	1.5	107

Here, by increasing the applied AC potential, we have reduced the microparticles spread around the centreline of the microchannel. Microparticles influenced by the n-DEP force across the X-axis only, n-DEP$_{X-axis}$, are more likely to be at different altitude within the channel's depth and hence flowing with different velocities since variations in velocity with height arise due to the capillary flow. This increases the possibility of two microparticles or a larger cluster passing the detector together and being measured as one. Figure 4-9 shows some frames extracted from camera image software where two microparticles flow through the 3D microchannel with different velocities. It is thought that they are at a different height, and hence the first particle closer to the microelectrodes narrow edge (frame A) passes the second one as it might be closer to the top or bottom walls of the microchannel (in different focus). Then at some point they become very close (frame B) where the probability of being measure as one increases before passing (frame C). Vertical variation in microparticle position in the depth of the microchannel, Y-axis, could be better controlled through the cross (X) polarity of the applied voltage. This polarity would enable the generation of horizontal

and vertical n-DEP focusing forces required for realizing 3D focusing of microparticles which will guarantee only one particle passes through the detection region in the microchip. In particular, microparticles steady state lateral as well vertical position through the interrogation region ensure repeatable illumination uniformity, which leads to reliable detections and enhance microparticles sorting purity.
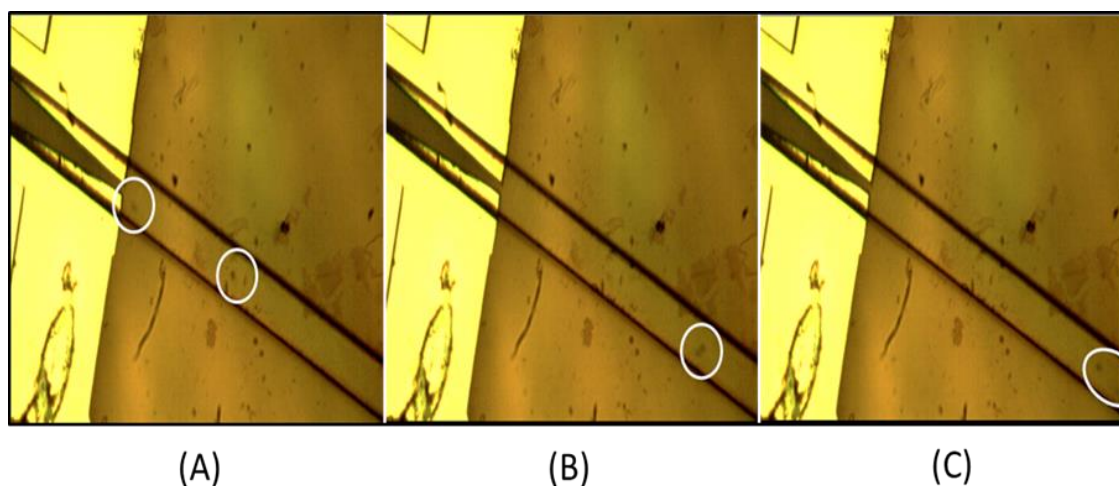
Figure 4-9 Photographs show the path of two particles flowing under the n-DEP$_{X-axis}$ force on a single image but in different stages of movement.

All the data was collected from videos recorded approximately 30 seconds after the drop of the sample come into contact with the fluidic network. The reason for this is that fluid velocity is changing very rapidly within the first 30 seconds and, as described in Chapter 2, fluid velocity has a major effect on the DEP force required to make focussing effective. Experiments confirm that fluid velocity after the first 30 seconds may still vary by a few mm/s but not to an extent that significantly affects the results. The fluid speed decreases with time in a capillary fill and, in general, the particles have the same velocity as the fluid [20], [21]. Although it is not shown here, particle velocities up to 5 mm/s, as presented in the next chapter, are acceptable through observations of frames from the high speed camera. Holmes et al [7] showed that they could not control particles in a pump system by DEP force with a fluid velocity in excess of 5 mm/s at an applied voltage of 20 V peak with a frequency of 10 MHz. The microelectrodes are designed with two platforms to drive down the total chip size as it shall be introduced in the next section.

4.5.3   Reduction in the length of microelectrodes and its advantages.

Any reduction in the length of the microelectrodes reduces total chip size and so is advantageous from an application and cost perspective. Data to examine the effect of the n-DEP force on microparticles behaviour as a function of the microelectrode's active length, with other variables unchanged is shown in Figure 4-10. A 20% reduction in the active microelectrode's length was proposed, designed and examined.
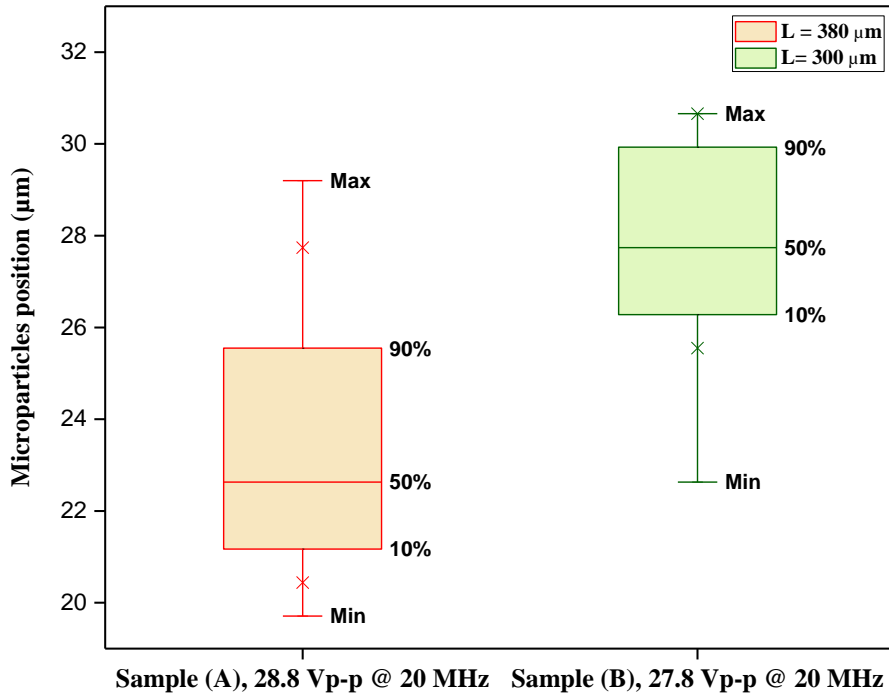
Figure 4-10 Distribution of 6 μm polystyrene microparticles with the voltage and frequency given in the caption, where L is the microelectrodes effective length.

In both experiments, the microdevices were experimentally tested over ~ 34.5 seconds with the same sized polystyrene microparticles. The results demonstrated effective n-DEP force on microparticles behaviour. Using sample A, it can be seen that the measured 105 microparticles were clearly concentrated around a central point of 22.63 ± 2.19 µm, not centred, 25 µm, due to fabrication misalignment, as shown in Figure 4-11. By using sample B, the measured 145 microparticles were aligned around a central point of 27.74 ± 1.83 µm. Based on the experimental observations, Sample A has a RCV of 9.67% and sample B has a RCV of 13.16%, we would say microparticles travelling through shorter microelectrodes focusing section were more tightly aligned around the centre of the microchannel, relative to its median. There is no significant

difference in microparticles distribution; this might be due to a very small increase (0.97%) in the aligning angle of microelectrodes focusing section. We conclude that the shorter microelectrodes within the proposed design can be used with the advantage of reducing the total size of the chip.
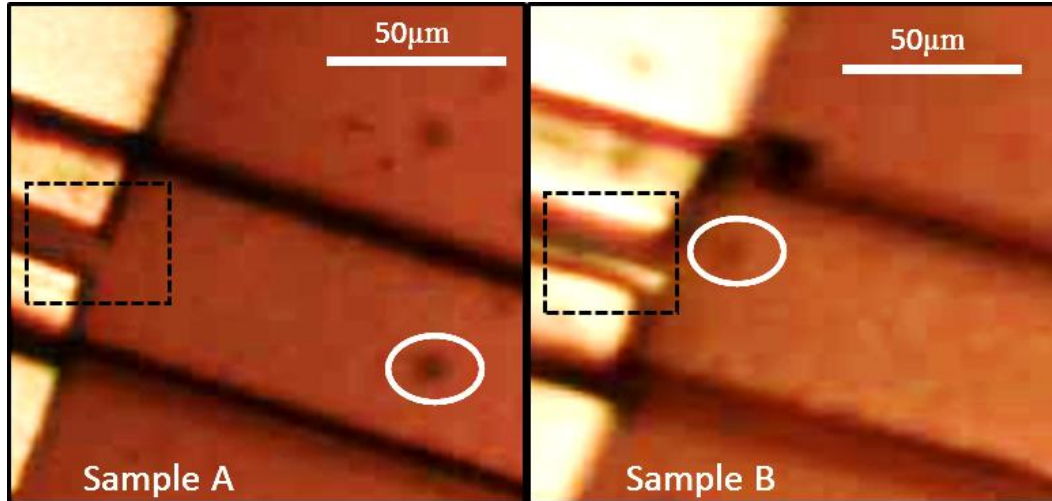
Figure 4-11 Images of sample A and B, obtained by Zooming in to the downstream edge of the microelectrode and, through extracted frames from the high speed camera, show flow of 6 μm polystyrene particles in the white circles with a lateral position around the centre of the microchannel. The small offset from the centre is due to fabrication misalignment which is indicated by the dashed black squares. The dashed black square in the image of sample A shows the microelectrodes do not line up with the centre of the microchannel. While the black dashed square in the image of sample B shows the top microelectrodes are not face-to-face with the bottom microelectrodes. Sample A and B images are for a prototype with 380 and 300 μm microelectrodes active length, respectively.

4.5.4   6 μm particles response at 1, 5, 10 and 24 MHz

Earlier, we experimentally show that the applied AC frequency is an important factor affecting the focusing process. In this section, the measurements were performed by increasing the frequency of the applied signal in three different steps (1, 5 and 10 MHz) not only to be compared with (24 MHz) but also to optimize a minimum frequency required to achieve a strong DEP focusing. In the first test, the same strategies were used, the microelectrodes were powered by an AC sinusoidal signal of 30 V_{p-p} while maintaining the flow of 6 μm polystyrene particles within a fluidic network by capillary action. Equal voltage was applied in a cross (X) - pattern to the

microelectrodes. As we said earlier this should result in horizontal (n-DEP$_{X\text{-axis}}$) and vertical (n-DEP$_{Y\text{-axis}}$) negative dielectrophoretic forces that are equal from each side to push the microparticles toward a single location where the strength of electric field's gradient is a minimum (the centre of the microchannel). The trajectories of microparticles were observed through extracted frames from the high speed camera and our code in MATLAB software, as shown in Figure 4-12. An n-DEP effect on the microparticle's behaviour is expected at 1 MHz as predicted by simulation work (see section 4.5.1). However, 80% of detected microparticles have a very wide width of approximately 34.00 µm over which they can distribute. When the frequency was increased to 5 a reduced spread of microparticles was observed (~ 18.00 µm) with the best focusing (~ 5.20 µm) at 10 MHz.
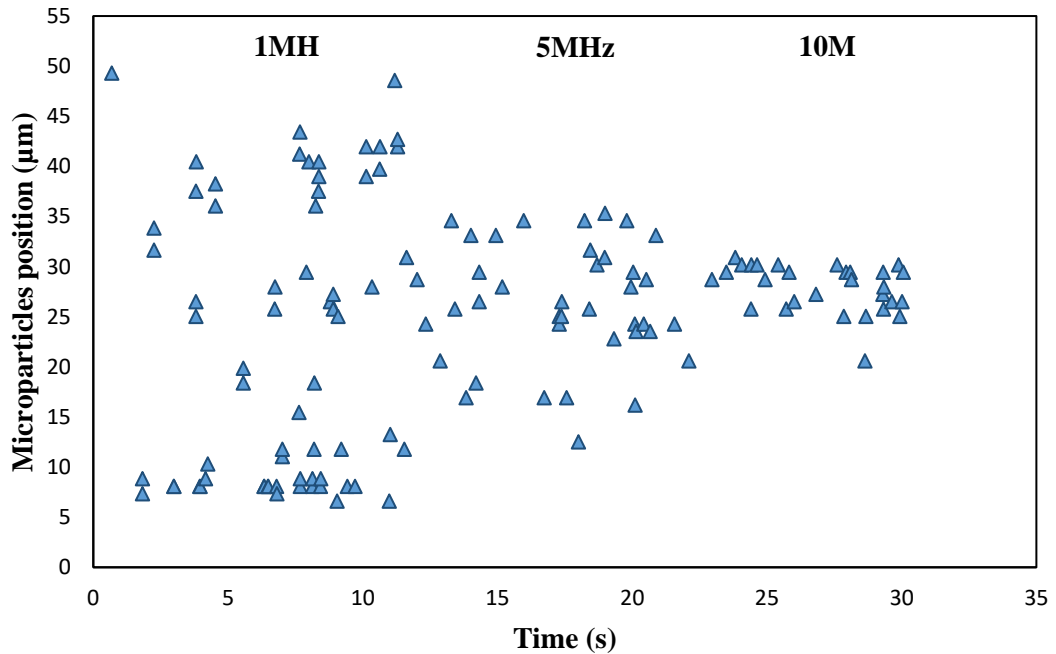
Figure 4-12 Distribution of 6 µm polystyrene particles with an AC signal of 30 Vp-p at frequencies of 1, 5 and 10 MHz. The frequency change is done with Labview control, 10 seconds for each run, written by Basmah Almagwashi.

In the second test, with a different sample, when the applied AC frequency was increased to 24 MHz, a slight improvement in the concentration of microparticles around the centre of the microchannel was observed. 80% of detected 175 microparticles were found at a lateral position of (23.23 ± 2.18 µm) in comparison with (28.70 ± 2.58 µm) for the 33 detected microparticles under a frequency of 10

MHz. We can understand this easily from the boxplot, Figure 4-13. The achieved result shows that microparticles can be highly aligned within the centre of the $(50 \times 27 \ \mu m)$ microcapillary with the applied voltage of 30 V_{p-p} and a minimum of 10 MHz.
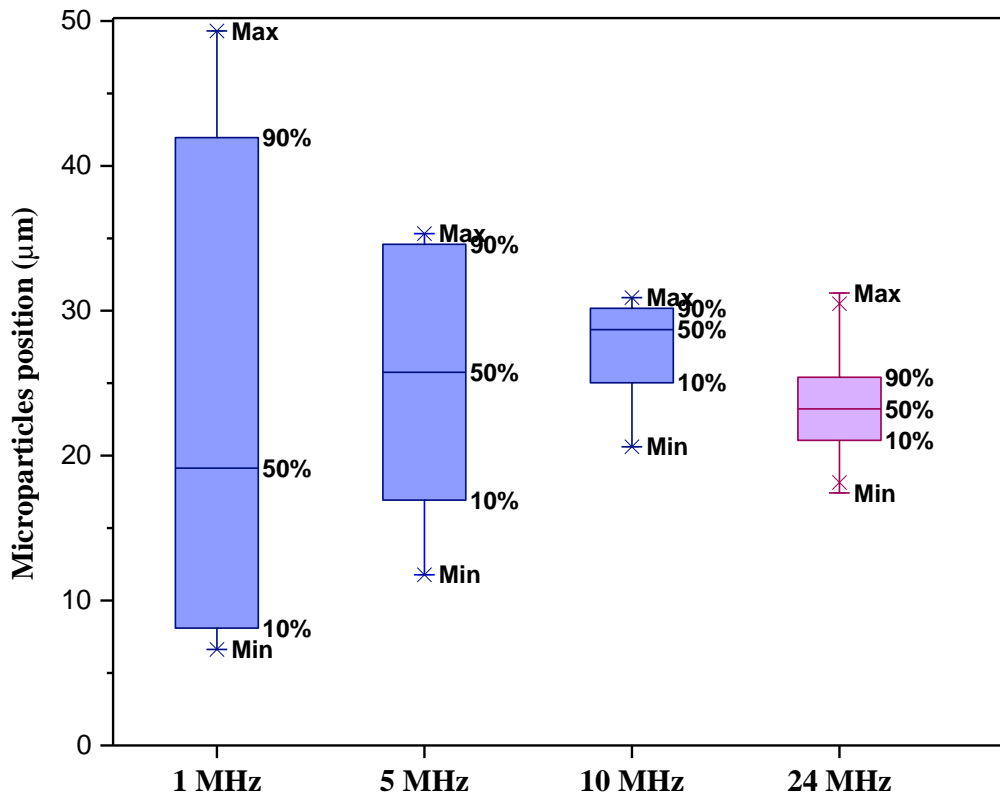
Figure 4-13 Distribution of 6 μm polystyrene particles under the n-DEP force generated by an AC potential of 30 Vp-p at different frequencies. Blue and violet refers to two different samples.

The positioning of microparticles under the n-DEP$_{Y-axis}$ cannot be confirmed through observations of frames from the high speed camera, but some indication that it is occurring is available. Particles that are in focus appear clearly through extracted frames from the high speed camera, and they become blurry when they are out of focus, due to their depth within the channel's cross section. This was used to assess whether the microparticles are affected by the n-DEP$_{Y-axis}$. Figure 4-14 shows photographs of particles from different frames without an n-DEP force field applied on the Y-axis. The 6 μm particle in the white circle is in focus while the microparticle in the purple circle is not, and this is believed to be due to the variation of their vertical position. Similarly, Figure 4-15 shows a photograph of particles from one frame, while zooming in along the channel. The two particles in the white square and the third one in the white circle are in different focus. When the signal is applied in the X-

configuration, there is no evidence of particles with a different focus. Hence better focusing can be simply achieved by changing the configuration of the applied voltage across the microelectrodes. In the following chapter, the vertical position of the particle under dielectrophoretic control is examined more quantitatively.
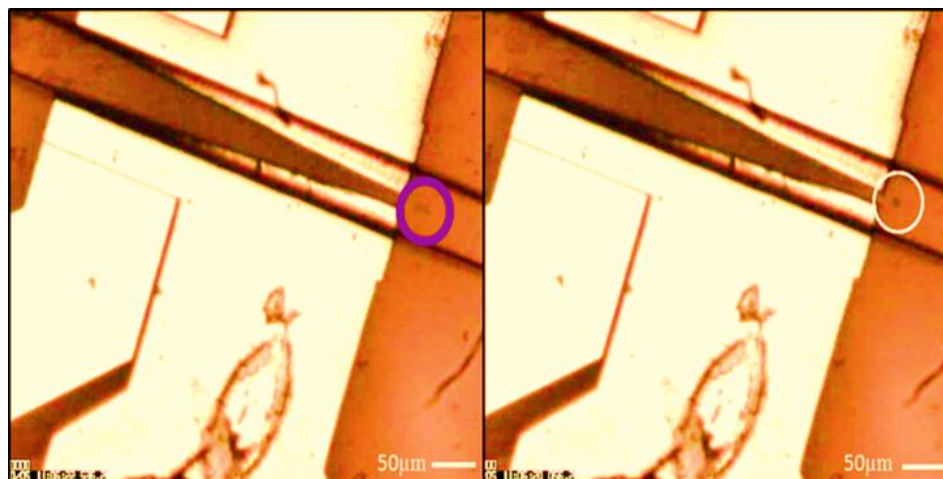
Figure 4-14 Photographs of two particles flowing under the n-DEP$_X$-axis force (from different frames).
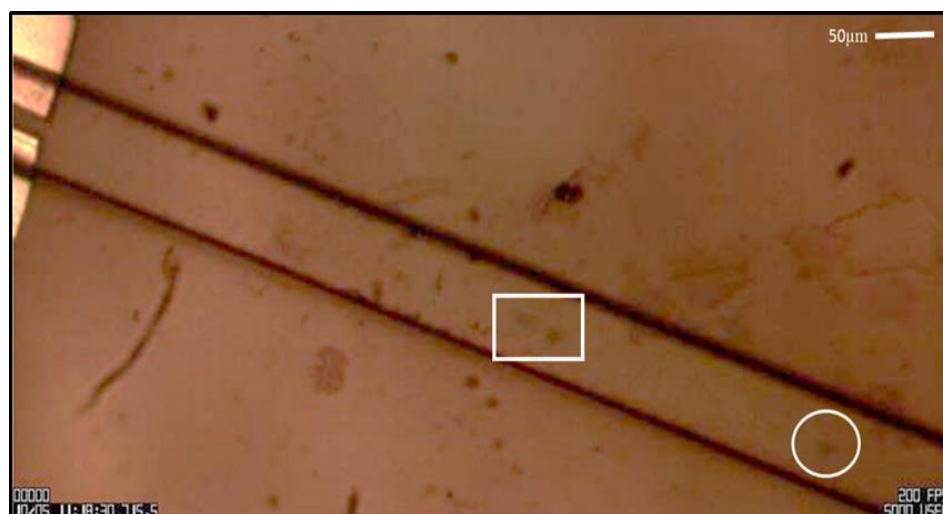
Figure 4-15 Photographs of three particles flowing under the n-DEP$_X$-axis force (zooming into the downstream along the length of the microchannel).

4.5.5   Toggling the applied AC potential and microparticle response

In order to compare directly the strength of n-DEP focusing force and its potential for applications with capillary systems, the distribution of polystyrene microparticles were

investigated while toggling AC function generator. The required values of applied voltage and frequency, in which an n-DEP response on microparticles dynamic behaviour can be observed, were recognised from the previous experiments. Therefore, with X-polarity of applied voltage, the microelectrodes were powered by an AC potential of 30 V_{p-p} at a frequency of 10 MHz. 34 seconds video of microparticles passing through the 3D embedded microchannel was recorded and analysed in MATLAB software. The results demonstrated a significant difference in the spread of the measured horizontal positions with and without the n-DEP focusing force, as shown in Figure 4-16.
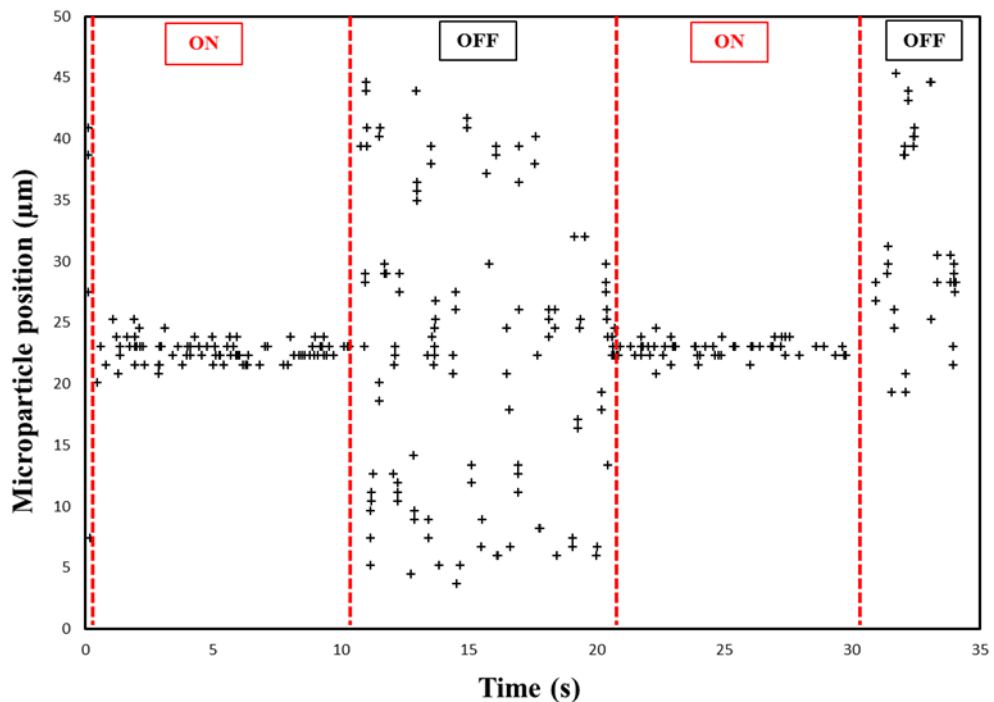
Figure 4-16 6 µm polystyrene microparticles distribution while toggling the applied AC potential of 30Vp-p at a frequency of 10 MHz. with a code written in MATLAB.

In the absence of the applied AC potential, the microparticles were randomly distributed over the whole width of the designed microchannel. Consequently, in such device (50×27 µm) at least three particles (6 µm in diameter) might pass the detector together and decrease the reliability and functionality of the ultimate microchip. On the other hand, under the AC potential application, all the recorded microparticles were pushed toward the centre of the microchannel. 100% of focused microparticles, over the first 10 second period, were found at a lateral position of about 4 µm in width around the centre of the microcapillary. Approximately the same distribution (4 µm)

was observed for the third 10 seconds. The steady state lateral position along the width is where the opposing horizontal component of force balance. The equilibrium vertical position is where the downward and upward forces component become equal. Since the microelectrodes were applied with equal voltages, this equilibrium position would be at the channel's centreline. However, due to fabrication misalignment, this equilibrium point was observed to be slightly shifted away from the centre of the microchannel. These trends clearly indicated that the steady state position in the microchannel is achieved, which should lead to accurate and fast data analysis in the light scattering experiment compared to those without DEP.

From the above figure, it is clear that random particles are more likely to travel at certain positions. This could be related to how the wetting of the microchannel walls was happened. In our case, it could be the difference in the nature of the exposure to oxygen ions. A planer surface directly exposed to the oxygen ions, while limited oxygen ions enter the microchannel through the open access (inlet reservoir and roofless spiral outlet). Since capillary, the microparticles will follow the well-wet long column, which is hard to film properly. Also, this sample at the end may have lost proper wetting on one of its walls, which is why microparticles travelled through the other one and middle. From the time averaged DEP focusing equation, the force increases linearly with particle volume. Hence, we expected the fabricated microchip to focus bigger microparticles with the same applied AC potential, as it shall be presented in the next section.

4.5.6 Response of 10 μm polystyrene particles

As described in Chapter 2 larger particles expected to experience much stronger DEP force than smaller particles, due to the fact that the DEP force is proportional to the cube of particle radius [22] and hydrodynamic force is proportional to the particle radius [23][24]. Therefore, with the same AC potential, larger microparticles would experience such stronger DEP force to overcome the hydrodynamic drag force and deflected them away from the microchannel's sidewalls. The response of 10 μm polystyrene particles has been investigated in a proof of concept. When the microelectrode pairs operated with 30 V_{p-p} at 10 MHz, video of the fluidic carrying microparticles through the fluidic network was recorded. The observations extracted

from the high speed camera image frames are shown in Figure 4-17. The 10 µm particles had a relatively higher distribution with RCV of 5.13% in comparison with RCV of 4.84% calculated for the 6 µm sample. However, this is might be due to the fact that the 6 µm sample had relatively a higher exposure time to the n-DEP force. The measured 6 µm polystyrene microparticles passed through the 3D microcapillary at a measured (1.13 – 1.89 mm/s) range of velocities in comparison with (1. 48 – 2.76 mm/s) for the 10 µm ones. Therefore, a sufficient focusing of bigger microparticles is achieved with the same applied AC potential.
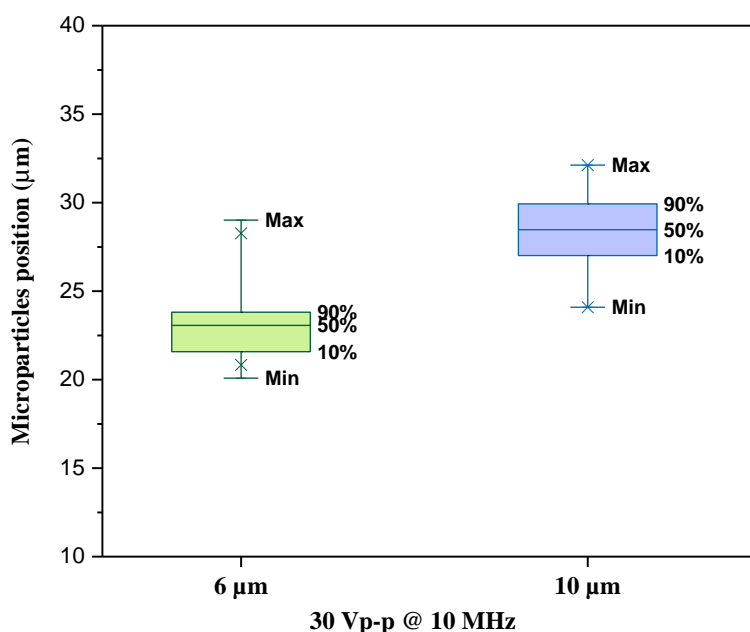
Figure 4-17 Distribution of 6 and 10 µm polystyrene microparticles while operating the microelectrodes with an AC potential of 30 V$_{\text{p-p}}$ at a frequency of 10 MHz. (Green and blue refers to two different samples).

The applied AC voltage and frequency are important parameters in which a sufficient focusing can be achieved, and thus the microchip was tested at different applied voltage and frequency to compare their influence on microparticles physical motion. In the first experiment, the microelectrodes powered by an AC signal of 20 V$_{\text{p-p}}$ and a frequency of 10 MHz. The observations extracted from the high speed camera image frames and with a code written in MATLAB are shown in Figure 4-18. 80% of the detected 89 microparticles sized 10 µm were driven away from the sidewalls of the microchannel and found at a lateral position of 23.55 ± 7.00 µm around the centre of the microchannel. When the frequency of AC potential was increased to 30 MHz with the same (20 V$_{\text{p-p}}$) applied voltage as the previous experiment, the 80% of detected 65 microparticles were travelling at a lateral position of 27.23 ± 5.89 µm. It is clear that

the distribution of microparticles slightly improved; this is while in both experiments, the microparticles flow in the almost same speed within the capillary flow. However, it is an insignificant difference with a 20 MHz increase in the applied AC frequency. Note that the median in the sample (E) is significantly being dragged toward the lower part of the boxplot due to the misalignment in the fabricated microchip (this is the case where the top microelectrodes are not face-to-face with the bottom microelectrodes).
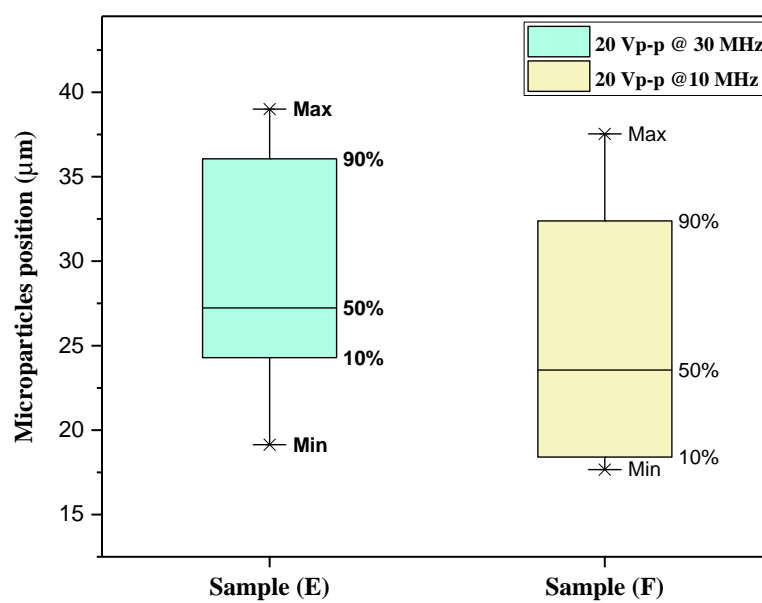
Figure 4-18 Distribution of 10 µm polystyrene microparticles under different applied AC frequency.

To confirm the results and to investigate the influence of a higher field frequency, the next two experiments were carried out while operating microelectrodes with an AC peak-to-peak voltage of 30 V_{p-p} with a frequency of 10 MHz and 30 MHz. The measured horizontal positions of microparticles over a ~ 34 second period, are plotted in Figure 4-19. Microparticles were highly aligned in a single stream within the centre of the microchannel. The result, when an AC potential of 30 $_{Vp-p}$ at 10 MHz was applied across the microelectrodes, indicates that the 80% of detected 248 microparticles passing through the sample (D) were highly aligned at a lateral position of 28.47 ± 1.46 µm around the microchannel's centre. Almost the same distribution (25.76 ± 1.47 µm) was observed when the applied AC frequency was increased to 30 MHz. Note that the 81 detected microparticles under the higher applied electric field were travelling relatively faster (3.50 ± 0.34 mm/s) than the microparticles passed through the sample (D), which had a range of velocities of 2.32 ± 0.20 mm/s (see chapter 5).
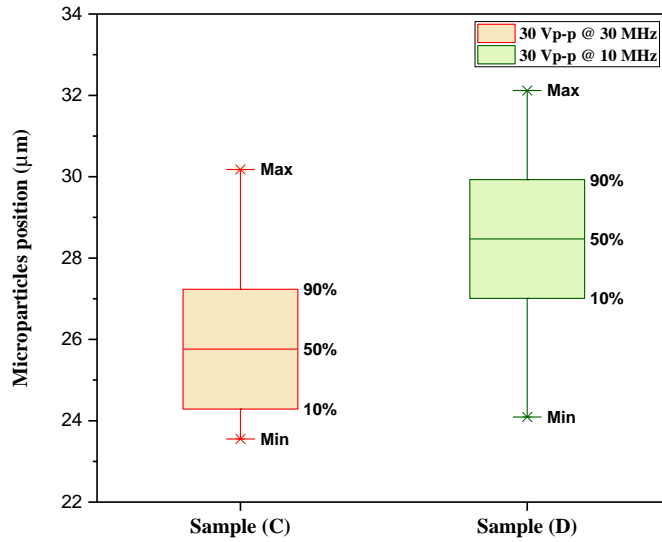
Figure 4-19 Distribution of 10 µm polystyrene microparticles under applied AC frequency.

In the following the strength of the applied AC potential and its potential of providing a steady state position downstream at the sensor position is examined. The result indicates that the microparticles in flow downstream, at least 350 µm away from the narrower edge of the microelectrode focusing section, remain focused after leaving the AC potential (DEP microelectrodes focusing section), as shown in Figure 4-20.
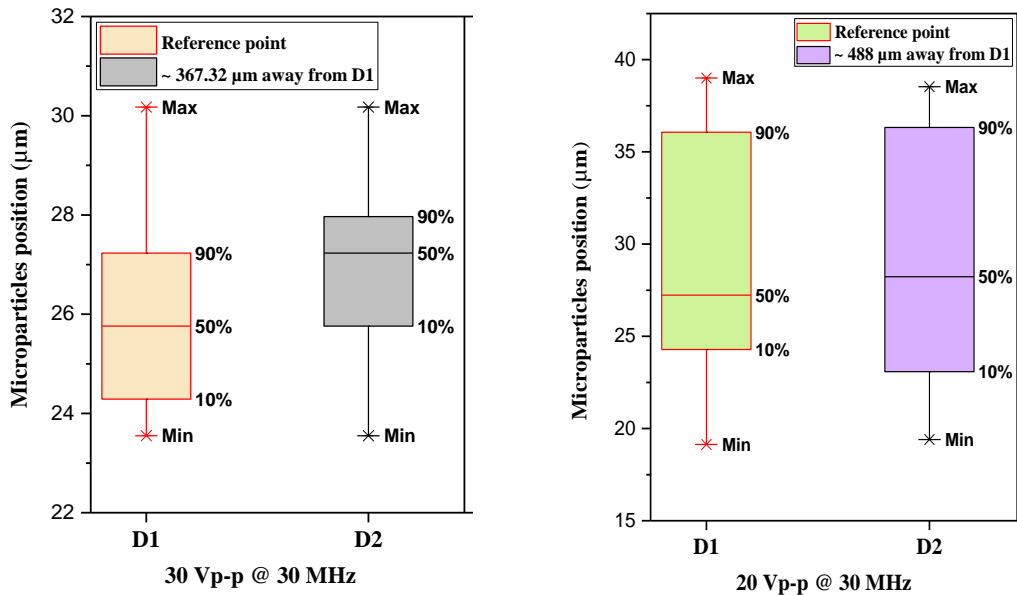
Figure 4-20 The position of the downstream polystyrene microparticles compared to their position at a point close to the narrower edge of the microelectrodes for two different fabricated chips. The applied AC voltage and frequency with the distance from the microelectrodes focusing section given in the caption.

These trends with the calculated RSD and RCV clearly indicate that the applied AC voltage has the greatest effect on the microparticle focusing response, the microparticles in flow downstream and along the available length of the microchannel (through the open viewing window from the high speed camera) remain focused in a single stream as they were under the influence of the n-DEP force, due to laminar flow, we can understand this easily from the table below. In the next section, increasing the magnitude of applied AC potential across the microelectrodes and its influence on 6 µm polystyrene microparticles behaviour is investigated and compared with 10 µm ones used in this section.

Table 4-2 illustrates the measured median, RSD, RCV of propagated particles along the microchannel's length while operating the microelectrodes with selected AC sine wave.

Size	No. of particles	Voltage peak-to-peak (v)	Frequency (MHz)	RSD (µm)	RCV %	Range of velocities (mm/s)
10	89	20	10	5.48	24.19	4.55-2.19
10	65	20	30	5.89	21.61	3.25-1.81
10	248	30	10	1.46	5.13	2.76-1.48
10	81	30	30	1.47	5.70	4.08-3.06
6	131	30	10	1.12	4.84	1.13-1.89
6	206	40	10	2.95	10.82	4.30-3.48
6	53	40	30	0.74	3.44	0.58-0.53

4.5.7   6 µm polystyrene microparticles distribution as a function of applied AC signal.

In this section, an AC potential of 40 V_{p-p} at 10 and 30 MHz was used not only to investigate the effect of a lager applied field on microparticles behaviour but also to compare their horizontal position distribution with 10 µm ones. The results, through observations of frames extracted from the high speed camera, are as shown in Figure 4-21. The 80% of detected 206 microparticles over ~ 33 second period passing, through sample (G), were repelled away from the channel's sidewalls and found in a single stream of 27.23 ± 2.95 µm around the centre of the microchannel. This is almost

the double of the distribution it has been observed for the 10 µm. Note this is while the microparticles were operated with a lower value of applied voltage (20 V_{p-p}), see previous section. When the frequency of the applied AC signal was increased to 30 MHz, all of the detected 53 microparticles sized 6 µm over a ~ 16 second period (due to switching off the AC power and reapplying it with different magnitude) were repelled way from the channel's sidewalls and tightly aligned in a single stream of 21.34 ± 0.75 µm in the centreline of the microchannel, no outliers to be taken into account.
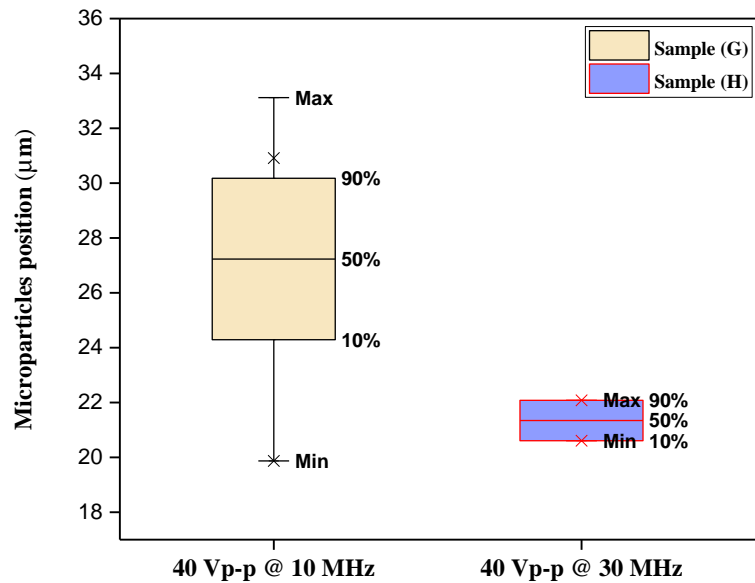
Figure 4-21 Distribution of 6 μm polystyrene microparticles as a function of an applied AC signal given in the caption.

This is a significant difference affected the behaviour of 6 µm polystyrene microparticles and inconsistent with what we have reported in the previous section (insignificant effect on microparticles response while increasing the frequency of the applied AC potential from 10 to 30 MHz with 30 V_{p-p}). This can be due to the fact that these microparticles have relatively a higher exposure time to the DEP force. The measured velocities indicate that the microparticles passing through the sample (H) with a velocity of (0.55 ± 0.025 mm/s) compare with (4.06 ± 0.41 mm/s) for those passing through the sample (G). Therefore, the significant improvement in focusing efficiency is achieved. We have shown that the flow rate is an important parameter affected the focusing efficiency, the smaller the flow rate is the sufficient n-DEP force is to move all the microparticles within a flowing fluid stream in an equilibrium

position inside the microchannel, which is required condition to perform detection and sorting of microparticles or cells according to their size and / or shape for in functional microfluidic platform. For applications with capillary system, the DEP platform will have the potential of reducing variation in the intensity of the detected signal and therefore providing fast and efficient microparticles, such as cells, counting and separation chip based flow cytometer.

4.6 Summary

In conclusion, this piece of work demonstrates the ability of the integrated microelectrode focusing section to provide a strong n-DEP force, perpendicular to the laminar flow, to position microparticles, such as cells, within a flowing fluid in a single stream, within the microchannel's centreline, for scattering measurements. The functioning of the device was assessed by detecting and counting 6 µm and 10 µm polystyrene microparticles as an example to assess how biological cells, and mainly white blood cells, might flow within the fabricated 3D capillary driven microchannel based on volumetric similarity. The focusing efficiency of the two active microelectrode systems is assessed and compared. The results demonstrated an effective n-DEP force on microparticles behaviour when a minimum AC potential of 30 volt peak-to-peak and a frequency of 10 MHz was applied across the microelectrodes. We have shown, bigger microparticles can be focused relatively accurate with the applied AC potential, and thus the proposed system can be used for focusing larger microparticles. The microparticles in flow downstream remain focused after leaving the DEP focusing area. Thus n-DEP based capillary driven platform ensures that microparticles passing through the optical detector, move one by one and at a more similar speed. A more precise examination of this latter point will be carried out in the next chapter. This suggests that all microparticles will be subjected to the same illumination intensity for reliable scattering measurements using the fully integrated device with lasers and photo-detectors.

4.7 Bibliography

[1]   D. Juncker, H. Schmid, W. H. Drechsler, and B. Michel, "Microfluidic capillary systems for the autonomous transport of bio/chemicals," *Micro Total Anal. Syst. 2002*, vol. 2, pp. 952–954, 2002.

[2]   N. Ichikawa, K. Hosokawa, and R. Maeda, "Interface motion of capillary-driven flow in rectangular microchannel," *J. Colloid Interface Sci.*, vol. 280, no. 1, pp. 155–164, 2004.

[3]   R. Thomas, A. Harrison, D. Barrow, and P. M. Smowton, "Photonic integration platform with pump free microfluidics," *Opt. Express*, vol. 25, no. 20, p. 23634, 2017.

[4]   Y. Temiz, J. Skorucak, and E. Delamarche, "Capillary-driven microfluidic chips with evaporation-induced flow control and dielectrophoretic microbead trapping," *Microfluid. BioMEMS, Med. Microsystems XII*, vol. 8976, no. February 2014, p. 89760Y, 2014.

[5]   A. Docoslis, N. Kalogerakis, L. A. Behie, and K. V. I. S. Kaler, "A novel dielectrophoresis-based device for the selective retention of viable cells in cell culture media," *Biotechnol. Bioeng.*, vol. 54, no. 3, pp. 239–250, 1997.

[6]   D. Williams and I. Sebastine, "3D focusing of nanoparticles in microfluidic channelss," *IEEE Proc. nanobiotechnology*, vol. 152, no. 6, pp. 207–211, 2005.

[7]   D. Holmes, H. Morgan, and N. G. Green, "High throughput particle analysis: Combining dielectrophoretic particle focussing with confocal optical detection," *Biosens. Bioelectron.*, vol. 21, no. 8, pp. 1621–1630, 2006.

[8]   A. Alazzam, B. Mathew, and F. Alhammadi, "Novel microfluidic device for the continuous separation of cancer cells using dielectrophoresis," *J. Sep. Sci.*, vol. 40, no. 5, pp. 1193–1200, 2017.

[9]   H. R. Nejad, O. Z. Chowdhury, M. D. Buat, and M. Hoorfar, "Characterization of the geometry of negative dielectrophoresis traps for particle immobilization in digital microfluidic platforms," *Lab Chip*, vol. 13, no. 9, pp. 1823–1830,

2013.

[10] M. Mohammadi, H. Madadi, J. Casals-Terré, and J. Sellarès, "Hydrodynamic and direct-current insulator-based dielectrophoresis (H-DC-iDEP) microfluidic blood plasma separation," *Anal. Bioanal. Chem.*, vol. 407, no. 16, pp. 4733–4744, 2015.

[11] Barbara J. Bain, "Blood Cells A Practical Guide," *Wiley Blackwell*, no. 5th ed, p. 504, 2015.

[12] A. Castellanos, A. Ramos, and A. Gonz, "Electrohydrodynamics and dielectrophoresis in microsystems scaling laws   Antonio Ramos - Academia," 2003.

[13] N. G. Green and H. Morgan, "Dielectrophoretic separation of nano-particles," *J. Phys. D. Appl. Phys.*, vol. 30, pp. L41–L44, 1997.

[14] F. E. H. Tay, L. Yu, and C. Iliescu, "Particle manipulation by miniaturised dielectrophoretic devices," *Def. Sci. J.*, vol. 59, no. 6, pp. 595–604, 2009.

[15] K. Khoshmanesh *et al.*, "Dielectrophoretic manipulation and separation of microparticles using curved microelectrodes," *Electrophoresis*, vol. 30, no. 21, pp. 3707–3717, 2009.

[16] P. R. C. Gascoyne and S. Shim, "Isolation of circulating tumor cells by dielectrophoresis," *Cancers (Basel).*, vol. 6, no. 1, pp. 545–579, 2014.

[17] K. Khoshmanesh *et al.*, "Size based separation of microparticles using a dielectrophoretic activated system," *J. Appl. Phys.*, vol. 108, no. 3, 2010.

[18] W. M. Arnold, H. P. Schwan, and U. Zimmermann, "Surface conductance and other properties of latex particles measured by electrorotation," *J. Phys. Chem.*, vol. 91, no. 19, pp. 5093–5098, 1987.

[19] A. Sobiesierski, R. Thomas, P. Buckle, D. Barrow, and P. M. Smowton, "A two-stage surface treatment for the long-term stability of hydrophilic SU-8," *Surf. Interface Anal.*, vol. 47, no. 13, pp. 1174–1179, 2015.

[20] L. D. LANDAU and E. M. LIFSHITZ, *FLUID MECHANICS.pdf*, Second Eng. Oxford, New York, Beijing, Frankfurt,Sao Paulo, Sydney, Tokyo, Toronto, 198AD.

[21] C. C. Chen, P. H. Lin, and C. K. Chung, "Microfluidic chip for plasma separation from undiluted human whole blood samples using low voltage contactless dielectrophoresis and capillary force," *Lab Chip*, vol. 14, no. 12, pp. 1996–2001, 2014.

[22] A. Olanrewaju, M. Beaugrand, M. Yafia, and D. Juncker, "Capillary microfluidics in microchannels: From microfluidic networks to capillaric circuits," *Lab Chip*, vol. 18, no. 16, pp. 2323–2347, 2018.

[23] A. Aliano *et al.*, *AC Electrokinetics: colloids and nanoparticles*. 2003.

[24] M. Dürr, J. Kentsch, T. Müller, T. Schnelle, and M. Stelzle, "Microdevices for manipulation and accumulation of micro- and nanoparticles by dielectrophoresis," pp. 722–731, 2003.

Chapter 5

MICROPARTICLES VELOCITY UNDER THE NEGATIVE DIELECTROPHORETIC FORCE

5.1 Introduction

Particle size measurements and sorting require a regular flow of single microparticles or cells within a single stream, as in flow cytometry and fluorescence-activated cell sorter (FACS) [1]–[4]. Following the microparticles position analysis discussed in the previous chapter, this chapter focuses on microparticles velocity analysis within the microchannel. Experiments and analysis were carried out here to investigate microparticles velocity under the capillary flow rate with and without the influence of negative dielectrophoretic force (n-DEP). This is an indirect way to prove that the developed device aligned microparticles in a single stream and at an equilibrium height around the centre of the microchannel due to their measured narrower velocity distribution compared to those without DEP effect on them. In this chapter, we measured the velocity distribution with two different configurations of the applied AC field (side-to-side and cross (X)-pattern). Varying the strength of the applied electric field and its influence on the microparticle velocity distribution is also presented. The separation distance between focused microparticles and the implication for interrogation of close particles is also discussed.

The motion of microparticles with a uniform velocity, as a result of position control under the effect of n-DEP forces created by non-uniform AC electric field, was achieved. Thus, the same signal shape from the same size microparticles passing through a final fully integrated device with lasers and photo-detectors is expected, the case study to be investigated in the next chapter.

5.2   Microparticle peak velocity under capillary flow

Experiments were carried out with 10 µm polystyrene particles, as a test sample, to visualise the fluid profile and to investigate microparticles velocity under an n-DEP force. Microparticles suspended in DI water, at a concentration of $2 \times 10^{\wedge 7}$ beads/mL were injected into the microchannel inlet using a micropipette. Fluid transport was achieved through capillarity action, achievable on the hydrophobic platform via the oxygen plasma surface treatment [5], as reported in Chapter 3. The time at which the sample is placed at the inlet is defined as t = 0, and following this a video is recorded using the high speed camera. It is important to note that t = 0 is the time equal zero only in this experiment, otherwise and throughout the remainder of this work t = 0 is approximately 30 seconds after the drop is pipetted. To allow for easier data analysis, as described in Chapter 3, a typical frame rate of 200 FPS is used to visualise the fluid flow meniscus location. Its location $X_{(t)}$ at a single time (t) is obtained and shown in Figure 5-1. However, we were unable to measure its velocity.
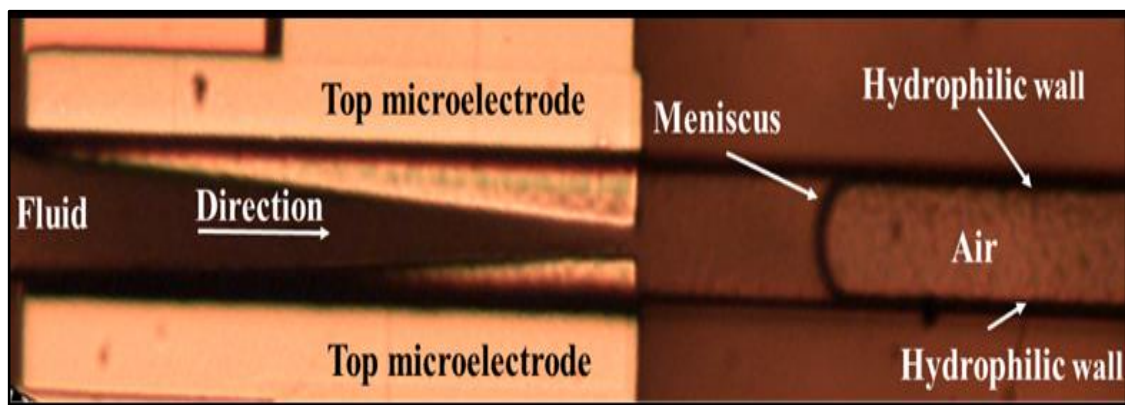
Figure 5-1 Photograph shows an example of the meniscus at the interface for SU-8 microchannel with a rectangular cross section.

The initial acceleration due to capillary action is too fast after sample injection [6][7][8][9] and therefore the velocity of the microparticles would be too fast to allow for successful particle tracking within the available resolution of the high speed camera. Thus, a high speed camera able to record a higher rate of frames per second with a high spatial resolution might be required in order to enable the provision of any useful information about fluid motion. However, a rapid decrease in microparticles velocity was observed after the next short period of time, as the mass of fluid being pulled, by the capillary force at the fluid front, increases. Measured particle velocities in this later regime can be used as an indirect way to predict fluid velocity and has been implemented here to observe the effect of applied n-DEP force. With an AC peak-to-peak voltage of 30 V and frequency of 30 MHz applied across the microelectrodes, the n-DEP response on microparticles physical motion was observed.

Two dimensional particle tracking measurements were carried out using two different methods; i) using the "object tracking tool" from the camera software for tracking the position of single particle through the video frames in the AVI player and ii) a MATLAB R2018a code which is written and developed for carrying out the image tracking and all calculations. Methods described in details in chapter 4. Measurements were taken, at around 16.5 seconds and over the next short period of experimental duration, where we could argue that it was the point of time when the most of the microparticles were flowing under the n-DEP response through extracted frames from the high speed camera. Particle velocities up to 5 mm/s were measured. Previously, particle focusing in a pumped system has been demonstrated by D. Holmes et al [10]. Their work with a system with different dimensions (40 µm high and 250 µm wide), shows that 100% of the used latex particles suspended in Potassium Chloride (KCL) can be focused around the centre of the channel at a flow rate up to a maximum particle velocity of 5 mm/s. This work has been done while operating microelectrodes with an AC signal of 20 V peak-to-peak and frequency of 10 MHz. Morgan et. al. [11] using a channel with dimensions 110 µm ×10 µm and 5mm long, focused microparticles with a peak velocity at a maximum fluid flow of 2 mm/s. The microelectrodes were operated with an AC signal in range 1 to 30 V peak-to-peak and frequency of 18 to 20 MHz. This initial experiment using a capillary driven system demonstrates that n-DEP can be used to focus polystyrene microparticles in a similar way to that in pump-driven systems and suggests the order of fluid velocity in which an n-DEP response can be

observed. In the next section, we will examine how different dielectrophoretic force field configurations, that generate net forces, results in particles moving within a uniform velocity inside the designed microchannel.

5.3   Microparticles velocity

5.3.1   Under n-DEP focusing force along the X- direction of the microchannel

In this section, the experiment is carried out while operating the microelectrodes with an AC signal of 20 V peak-to-peak and frequency of 10 MHz applied to the top microelectrodes with respect to the bottom microelectrodes, which are grounded (0) as shown in Figure 5-2 (A). We now investigate microparticles velocity to see how this might affect on the operation of our intended device, as shown in Figure 5-2 (B).

(A)   (B)
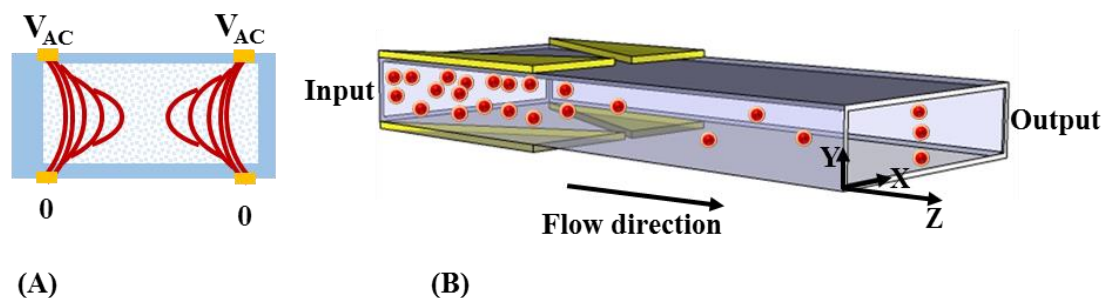
Figure 5-2 **(A) Schema indicates the pattern of applied AC signal, with the region of minimum electric field confined away from microchannel's side walls and (B) the expected variation in microparticles position within the depth of the microchannel. Features are not drawn to scale.**

The velocity of polystyrene microparticles was calculated from frames extracted from the high speed camera and analysed with a code written in MATLAB. The resulting data is plotted in Figure 5-3. A range of velocities is obtained (0.48 - 1.75 mm/s), 80 % of the calculated velocities are close to 0.6 mm/s and a few of them are above 1.3 mm/s. While the recorded position of the 6 µm polystyrene particles was all within the centre of the microchannel (20.61± 1.84 µm) as shown in Figure 5-4. Note that, the statistics are computed in terms of median instead of mean, for the reasons mentioned in chapter 4.
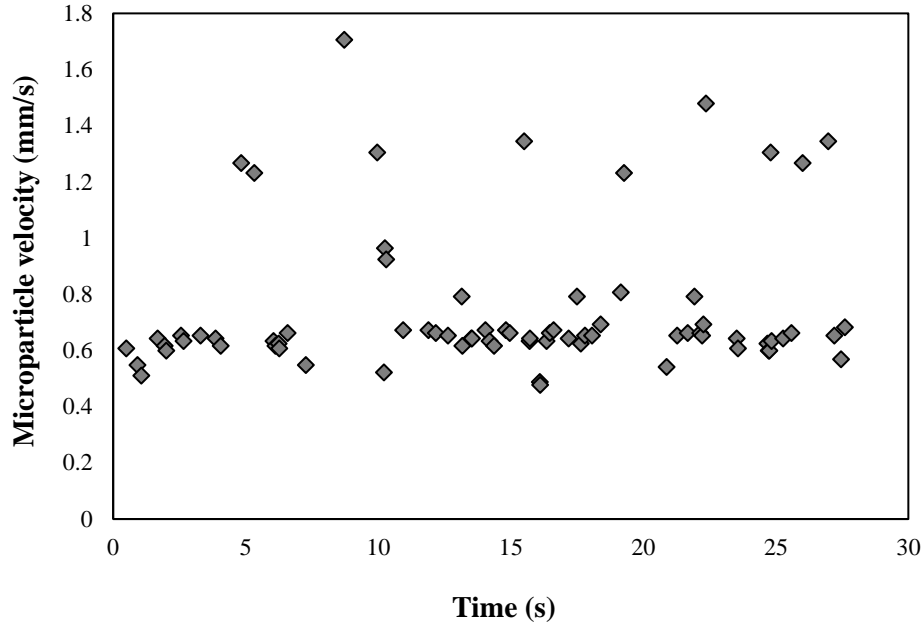
Figure 5-3 6 μm polystyrene microparticles velocity distribution over the experimental duration of about 30 seconds as a function of the applied electric field. The top microelectrodes are powered with 20 V p-p at 10 MHz. while the bottom microelectrodes are grounded. The pattern of the applied electric field is believed to align microparticles around the centre of the microchannel (side-to-side) away from the microchannel's sidewalls.
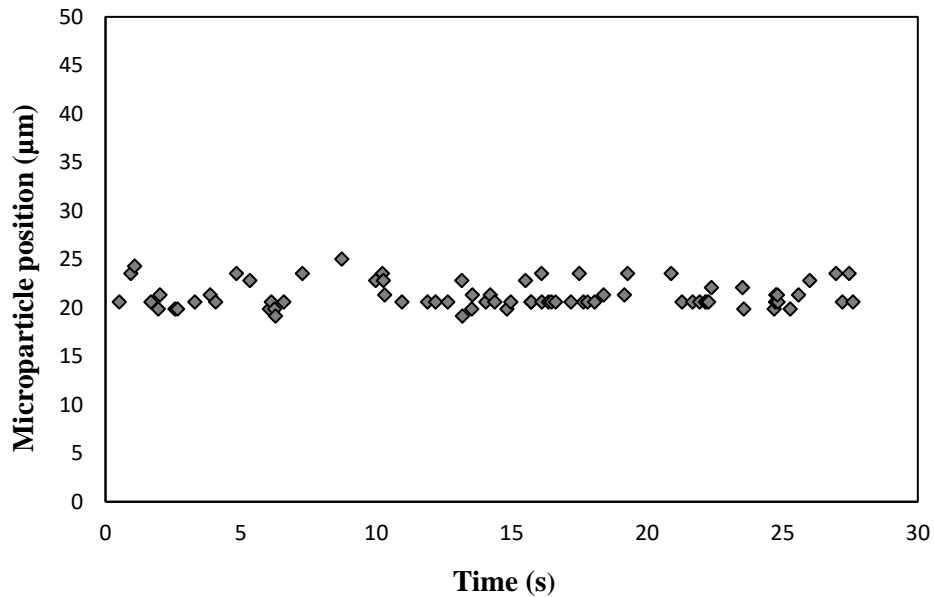
Figure 5-4 Distribution of 6 μm polystyrene particles over the experimental duration of ~ 30 seconds. An AC potential of 20 V p-p at a frequency of 10 MHz applied to the top microelectrodes while bottom microelectrodes are grounded.

In such capillary systems (50 µm × 27 µm), where several microparticles can fit into the depth of the microchannel, microparticles can travel at different heights (velocities). This would make for a complex data analysis of the scattering measurements in a fully integrated device with lasers and photo-detectors. The geometry of microelectrodes and pattern of the applied electric field is believed to confine the microparticle at the minimum electric field intensity region, which is at the centre of the microchannel, away from the edge of the metallic microelectrodes. In the vertical direction, there is no net force on the microparticles, and they are left freely distributed within the depth of the microchannel, as shown in Figure 5-2 (B). From Figure 5-3, we can argue that the microparticles travelling close to the wall of the microchannel were going slower than some that were around the middle of the channel. While the microparticles are being pushed away from the microchannel side walls, the measured velocities suggest that most of the microparticles are not being lifted up from the bottom of the channel. A uniform flow of single microparticles is required to count and manipulate them; therefore, in the following section microparticles velocity distribution is investigated while operating microelectrodes with a cross (X) – electric pattern field polarity.

5.3.2   Under n-DEP focusing force along the XY- plane of the microchannel

A capillary system benefits from the simplicity and ease of use free from external pumps. However, the fluid motion is less controlled than in an externally pumped system. To mitigate the complicated external flow controls here we use three-dimensional focusing by applying the microelectrodes with an X - pattern electric field polarity. This pattern confines the minimum electric field region to the centre of the microchannel. Therefore, based on the applied potential as well the fact that the used microparticles are more polarizable than the fluid medium, chapter 2, the microparticles will feel a net force driving them away from the microelectrode edges. This force will align them in a single stream around the centre of the microchannel, the result of which we have seen in chapter 4, and therefore a regular flow of single microparticles is expected.

In this section, the velocity is measured as a function of time, this is while operating microelectrodes with a sinusoidal signal of 30 V peak-to-peak and 10 MHz. The microelectrodes at the top and bottom surfaces of the microchannel are connected with X – pattern polarity, as shown in Figure 5-5 (A). Therefore, because the maximum electric field strength regions are located at the microelectrodes edges, the generated force would push the microparticles away from the surfaces of the microchannel into the centre of the microchannel (along the Y-axis as well as the X-axis) as illustrated in Figure 5-5 (B).

(A)   **(B)**
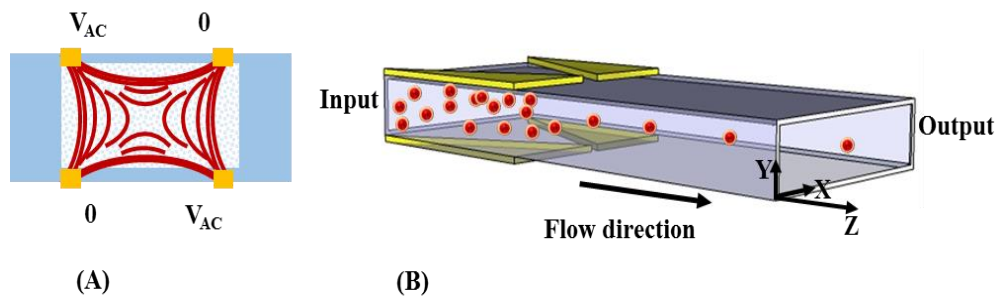
Figure 5-5 (A) Schema shows the pattern of applied AC signal indicating that the region of low electric field at the centre of the microchannel and (B) the expected microparticles distribution under the influence of n-DEP force with fixed vertical and lateral position.

The measured velocities of microparticles over a ~35 second period, again in image frames extracted from the high speed camera and with a code written in MATLAB, are plotted in Figure 5-6.
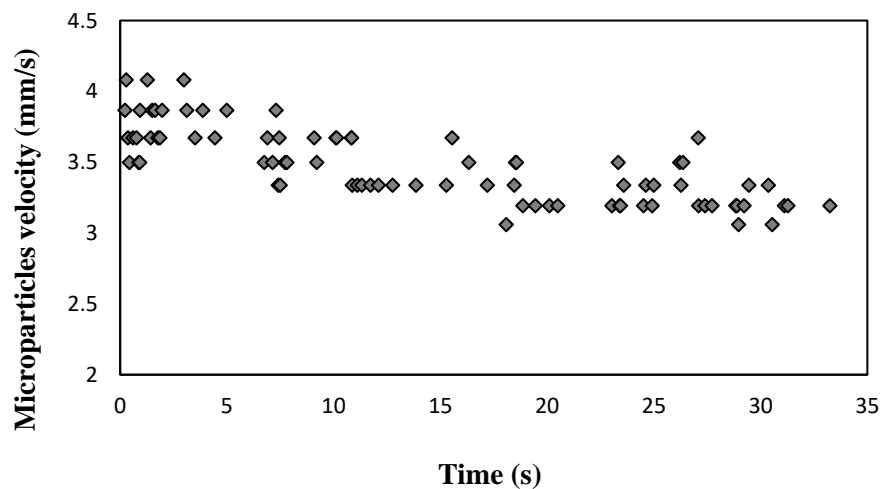
Figure 5-6 10 μm particles velocity distribution over the experimental duration of 35 seconds. This is while operating microelectrodes with an AC signal of 30 Vp-p at 10 MHz.

The results indicate that the applied force has reduced the range of velocity measured. Thereby, the focused 10 µm polystyrene particles passed at a nearly uniform velocity ranges between (~3.00 mm/s and 4.00 mm/s). Note that, this included the gradual reduction in the value of calculated velocities with time. A comparison of the two results in Figure 5-3 and Figure 5-6, suggests that the applied polarity across microelectrode, the X-pattern electric field polarity, has removed the difference in height of microparticles within the microchannel and thereby reduced the differences in microparticles velocity. Together these velocity measurements give an initial indication that the X-pattern voltage application successfully focused the microparticles within one flow stream. By comparing with the previous section, it can be seen that there is a massive variation in the experimentally measured velocities, this is due to the hydrophilic nature of the plasma treated SU-8 microchannel surfaces. We believe the proposed microelectrode focusing design is suitable for integrated capillary flow microfluidic devices. The next section looks closely at the speed of the microparticles travelling under the capillary action in the chip.

5.4   Microparticles velocity distribution in capillary system

5.4.1   Under an n-DEP force

In order to assess the particles velocity distribution under the n-DEP focusing force, repeated experiments were used. Velocity was measured as a function of applied AC potential. The microparticles are expected to travel at a uniform velocity as a result of the focusing effect which was achieved in the earlier experiments and as reported in [4], [12]. We note that the time zero ($t = 0$) will be defined as 30 seconds after the sample is injected into the inlet reservoir. This avoids the initial high and rapidly changing velocities where control is difficult, as described in chapter 4.

In the first experiment, an AC peak – to – peak voltage of 30 V, at a frequency of 10 MHz was applied across the microelectrodes. Through observations of frames from the high speed camera, the influence of n-DEP force on the microparticles velocity was observed. The measured velocities of microparticles over the experiment duration, and with our MATLAB code, are plotted in Figure 5-7. The box plot indicates that the majority of the focused microparticles are moving in a uniform velocity believed to be

the fluid velocity at that time. The 10 µm polystyrene particles passed at a range of velocities (2.91 – 3.62 mm/s), 80% of the calculated velocities are between 3.11 mm/s and 3.43 mm/s. Thus, we assumed that these microparticles experienced a negative dielectrophoretic force driving them away from the microchannel walls to an equilibrium height within the microchannel's depth.
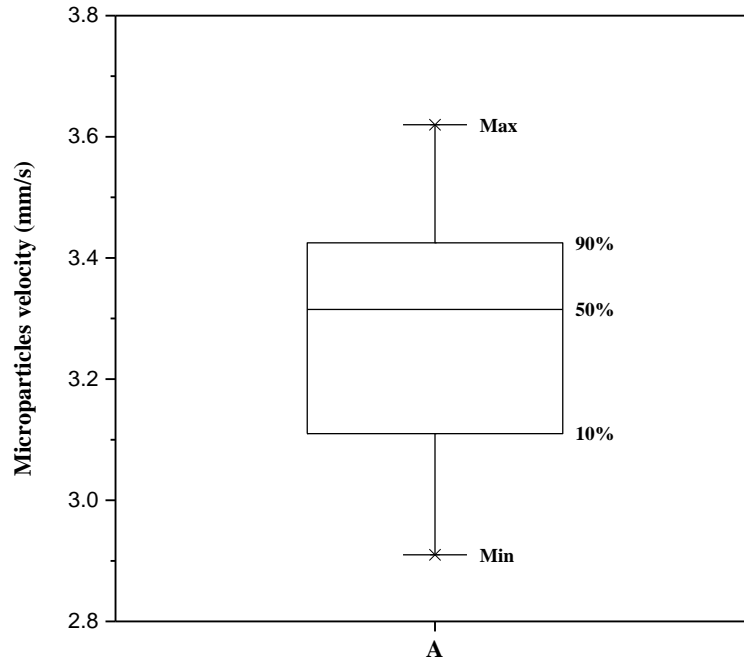
Figure 5-7 10 µm particle velocities measured under the n-DEP effect over an experiment duration of 30 seconds.

Our experiment shows that the focused microparticles will flow through our device with a steady velocity. This would reduce the false-sort events in our intended device with lasers and photo-detectors for scattering measurements. In the following, further experimental and statistical tests revealed similar behaviour, as shown in Figure 5-8.

Figure 5-8 provides the results obtained from the measured velocities of 10 µm diameter polystyrene particles for the fabricated samples A and B. This was under the non-uniform electric field generated by applying an AC potential across the microelectrodes and by using our in-built software. It can be seen that 80% of the calculated velocity of 81 microparticles symbolised by the blue box is between about 3.20 mm/s and 3.90 mm/s, over 30 seconds. This revealed that the microparticles under the influence of n-DEP were highly aligned in a single stream around the midpoint of the microchannel.
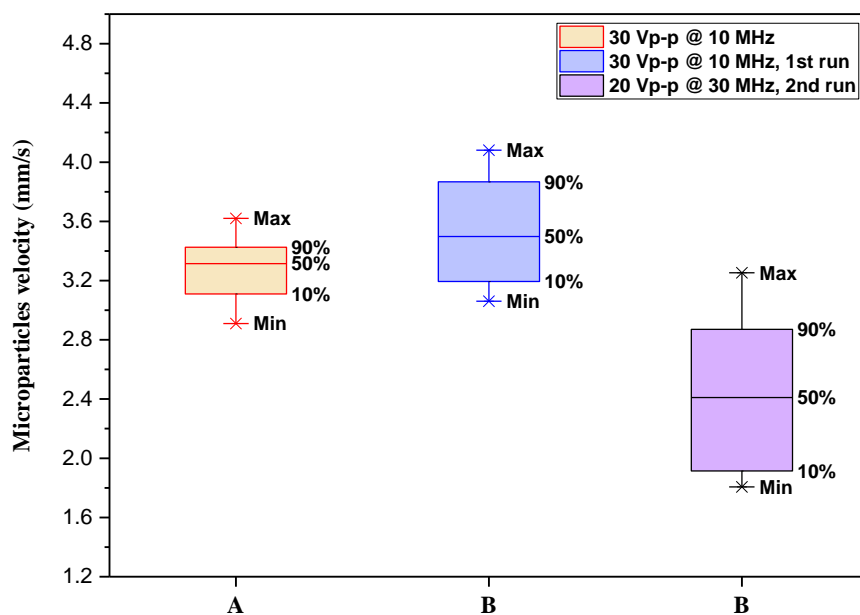
Figure 5-8 10 μm polystyrene particles velocities while operating the microelectrodes with an X-pattern AC potential.

This was also in accordance with our earlier observations, replotted in the same figure for comparison (red chart box). It is clear that 80% of the focused microparticles were moving at a speed range from 3.11 mm/s to 3.43 mm/s in the flowing fluid. It should be noted that the same size and approximately the same volume of microparticle were used with the same applied AC potential, but with a different fabricated microchip. Therefore, a wider range of the calculated velocities can be due to the imperfections of the fabricated chip, where the top and bottom set of microelectrodes were slightly offset from the centre of the microchannel or from each other, results in a microparticle concentration that is not centred in the microchannel. Additional, it can be seen that the overall calculated velocity while using sample B is higher than that of sample A, this behaviour might be due to some differences in hydrophobic recovery of treated SU-8 samples. The hydrophilicity of SU-8 samples that have achieved via the applied plasma.

The third experiment (second run) was carried out, first by having the tested chip (sample B) rinsed with deionised (DI) water (instead of replacing sample B, we just clean it with DI water) before leaving it to dry in room temperature for several minutes, and then the microdevice powered by an AC signal of 20 V peak – to – peak with a frequency of 30 MHz. Again, the n-DEP response on 10 μm polystyrene particles was

observed through extracted frames from the high speed camera. Figure 5-8 shows the statistics of the measured velocities of 65 microparticles, which were collected over 30 seconds recorded video and with our MATLAB code. The data shows that there is a clear reduction in the average velocity of microparticle during the second use of the microchip, approximately 1mm/s less than that of the first run. This might be due to the gradual decrease in the hydrophilic nature of the plasma treated SU-8 surfaces. The next section covers the velocity distribution whilst toggling the applied electric field.

5.4.2   While toggling applied AC signal

To assess the performance of our fabricated DEP capillary driven microfluidic chip for particle focusing, experiments were carried out with 6 µm polystyrene particles to investigate their velocity whilst toggling the applied sinusoidal signal. The microelectrodes were applied with an X – pattern of applied AC power source, with it toggled every 10 seconds over the total duration of the experiment (approximately 34 seconds (see chapter 4 section 4.3)). The measured horizontal velocities, using observations of the differences between frames from the high speed camera, are plotted in Figure 5-9.
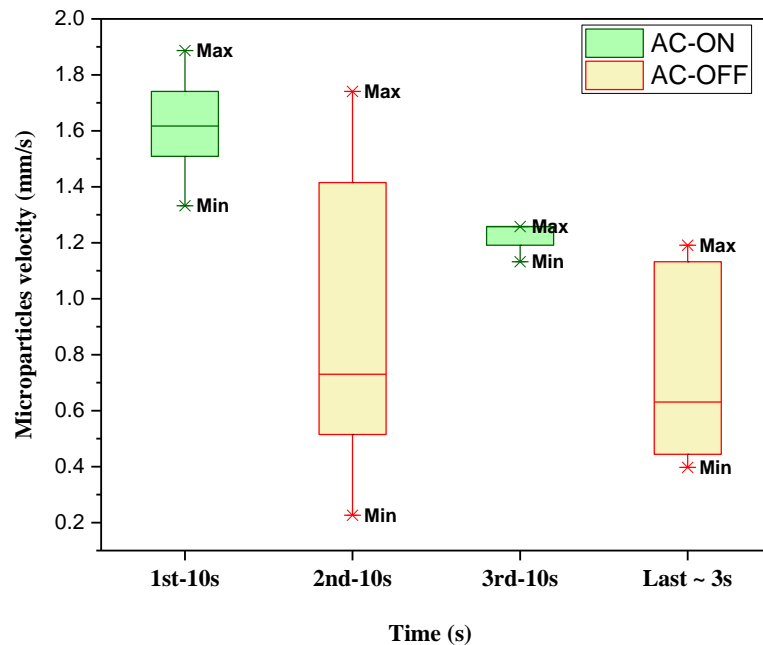
Figure 5-9 Velocity distribution based on the lateral displacement of 6 µm polystyrene particles while toggling the applied AC potential using 30 V $_{p-p}$ at 10 MHz. This is over experiment duration of ~ 34 seconds.

When operating the microelectrodes with an AC peak – to – peak voltage of 30 V with a frequency of 10 MHz, the microparticles started to move in a uniform velocity. This indicated that the microparticles experienced negative dielectrophoretic force in both X-axis and Y-axis and hence are arranged in a single stream around the centre of the microchannel. The microparticles were released from the DEP force after switching off the applied non-uniform electric field and a range of velocities is obtained (0.23 mm/s -1.75 mm/s) between ~12 and 21 seconds, as shown in Figure 5-9. This variation suggests that these microparticles were at different streamlines within the fluid flow. When re-applying the AC signal, again the microparticles were repelled away from the surfaces of the microchannel and aligned around the centre of the microchannel and with a narrower velocity distribution. This shows the fast response of our proposed microfluidic chip for moving from one state to another and for driving the microparticles toward the centre of the microchannel with a uniform velocity. The plot indicates that the microparticle and fluid velocity is decreasing from 1.62 ± 0.12 mm/s to 1.26 ± 0.04 mm/s with time over the recorded experiment duration, assuming in both cases particles are focussed to the same central position. It can be seen that such speed difference, due to the nature of the capillary flow, is not as significant as the variation in speed caused by unfocused particle. Hence, in our intended device with lasers and photo-detectors, the spread of the measured intensity distribution of focused particles is expected to improve significantly compared to those without DEP effect on them.

In this work, fluid penetrated the microchannel by capillary action. Thereby, microparticles nearby the channel's walls were expected to travel faster than those around the centre [13][14]. However, replotting the data of Figure 5-9 in Figure 5-10 shows that the focused microparticles, represented by red and yellow crosses, were driven into the region where the velocity was the highest. This suggests that the fluid velocity is highest at the centre of the channel. Such a result can be explained by considering the balance of forces in the system as described in Chapter 2 and that the capillary force is only present at the fluid front so that behind the advancing meniscus the fluid flow becomes faster at the centre due to the greater friction at the side walls [8][7].
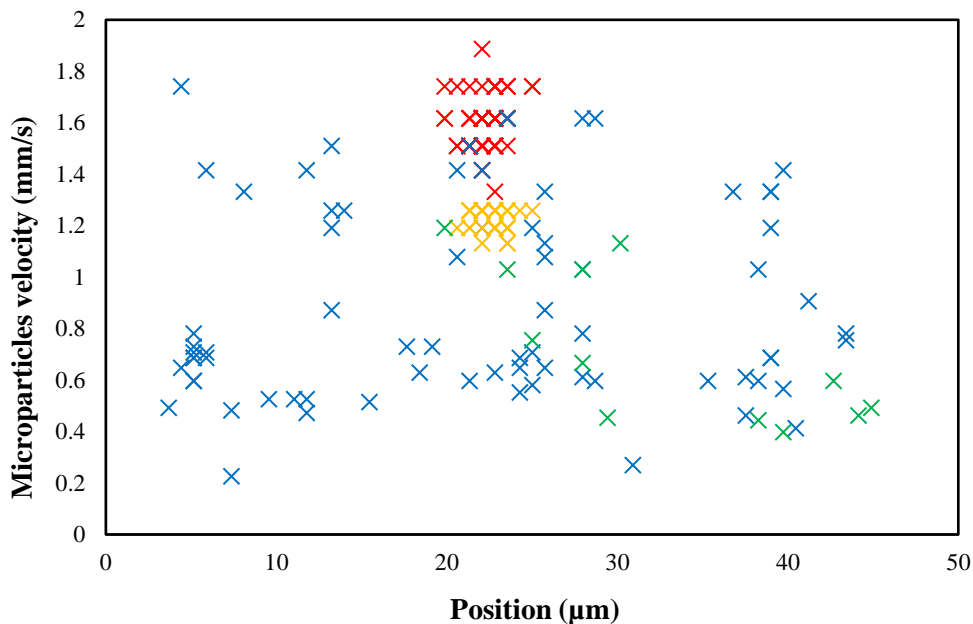
Figure 5-10 6 μm particle velocities distribution as a function of toggling applied AC potential.

Figure 5-10 also shows that the most of the unfocused microparticles have the slowest velocity as they were at the bottom of the microchannel. It can be seen that some of the unfocused microparticles were travelling with almost the same velocity as those that were focused. I would say that (along horizontal plane) those microparticles were around the centre of the microchannel and hence travelled in the almost same velocities as those of focused ones. The calculated velocities of (~1.2 mm/s -0.4 mm/s) over the last less than 4 seconds of the experiment, indicates that the 13 microparticles represented by the green crosses still travel with a wider range of velocities in the absence of DEP focusing force. Therefore, in such a capillary system, and over about 30 second period, in the absence of the n-DEP force, there is a massive variation in the velocity between the slowest and the fastest microparticle. This would increase variation in detected signal intensity from the same sized microparticles such as cells, which would make for complex data analysis in our intended device with lasers and photo-detectors for scattering measurements. Furthermore, the reduction in measured velocity over the experiment period, due to reduction in a fluid flow over time in the capillary driven system, led to an improvement in microparticle focusing response [12] in a way that reduced the difference in their velocities. To investigate the usage and strength of the applied n-DEP focusing force and its potential on the application with capillary driven system more quantitatively, it is important to measure microparticles

velocity in detail relative to their position in flow through different regions along the length of the microchannel, and this is presented in the next section.

5.4.3   Before, between and after the microelectrodes structure.

While this work and previous work [4], [10]–[12], [15]–[19] has shown that particles can be focussed at the position of the electrodes, the fully integrated device we will develop requires the particles to remain focussed downstream at the sensor position. In this section, I evaluate the position downstream and compare it with the position at various points along the length of the channel. The experiment used 6 µm polystyrene particles, with the applied potential switched on. Here, the microelectrodes were operated with the X-pattern of the applied AC source. The selected regions were; i) before microelectrodes focusing section, ii) between microelectrodes focusing area and iii) after microelectrodes focusing section. The video recording was taken with 200 frames per second (FPS), and the computed positions using the code written in MATLAB, are plotted in Figure 5-11.
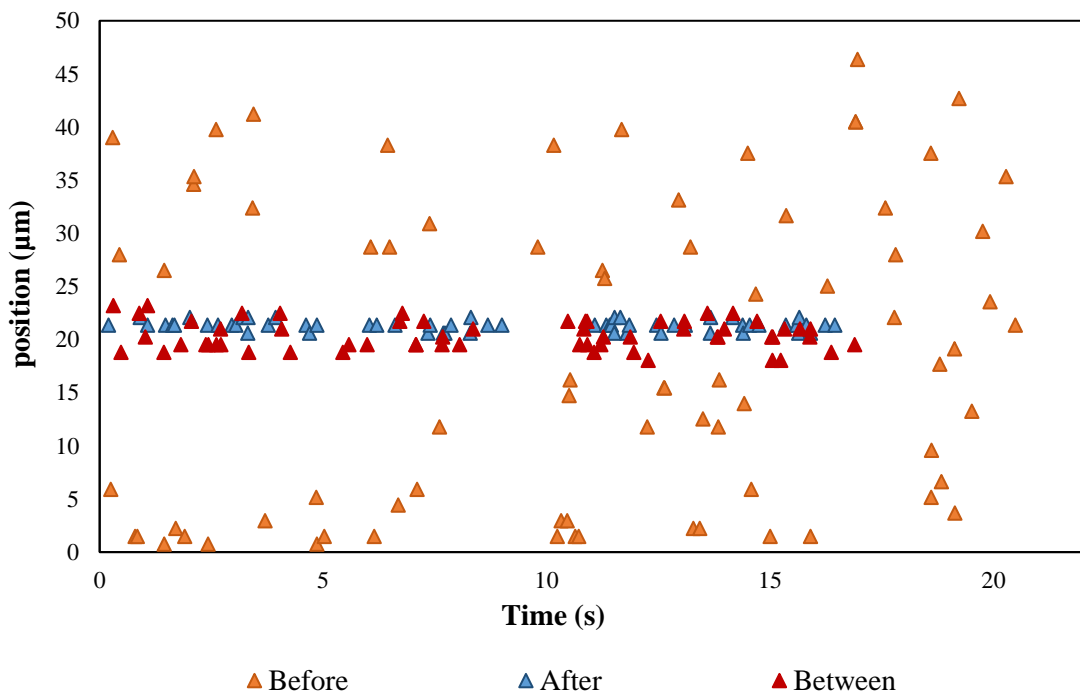
Figure 5-11 Position distribution of 6µm polystyrene particles at three different regions along the channel's length. This is a long horizontal plane.

Figure 5-11 shows microparticles measured before the microelectrodes, symbolised by orange triangles, distributed over the full width of the microchannel. These microparticles were measured at the main entrance of the three dimensional microchannel (50 µm × 27 µm) and before microelectrodes focusing structure. In this part of the structure, the microparticles were outside the influence of negative dielectrophoretic force and are flowing under capillary action only. On passing through the microelectrodes focusing structure, microparticles, symbolised by red triangles, are pushed away from the sidewalls of the channel and localised in what we believe is the minimum-electric field located between the microelectrodes. After the microelectrodes region, microparticles, symbolised by blue triangles, were focused in a single stream around the centre of the microchannel (21.30 ± 0.5 µm), (non-zero, 25 µm, due to fabrication misalignment). After the microelectrode region, the n-DEP force should fall rapidly to zero. However, the microparticles remain in the same streamline downstream due to laminar flow, as shown in Figure 5-12.
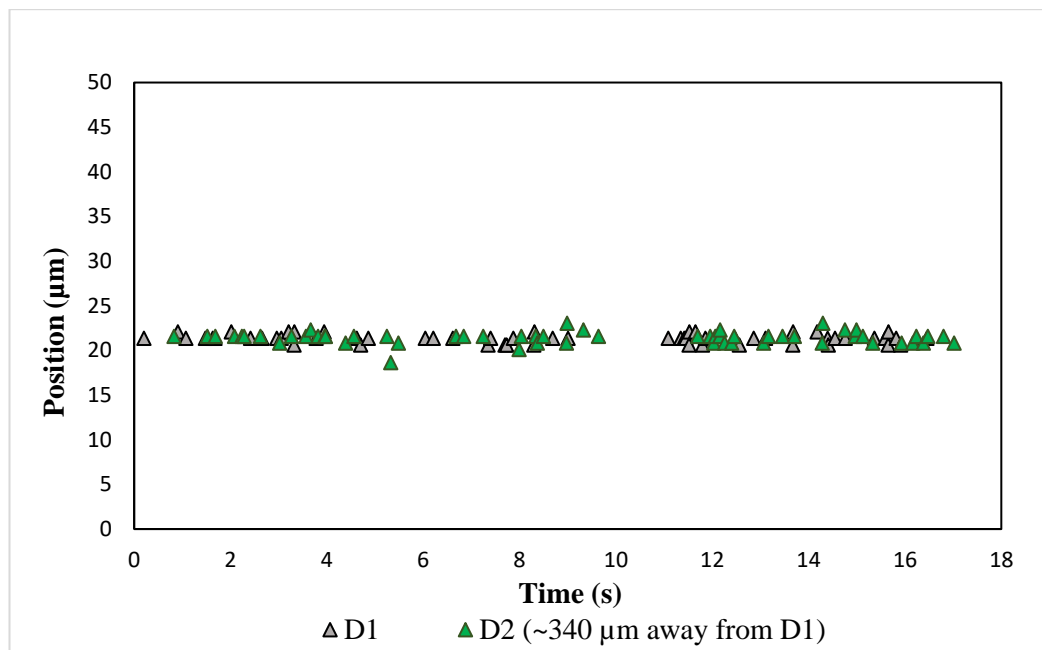
Figure 5-12 position distribution of 6 µm polystyrene particles through two different windows (D1 and D2) along the channel's length. Distance between D1 and D2 is about 340 µm.

In this particular example, the distance downstream from the microelectrode region is about 500 µm, due to the limitation in data collection of the high speed camera. Note the 3D microchannel used in this work is 1410 µm long. Under the n-DEP focusing force, the measured position of, 21.30 ± 0.50 µm immediately after and 21.40 ± 0.70

µm further downstream of the microelectrode focusing section, through the first and the second window (D1 and D2), respectively, indicated that focused microparticles remain within the same focusing position downstream where the lasers and photo-detectors will be in our final fully integrated chip.

Further analysis was carried out to assess the microparticles velocity along the three regions, before, within and after the microelectrodes. The measured velocities as a function of the experiment period are plotted in Figure 5-13 where the colour of the triangles corresponds to the colours in Figure 5-11. It can be seen that there is a massive difference in the value of calculated velocities for microparticle before and after the influence of the n-DEP force. Before the microelectrode focusing section, without any influence of the n-DEP effect, a range of velocities is obtained (0.5 mm/s -0.075 mm/s). Most of the calculated velocities are less than 0.3 mm/s and just a few of them are close to 0.5 mm/s. The velocities measured for particles between the microelectrodes are on average faster and equal to the fastest of the particles measured before the microelectrodes. This suggests after focussing the particles are at the fastest flowing part of the channel. Note that, for randomly distributed microparticles, velocities computed using the tools in AVI camera video for the reason given in chapter 4.
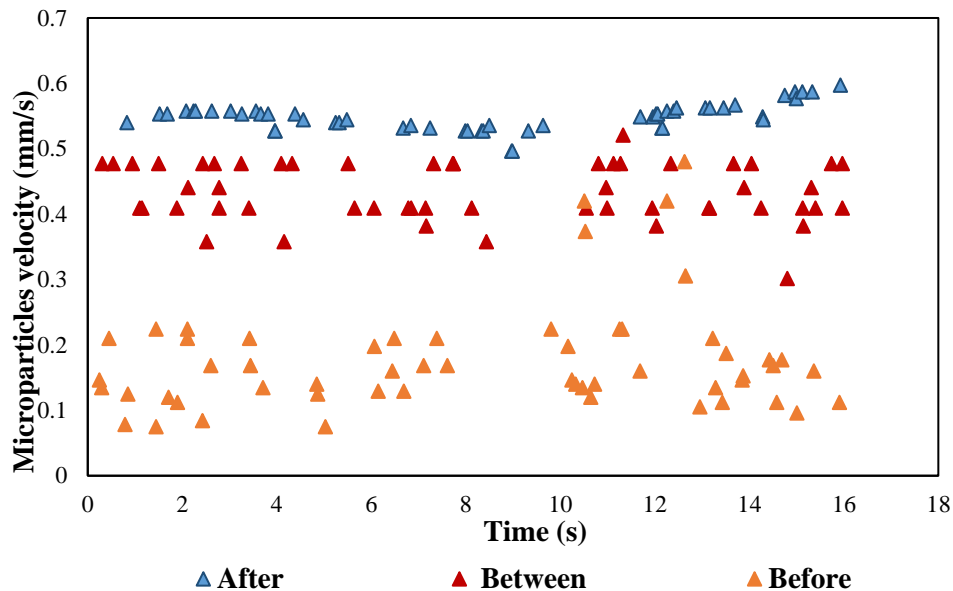
Figure 5-13 Velocity distribution of 6 µm polystyrene particles under three different conditions along the channel's length.

The experimental result is clear and in agreement with the results already described that particles flow fastest at the centre of the channel. However, there is an additional effect. The particles within the electrode region travel more slowly compared to their velocity after the electrode region. This indicates that the sum of forces at the end of the microelectrodes structure can accelerate microparticles. This was the case where the DEP force tried to push the microparticle away from the microelectrode edge in the direction of flow. However, this should only last tens of micrometres away from the microelectrode structure [20]. The microparticle velocity is expected to decrease with distance travelled within the focusing section itself, as a result of a gradual increase in the strength of the applied electric field with the converge shape of microelectrodes structure. However, we were unable to investigate the velocity of the same particles during the microelectrode due to the limited frame rate. Finally, Figure 5-13 shows a few microparticles (orange triangles and surrounded by a dashed circle) travelling at almost the same velocity as that in focus (red triangles). This might be due to their position around the centre of the microchannel. The plot shows evidence for a period of about two seconds without any particles passing. We also not that the particle velocity shows a minimum around this two second gap, perhaps a result of a partial clogging of the channel before it cleared itself and resumed the normal flow.

5.5 The separation distance between microparticles flowing under the n-DEP focusing force.

In this section, the distance between microparticles, as a function of applied voltage, is examined. In the absence of an applied n-DEP force, particles are randomly distributed within the channel width. They experienced hydrodynamic force and the distance between particles is unpredictable and time varying. When the microparticles motion is subjected to the dielectrophoretic force they flow in a single stream around the centre of the microchannel. The separations between particles are summarised in Table 5-1. The separation distance between two particles of less than 30 µm was obtained for some particles. This is important because we are using a 30 µm wide stripe laser, which produces a beam width of at least 30 µm. These results therefore indicate that there is a probability of detecting signals from more than one particle passing through the cross line of lasers/photodetectors in a final fully integrated device.

The dilution of the tested sample is one way to reduce this probability, but it would be at the cost of reduced throughput. Furthermore, it may not be effective if particles clump or cohere. In the next chapter, the effect of focusing microelectrodes on counting, sensing and sorting different particles will be investigated more quantitatively.

Table 5-1 Microparticles separation distance.

Size (µm)	Voltage (V Peak-to-peak)	Frequency (MHz)	Average distance (µm)	Detected particles with separation distance < 30 µm / out of total number
6	40	30	158.4	9 / 53
6	40	10	39.4	114 / 213
10	30	10	112.2	25 / 75
10	20	30	205	7 / 65

5.6   Summary

In view of the obtained results, velocity measurements could be an indirect way to confirm particle position at an equilibrium height within the depth of the microchannel. The microparticle suspension is introduced by capillary action only, this means that the speed of microparticle (flow rate) inside microchannel is not controlled. Also, the change in speed is more in the vertical direction so focusing microparticle in the vertical direction is more important. The microparticles position control on the Y–axis (side view) as well the X–axis (top view) decreased the risk of detecting different signals from particles passing the detection region at different heights, due to the fact

that multiple particles can fit within the height of the microchannel. In the case of a laser light source, the divergence of a laser beam has an elliptical cross section, this means the beam width is a function of the particle height inside the microchannel not the size. The performance of the focusing section was investigated and results shown that microparticles can clearly be distinguished and tracked when using a sample concentration of 2×10^{7} beads/mL. The sensitivity to the position under the n-DEP force with further analysis provides valuable information about the velocity of microparticles and so the fluid itself in the capillary driven system. The average speed of microparticles, and also the fluid speed, is decreasing (e.g. from 1.60 ± 0.10 mm/s to 1.23 ± 0.04 mm/s) with time. However, the result has shown that such velocity variance, assuming microparticles are focused to the same central position, is not significant as the differences in velocity seen for unfocused ones. The highest velocity is obtained in the centre of the microchannel, this suggests that the fluid speed is also highest at the centre of the microchannel. With the intention of using in a fully integrated device, with an array of $30 \, \mu$m wide strip laser, the results have shown that there is still a probability of detecting different signals from more than one particle with a separation distance less than the width of the light source and this will be investigated more quantitatively in the next chapter.

5.7   Bibliography

[1]   M. Leach, M. Drummond, and A. Doig, *Practical Flow Cytometry in Haematology Diagnosis*. 2013.

[2]   R. Nunez, "DNA measurement and cell cycle analysis by flow cytometry," *Curr. Issues Mol. Biol.*, vol. 3, no. 3, pp. 67–70, 2001.

[3]   "PIV measurements in a microfluidic 3D-sheathing structure with three-dimensional flow behaviour," *J. Micromechanics Microengineering*, vol. 12, no. 6, pp. 862–869, 2002.

[4]   K. Oshii, J.-E. Choi, and H. O. and M. Takei, "Measurement of Dielectrophoretic Velocities of Microparticles in a Minichannel," vol. 2, no. 4, pp. 1–14, 2011.

[5]   A. Sobiesierski, R. Thomas, P. Buckle, D. Barrow, and P. M. Smowton, "A two-stage surface treatment for the long-term stability of hydrophilic SU-8," *Surf. Interface Anal.*, vol. 47, no. 13, pp. 1174–1179, 2015.

[6]   R. Thomas, A. Harrison, D. Barrow, and P. M. Smowton, "Photonic integration platform with pump free microfluidics," *Opt. Express*, vol. 25, no. 20, p. 23634, 2017.

[7]   W. Huang, R. S. Bhullar, and Y. C. Fung, "The Surface-Tension-Driven Flow of Blood From a Droplet Into a Capillary Tube," *J. Biomech. Eng.*, vol. 123, no. 5, p. 446, 2001.

[8]   H. S. LEW and Y. C. FUNG, "ON THE LOW-REYNOLDS-NUMBER ENTRY FLOW INTO A CIRCULAR CYLINDRICAL TUBE," vol. 2, no. 1968, 1969.

[9]   H. S. Lew, Y. C. Fung, and S. Diego, "Entry Flow Into Blood Vessels," vol. 3, pp. 23–38, 1970.

[10]   D. Holmes, H. Morgan, and N. G. Green, "High throughput particle analysis: Combining dielectrophoretic particle focussing with confocal optical

detection," *Biosens. Bioelectron.*, vol. 21, no. 8, pp. 1621–1630, 2006.

[11] D. Williams and I. Sebastine, "3D focusing of nanoparticles in microfluidic channelss," *IEEE Proc. nanobiotechnology*, vol. 152, no. 6, pp. 207–211, 2005.

[12] H. Ching-Te, W. Cheng-Hsin, and J. Chun-Ping, "Three-dimensional cellular focusing utilizing a combination of insulator-based and metallic dielectrophoresis," *Am. Inst. Phys.*, vol. 5, no. 4, pp. 1–11, 2011.

[13] H. Tachibana, M. Saito, K. Tsuji, K. Yamanaka, L. Q. Hoa, and E. Tamiya, "Self-propelled continuous-flow PCR in capillary-driven microfluidic device: Microfluidic behavior and DNA amplification," *Sensors Actuators, B Chem.*, vol. 206, pp. 303–310, 2015.

[14] M. S. Maria, P. E. Rakesh, T. S. Chandra, and A. K. Sen, "Capillary flow-driven microfluidic device with wettability gradient and sedimentation effects for blood plasma separation," *Sci. Rep.*, vol. 7, no. June 2016, pp. 1–12, 2017.

[15] N. Demierre, T. Braschler, R. Muller, and P. Renaud, "Focusing and continuous separation of cells in a microfluidic device using lateral dielectrophoresis," *TRANSDUCERS EUROSENSORS '07 - 4th Int. Conf. Solid-State Sensors, Actuators Microsystems*, vol. 132, pp. 1777–1780, 2007.

[16] L. Wang, J. Lu, S. A. Marchenko, E. S. Monuki, L. A. Flanagan, and A. P. Lee, "Dual frequency dielectrophoresis with interdigitated sidewall electrodes for microfluidic flow-through separation of beads and cells," *Electrophoresis*, vol. 30, no. 5, pp. 782–791, 2009.

[17] A. Hilal-Alnaqbi, A. Alazzam, S. Dagher, and B. Mathew, "Analysis of dielectrophoresis based 3D-focusing in microfluidic devices with planar electrodes," *Proc. Annu. Int. Conf. IEEE Eng. Med. Biol. Soc. EMBS*, no. July, pp. 3588–3591, 2017.

[18] C. P. Jen, C. H. Weng, and C. Te Huang, "Three-dimensional focusing of particles using negative dielectrophoretic force in a microfluidic chip with insulating microstructures and dual planar microelectrodes," *Electrophoresis*, vol. 32, no. 18, pp. 2428–2435, 2011.

[19]   S. Fiedler, S. G. Shirley, and T. Schnelle, "Dielectrophoretic Sorting of Particles and Cells in a Microsystem," vol. 70, no. 9, pp. 1909–1915, 1998.

[20]   G. Ferrier, "Electronic detection of dielectrophoretic forces exerted on particles flowing over interdigitated electrodes," vol. 024117, no. June 2012, pp. 1–15, 2014.

Chapter 6

DEP FOCUSING EFFECT ON THE LASER LIGHT SIGNALS OF THE MICROFLUIDIC DEVICE

6.1   Introduction

In this chapter, a novel photonic integrated platform with on-chip capillary driven microfluidics and dielectrophoresis (DEP) particle focusing is presented. All components are integrated directly onto a single chip of III-V semiconductor material to demonstrate the feasibility of true chip scale flow cytometer. In particular, we show the strength and potential of n-DEP focusing force in both horizontal and vertical directions to overcome the variations in detected signal shapes that occur because of variations in position rather than the desired measurand, for example particle size. This removes the need for complicated data analysis which is time-consuming. The main advantages of our system are its relatively small size with no alignment required, and thus no coupling losses (the laser beam directly interacts with the analyte of choice) allowing for in situ haematology assessment. Besides, the chip design is scalable and compatible with standard microfabrication process and industry-standard material ideal for mass-production and of fully integrated devices.

6.2 Device configuration

In its simplest form, the active devices can be operated as a light source or photo-detector. By electrically forward biasing one section (source cavity), the resulting light that is transmitted across the gap and coupled into the active region of the opposing section (source cavity) can be detected through measuring the photo-voltage generated in that section. The proposed design of the prototype is shown in Figure 6-1. The device consists of a 30 µm wide oxide stripe lasers etched into the surface of a semiconductor wafer and set 100 µm apart either side of the 3D microfluidic channel. The microchannel is 60 µm in width, and about 30 µm in height patterned over a deeply etched semiconductor surface. p and n-contact metal are patterned on top of the upper surface to allow electrical biasing. The microchip is fabricated from GaInP/AlGaInP quantum well material grown on an n-type GaAs substrate emitting at ~ 650 nm wavelength, and the process steps used to build up this device are detailed in chapter 3. The numbers (0 - 7) seen in Figure 6-1 correlate to the specific numbering of driver boards in the control electronics and within the associated computer software for the lasers/photo-detectors. This numbering will be used to label the results later in this chapter. Experimental setup will be presented in the following section.
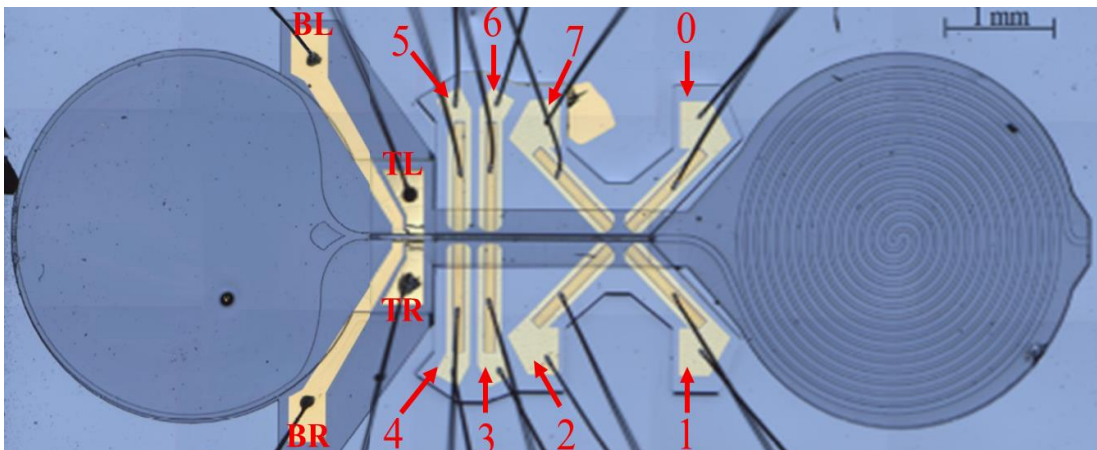
Figure 6-1 Plan view of a photonic integrated chip with an oxide stripe laser/detector sections and the critical components of the capillary fill microfluidics. Optical microscope image shows, from left to right, the inlet reservoir, the 3D microfluidic channel in the centre between the dielectrophoretic metallic microelectrodes and laser sections, and the spiral outlet. The numbering (0 to 7) of each laser section relates to orders from the computer software to the electronics in the control box. The black lines are wire connections made to connect each of bottom (B) and top (T) metallic microelectrodes for the DEP (DEP required microelectrodes)

and p- and n- side contact for each of the laser sections to gold-plated pads with PCB. Here R and L denote the Right and Left side of the microchip.

6.3   Experimental setup

The essential components of the experimental setup used for all on-chip light detection measurements are given in Figure 6-2. The packaged chip is plugged directly into a control unit. The electronic boards housed in it are required to drive and sequence the lasers that also sample and amplify the recorded photo-voltage signals. The control box also contains the electrical connections to power the DEP focusing microelectrodes with an AC function generator. The AC function generator (AFG3101C) and a built-in-house circuit were used to generate a sine wave with the required voltage and frequency, creating a highly localized non-uniform electric field capable of focusing polystyrene microparticles in the flowing fluid via the n-DEP force without any complicated flow controls (external pump or syringe system). The control unit is designed with a low profile so that the whole package can be used within the working distance of a standard microscope, see Figure 6-3. This allows, in a research setting, the movement of microparticles to be recorded independently of on-chip light scattering measurements using a high speed camera (Mega Speed, Model MS60K-AB). A frame rate of 200 frames per second is used for the reasons mentioned earlier in this work.
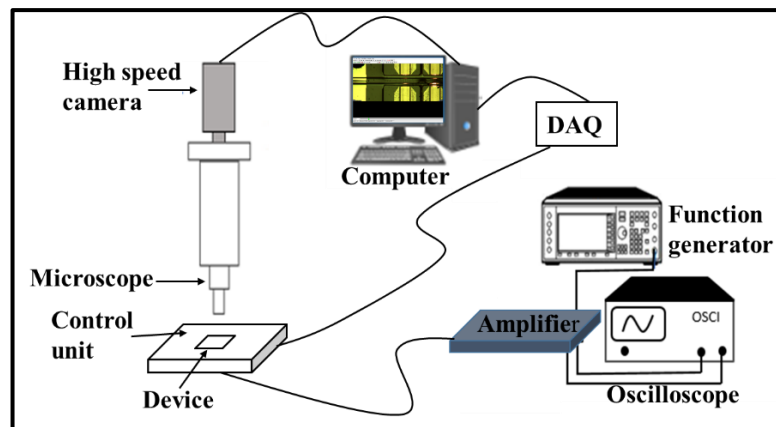
Figure 6-2 A schematic diagram of the experimental setup used to measure both single laser characteristic and time resolved microparticle detection events. The output from the function generator was displayed through an oscilloscope. DAQ stands for data acquisition system.
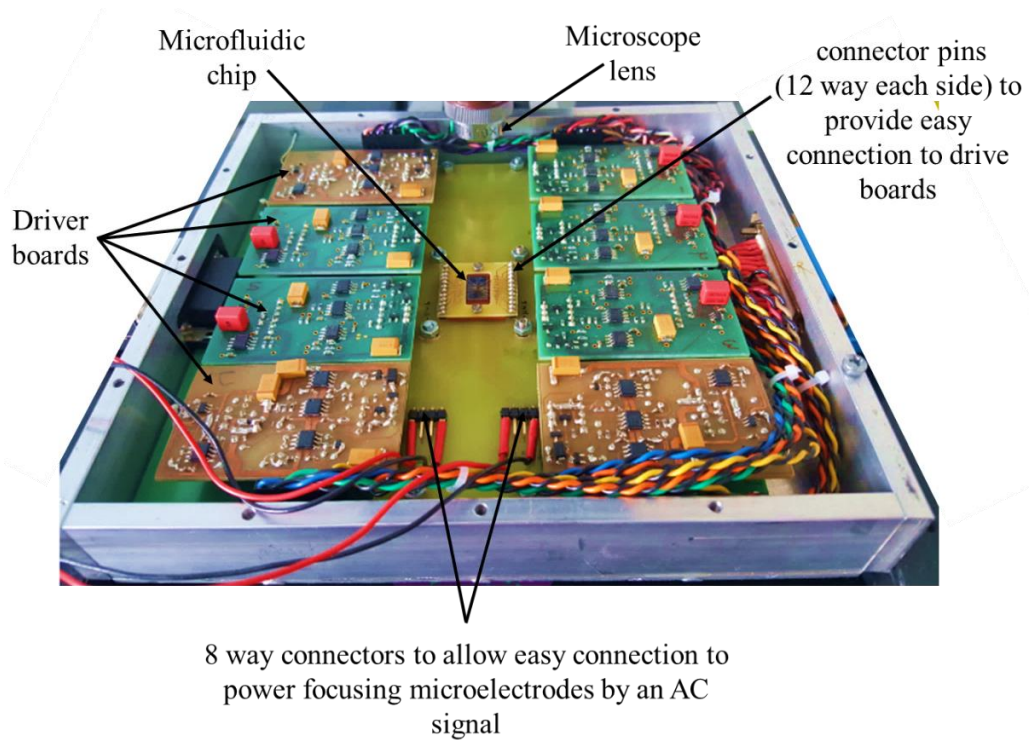
Figure 6-3 Image of in-house-made control system showing where the packaged chip sits, the 2 Amp electronic driver boards required to sequence and drive the lasers that also sample and amplify the photo-voltage signals, and the connecter pins to provide easy and secure connections to power focusing metallic microelectrodes by an AC signal.

The aim of this PhD is to investigate the strength and the potential of DEP focusing force on photo-voltage output shape during microparticle transit events for chip based flow cytometer. This work builds on the research of both Dr R. Thomas [1], [2] and Dr S. Gillgrass [3], from Cardiff University, using a fully integrated 3D capillary fill fluid delivery system and 10 µm wide ridge lasers [2] or 30 µm oxide stripe lasers [3] etched into the active semiconductor substrate. The variations in detected photo-voltage signal shapes, mainly three different types of events from the same sized microparticles, are due to the difference in microparticles' transit height as they are flowing through the light beam under capillary action. This is why the resulting data analysis is both complicated and time-consuming.

The oxide stripe laser, as mentioned earlier in this work, is in its simplest form encompassing the PIN diode. Each section can be electrically positive biased in sequence, so that whilst one part operates as a laser, the others act as photodetectors. In this chapter, the laser sections of the microdevice are operated with a pulse mode (duration of 800 ns at a repetition rate of 10 kHz). The laser output is highly sensitive

to temperature changes but under these pulsed conditions any current induced self-heating is negligible. The signal resulting from the detection of laser light in the adjacent reverse biased sections is amplified and recorded through a NI USB-6210 DAQ; then the data is transferred to a computer for analysis. This setup allows us to obtain a sequential laser operation. They are effectively toggling back and forth between laser and photodetector on alternate pulses, making a system where the laser beam transit events can be captured from both sides of the microchannel in sequence but interleaved in time.

The presence of a microparticle in the laser beam would show a photo-voltage output change compared to the normal signal. It is this change and the detail of the shape of the change which is different depending on the detail of the microparticles position. We hope to obtain a more uniform change in signal, from the same sized microparticles, indicating the DEP has made the particle position more uniform, with the flowing microparticles focused into a single streamline, in both vertical and horizontal directions. The microparticle transition time between known fixed points along the microchannel's length can be used to determine the microparticle velocity at the interrogation points. It should be noted in this setup that the high speed camera and microscope are used to characterise the performance of the microchip, although are not intended to be present in the final application. Also in the future, to reduce the cost and drive down the size, that would promote portability of the ultimate device, the computer can then be replaced by a smartphone, and the functionality of the DAQ and control electronics can be integrated on chip.

6.4 Optical particle sizing method

The laser source and detector are situated on opposite sides of the etched channel. A particle passing through a laser beam causes a disturbance to the power coupling between these elements across the microchannel. We measure a photo-voltage output change during the transit event. The population of microparticles appears as a peak or dip in the measured intensity. Reconfigurable lasers and detectors allow for time-resolved measurements to be taken to determine microparticle size and velocity at the interrogation point (where the velocity of the microparticles is not externally controlled).

In this work, we suppose that the collected light is scattered only once, this is where the excitation light from the source is scattered by individual microparticles, and this scattered light is collected. But, in practice, the chance of some multiple scattering needs to be taken into account if the microparticle is excited in the excitation light beam and the light scattered from other nearby microparticles. For example, in the designed microchip, multiple scattering comes into play if two particles pass the excitation beam with a separation distance of less than 30 µm, based on the expected laser beam width. In order to ensure that independent scattering will dominate, one could lower the sample concentration: however, this does not remove the existence of some multiple scattered light in the case where two or a large cluster of microparticles are stuck together. In practice, lowering the sample concentration would sufficiently lower the probability of two particles being very close together. On the other hand, lowering the sample concentration has the disadvantage of reducing the number of events to be analysed unless the sample volume is increased, which means increasing the analysis time and this exceeds that which can be recorded by the high speed camera.

As mentioned, there will always be a very small chance of two microparticles or a large cluster being stuck together, and hence the detected events will be interpreted as a large single microparticle, as is observed later in the chapter, or a microparticle with many more internal features. Analytes of interest can make doublet (double detection) events if they are either back-to-back or side-by-side in the sample stream. Figure 6-4 displays the multiple ways that double detection can take place and the effect it has on analysis abilities. It also gives a simple picture for what could be expected for a larger cluster of microparticles passing the light source/detector sections.
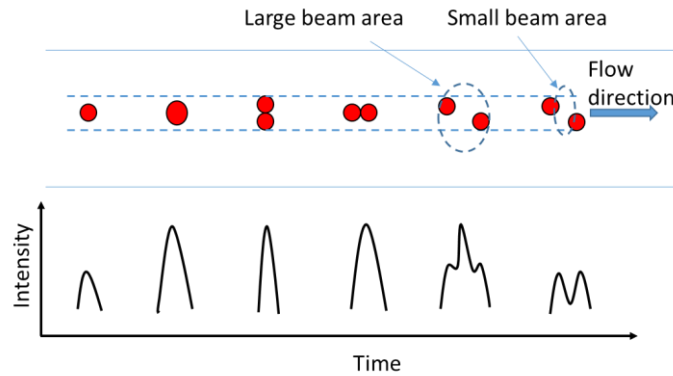
Figure 6-4 Representation of several detection possibilities that show single and double events. Single particle, large particle, doublet lateral orientation, doublet sequential orientation, doublet (large beam) and singlets (small beam) from left to right.

The on-chip light-current (L-I) curves that result from operating the device in the laser/detector configuration have been measured to determine the threshold current of a laser device, as presented in the next section.

6.5   Result and discussion

6.5.1   Light-Current measurements

When using a semiconductor laser, it is essential to know its performance characteristics. One of the most commonly used laser characteristics is the L/I curve. It shows the current required for the device to obtain a specific level of light output. Using a device fabricated as described in chapter 3 and the experimental setup as illustrated in section 6.3, on-chip L/I curves have been measured. By user selection of sections as either laser or detector and current automated step of 10 mA the measured L/I curves from two different samples, namely 1658 and 1659, are shown in Figure 6-5. They have been obtained by measuring the resulting photo-voltage on the selected detector until the predetermined current limit is reached. Note this result is reached using the device with a forward biased laser section (L) and with an empty microchannel, an air gap between laser and detector pair.
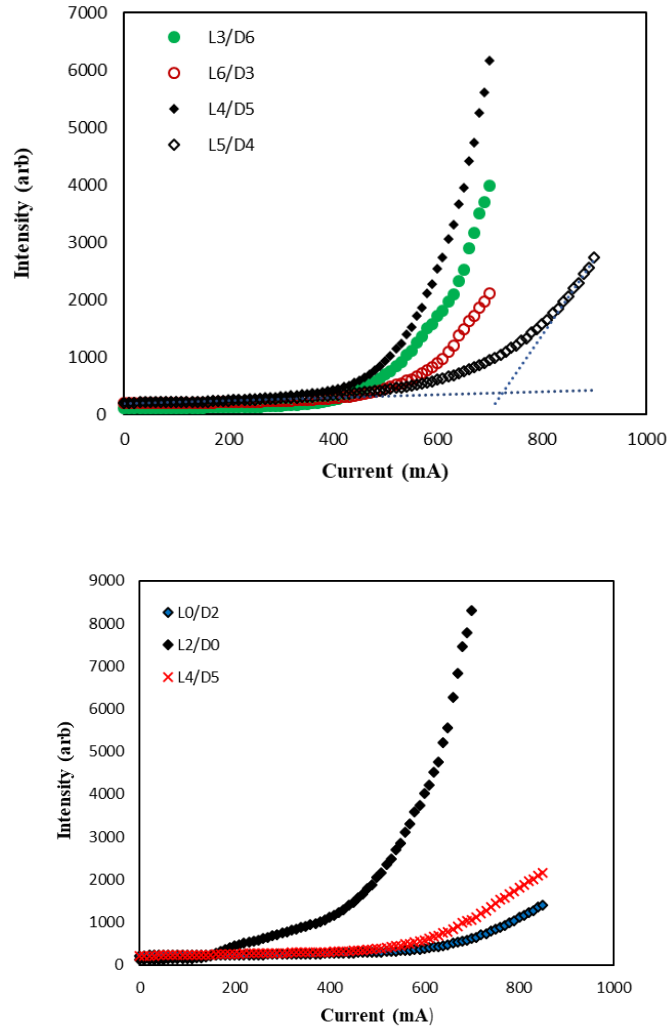
Figure 6-5 On chip L/I curves for two different devices named 1658 (above) and 1659 (below) measured using one section as a source (L) and the other section as a detector (D) with fluidic microchannel empty. The two straight lines fitted to the L5/D4 data in the upper plot illustrate how the I_{th} value is taken from that L/I curve.

The abrupt change in the gradient of the curve associated with the transition from below threshold spontaneous emission to above threshold lasing (stimulated emission). The threshold current value (I_{th}), for these devices, has been extracted from each of the L/I curves by fitting straight-line functions to both the below and above threshold regions of the curve. Then the I_{th} is taken to be the intersection point between these two lines, see Figure 6-5. From the L/I curves, the most common question I get, are the light source LEDs not lasers. A complicated question, but I should note that at this stage of this work (simple (present/absence) detection) weather the devices are lasers or LEDs not a problem. However, for chip based particle sensing, lasers are high

in power compared to a LEDs, together with other laser advantage (see chapter 2), this means increase system efficiency. The end conclusion is that any laser scatter enables higher signal to noise even with a higher cost per device.

6.5.2   Microparticle detection

6.5.2.1   10 µm polystyrene microparticles

In this section, detection of polystyrene microparticles is used to prove that the n-DEP force indeed focussed them into a single streamline using a laser/detector pair configuration and the experimental setup as described in section 6.2. The 10 µm polystyrene microparticles were purchased from Thermo Fisher Scientific, suspended in DI water at a concentration of 2×10^7 particles/mL. The sample used in the experiment was prepared through further diluting with the DI water by a 1:9 ratio to a final concentration of 2000 particles/µl. This is to ensure that single detection is dominant and that the probability of clogging the microchip is reduced. A (1 ± 0.2) µl volume of sample was deposited into the inlet reservoir of the fluidic system by a micropipette, and 120 seconds of data were recorded from the adjacent laser/detector (L/D) pairs.

An AC potential of 40 Vp-p, at a frequency of 30 MHz was applied across the microelectrodes. Immediately after the injection of sample, the recorded video using the high speed camera showed that for almost 35 seconds all the recorded microparticles passed through the microchip interacted with the generated electric field and clearly laterally focused to the centre of the microchannel, and they did not change position downstream where the L/D sections were. However, the L/D sections were not detecting large numbers of particles. In Figure 6-6 there is evidence of one spike in the data levels and this is believed to be due to a large clump of particles.
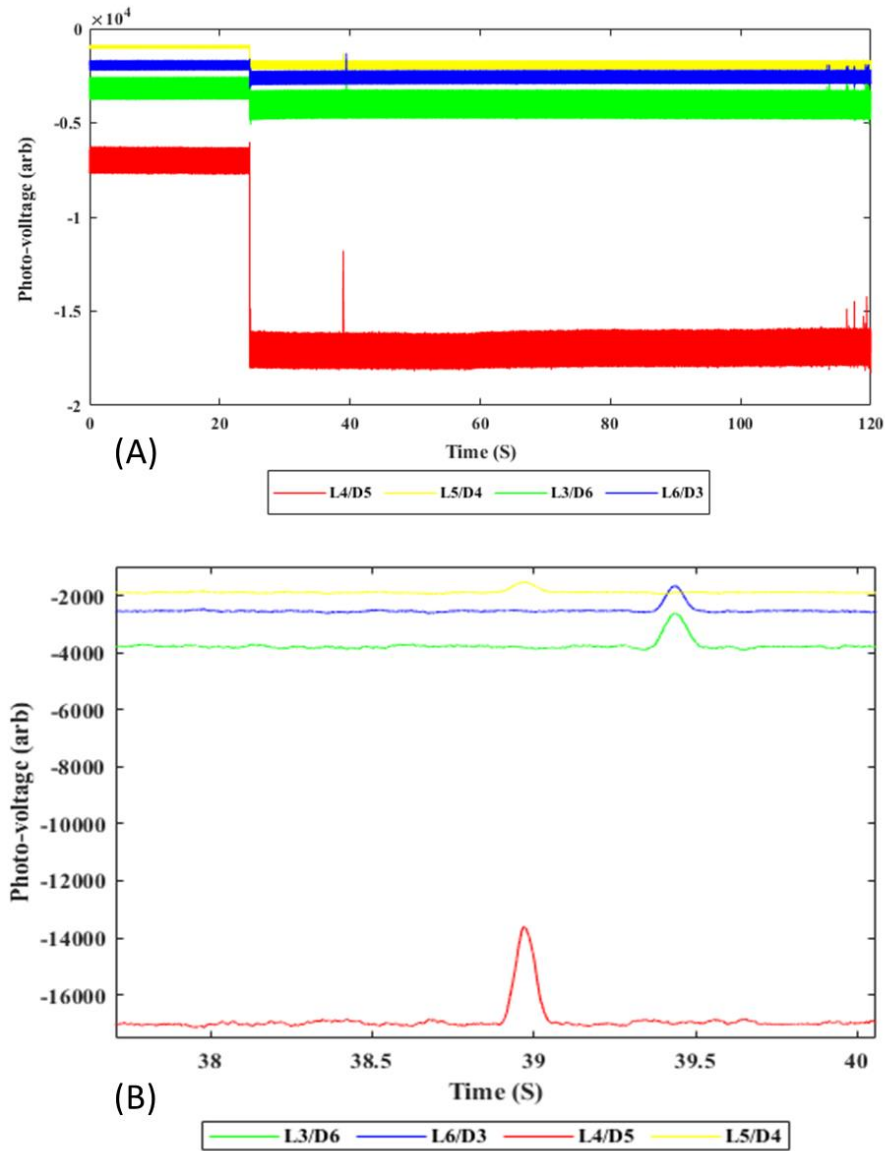
Figure 6-6 (A) Photo-voltage signals and (B) closer inspection of the smoothed data from an adjacent laser/detector pairs for a flow of 10 μm in diameter polystyrene microparticles.

The signal (sharp spike), spotted at about 39 second (s) in L/D data, corresponds to the clumped (four) microparticles captured on the high speed camera, see Figure 6-7 (D) and (E).

As we get fewer detection events when we apply the DEP we assume that the null signal arises because the focused microparticles position and the optical axis of the lasers and photodetectors is misaligned ie the lasers active region is not at the central point of the microelectrodes.
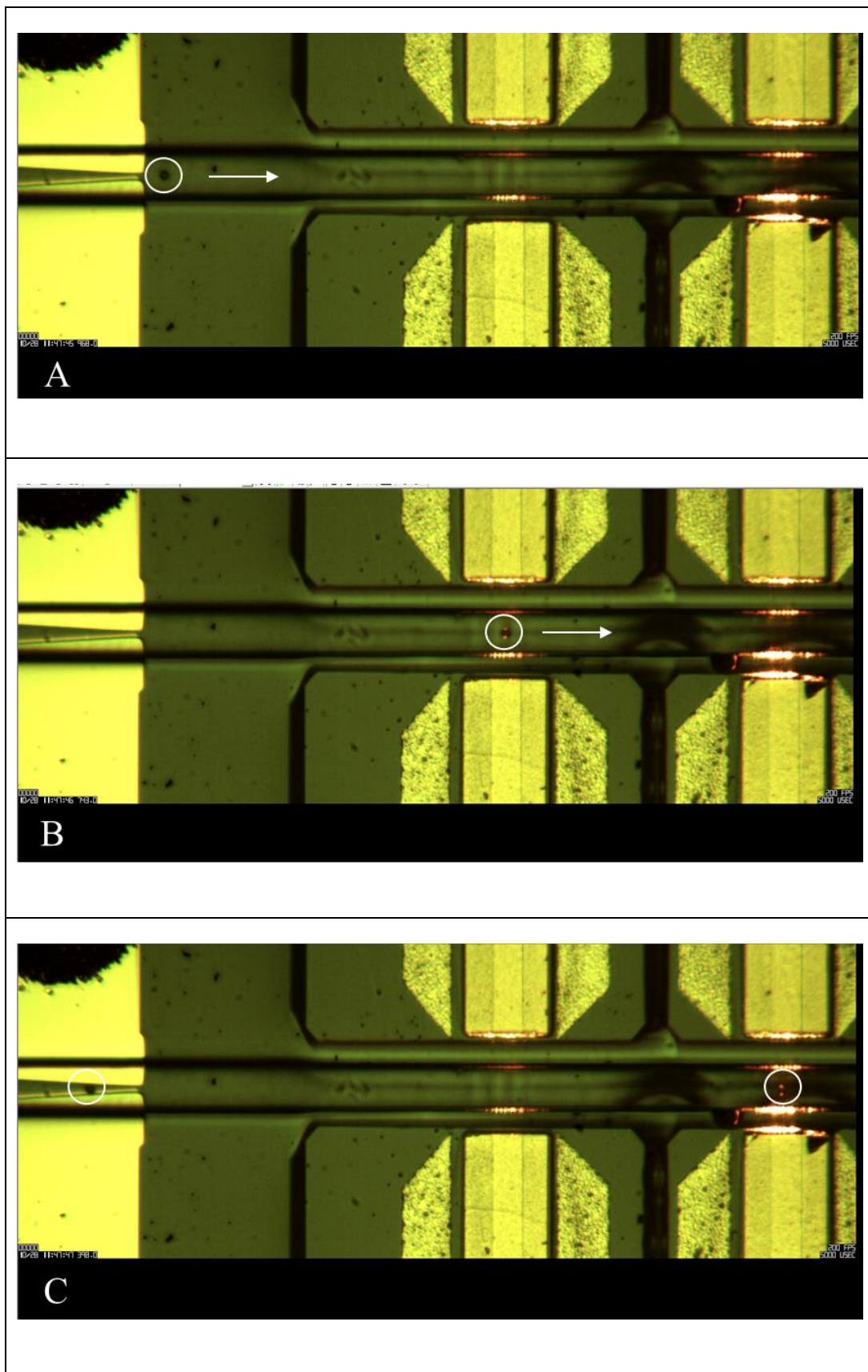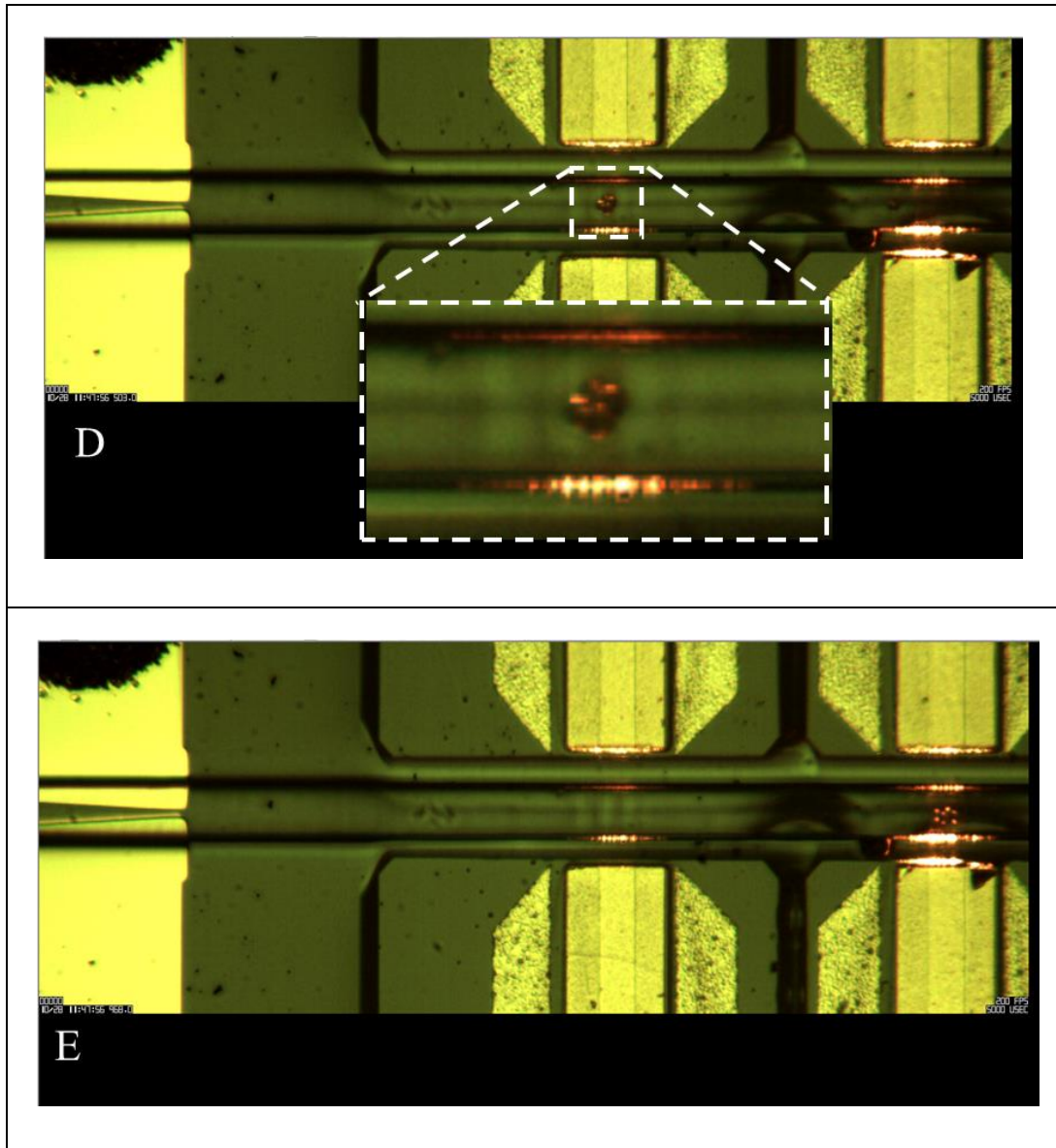
Figure 6-7 High speed camera images of polystyrene microparticles passing through the embedded 3D microchannel (top view). The n-DEP force works from the time the microparticles pass through the metallic microelectrodes on the left, producing laterally focussed microparticles. These microparticles then travel through the integrated laser/detector section on the right where it passes two lasers for particle detection and to investigate the success of their vertical focusing. Figures A-C show an example of a single focused particle exiting the electrodes (A), passing the first laser (B), and passing the second laser (C), but producing no detection pulse in the system, possibly due to misalignment of the lasers active region with the central point of the microelectrodes. On the other hand, a clump of microparticles that was focused by the electrodes and travelled through the lasers (D) and (E) has been successfully detected by the lasers, and has been used to comment on the microelectrodes' vertical focusing. From the selected frames, the scattered red laser light from the sidewalls of the microchannel and the front edge of the detector can be seen. This simply decreases the intensity available for measurements.

Previous work [2] on polystyrene microparticle detection with a capillary fill fluid delivery system, using 10 µm ridge lasers, found that there were three main types of trace recorded (except the null type): i) single peak, ii) single dip, and iii) double dip. These shapes were explained as originating from the interaction of the elliptical far-field distribution of the laser diode and microparticles travelling at different vertical positions. The channel of the capillary driven microsystem is 25 µm in height by 50 µm in width and several microparticles (10 or 15 µm in diameter) can fit into the microchannel height. First, the single peak, is a positive difference in signal intensity caused by a microparticle traveling at a microchannel height greater than one microparticle's radius. When a microparticle is at this height light travelling directly to the detector from the source continues to be detected and is supplemented by divergent light that would otherwise miss the detector being directed back to the detector as the bead passes producing a very small positive signal. Secondly, the single dip, is a decrease in the recorded light level caused by a microparticle travelling at a height slightly off-centre and partially blocking light as it passes. Thirdly, the double dip, is the signal that results from a microparticle passing through the central point of the microchannel. Based on fabrication accuracy, that is where the optical axis of the laser/photodetector pair intersects with the midpoint of the microchannel. The microparticle at the central point blocks the light falling on the photodetector but at the very central point focusses the light falling on the photodetector and enhances the detected intensity before blocking it again on the other side of centre. In addition to the three detection type events there is also the possibility of a null event when the particle does not intersect the beam between laser and detector.

During the test, the applied AC potential is turned off (no DEP) and the differences in signal are expected due to variations of microparticles vertical position within the excitation beam [2]. In general, the signal is too noisy to see the expected differences due to the different positions of regular microparticles (the same size within ± 0.09 µm). The signal detected for the clumped microparticle had a similar shape for different detector pairs L5/D4 and L6/D3 but not precisely similar. Therefore, we may be able to judge something about the vertical position of the sample using these results that the DEP focussed microparticles not only horizontally but also vertically.

The sharp increase in the background signal intensity of all traces that occurs around 25 s seen in Figure 6-6 (A), is a result of the initially empty microchannel filling with fluid, water in this case. As mentioned earlier in this chapter, the presence of water in the microchannel increases the refractive index of the gap between the L/D pair and decreases the reflectivity of the two interfaces, the latter improving the coupling and therefore the detected signal. This demonstrates that the device can be used in a simple forwarded scatter detection of an analyte of choice. However, most particle events were missed in a very simple detection (present/absence) decision, although this should be solvable by improving the fabrication process flow and ensuring that the active region of the laser will intersect with the central point of the etched 3D microfluidic channel.

6.5.2.2   15 µm polystyrene microparticles

The same strategies were used to examine the detection of 15 µm diameter polystyrene microparticles. The microparticles used here were also purchased from Thermo Fisher Scientific and were supplied at the same concentration and in the same suspension as the mentioned 10 µm polystyrene microparticles. The microparticle sample used was further diluted with 5% DI water, as previously explained, to reduce the probability of microchannel blockages although this also reduces the number of transit events.

Video data recorded by the microscope camera indicates that the microparticles did not laterally focus into the centre of the microchannel, which we assume is due to misalignment, however, all 14 recorded microparticles behaved similarly (same position) when n-DEP was applied focusing them into a single streamline, see Figure 6-8.
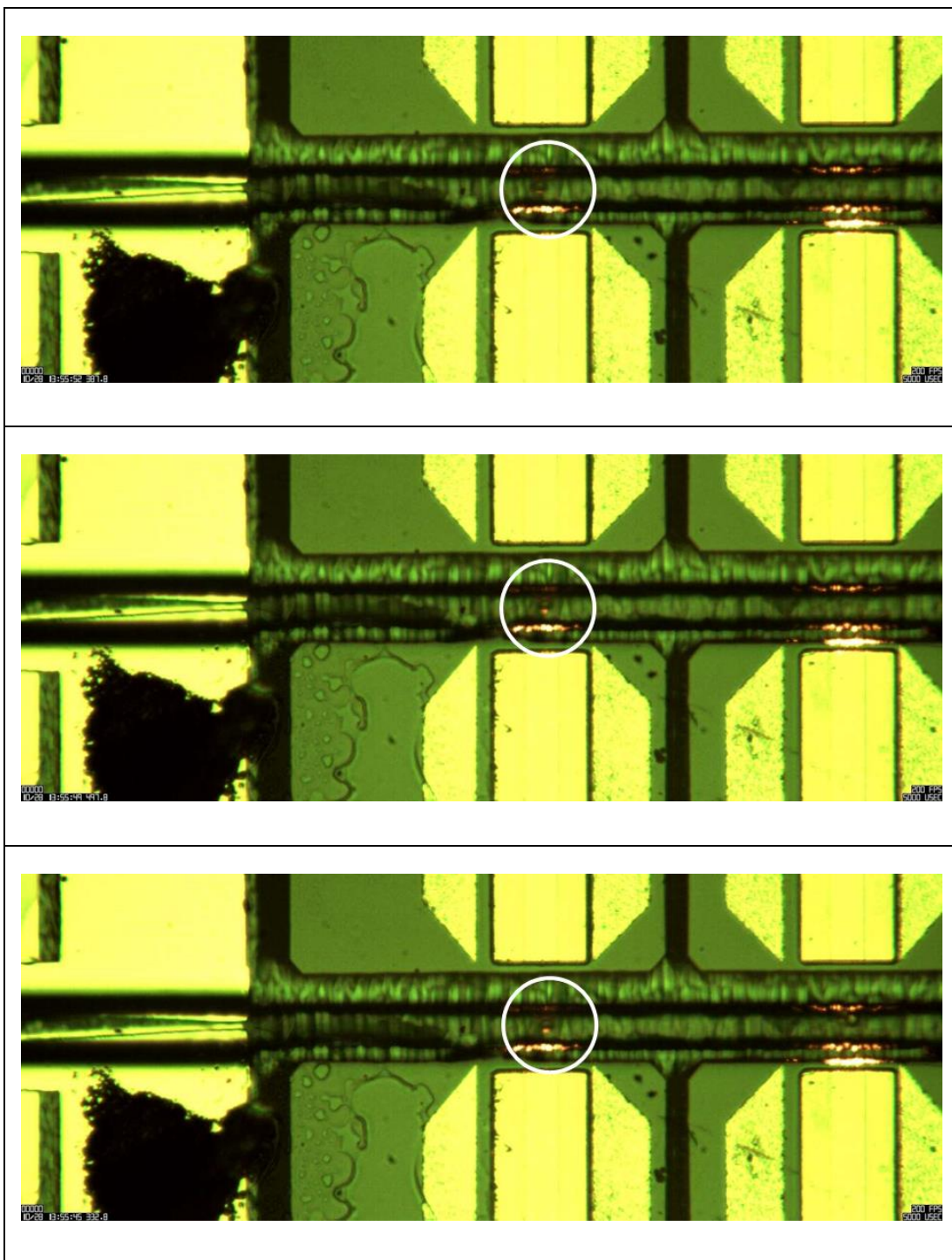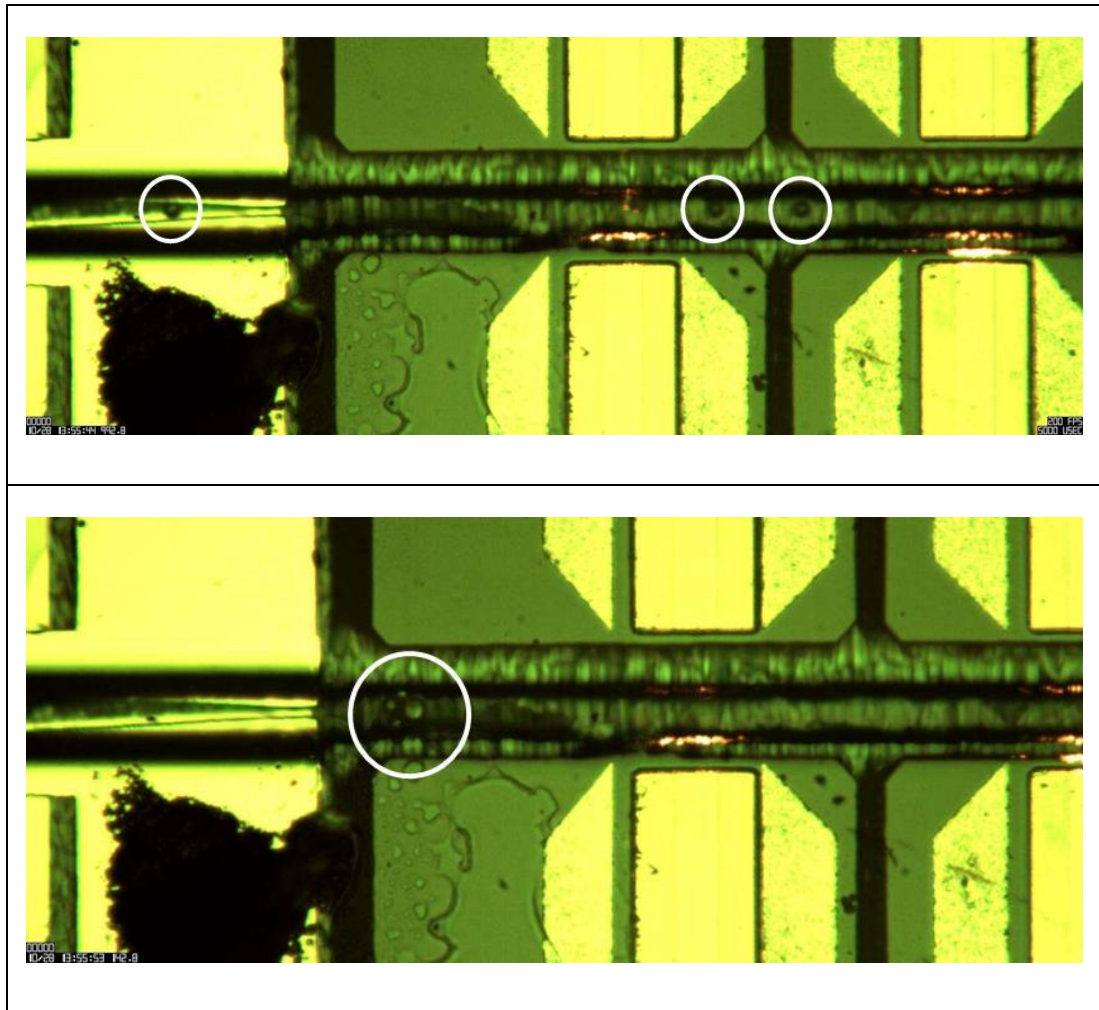
Figure 6-8 High speed camera images of 15 μm polystyrene microparticles flowing through the embedded 3D microchannel; this is while the movement of microparticles was subjected to the n-DEP force. First four figures show an example of focused microparticles (not at the centre point (sideways) of the microchannel) passing through the microchannel (top view) and the last figure shows microparticles building up and blocking the microchannel.

On closer inspection of the L/D numerical data, there is only one type of microparticle event. The same shape signals for recorded microparticles indicate that the n-DEP force works to expectation and the microparticles travel through the laser beam at fixed position both laterally and vertically. The raw data is plotted in Figure 6-9 with a more detailed plot in Figure 6-9. I now explain the detailed inspection necessary to understand this data. We note that the photo-voltage signals observed in L0/D2 or L2/D0 of Figure 6-8 are not always followed with an observable event on L4/D5. To understand this the L0/D2 signals that were unrecognised on L4/D5 were compared with the camera recorded video. It seems that there are microparticles in the

microchannel from a previous test. I note that, L5, L3/D6, L6/D3, L1/D7 and L7/D1 did not work on this sample and therefore were neglected.

To understand the data fully the number of L/D detections is correlated with the video data. The first task is to align the time of the camera data with the L/D time, since, due to the limited camera recording time, this is started after the sample is injected while the photovoltage data time starts before injection of the sample. This is done using an observed blockage (frame number 1982) and counting microparticles backwards from this point. The first microparticle is at frame number 1831 (or $t_1 = 9.155$ s since the start of camera recording). The last observed photo-voltage signal on L4/D5 is at $t_1 = 15.85$ s. Since the change in signal due to the advancing liquid front occurs in L4/D5 at 5.315 s, we determine the camera has missed approximately 1.38 s (15.85 - (5.315 + 9.155)) of particle measurements on L4/D5, see Figure 6-9.
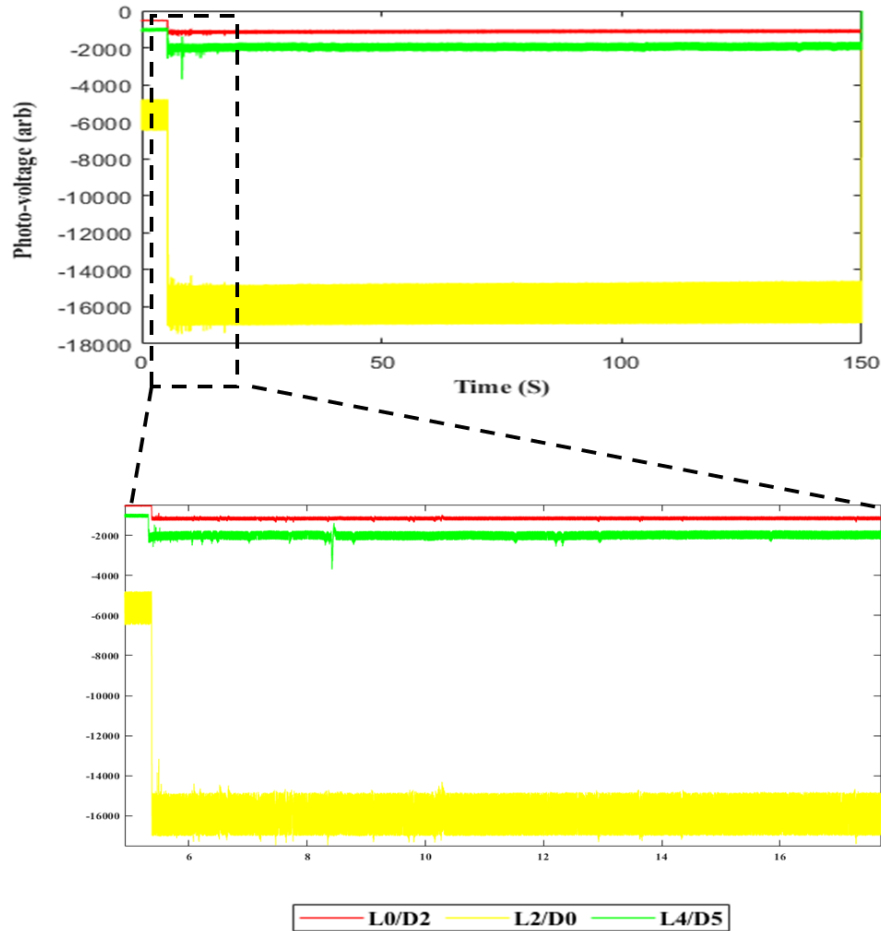
Figure 6-9 Photo-voltage signals from an adjacent laser/detector pairs for a flow of 15 µm diameter polystyrene microparticles. The spikes in the data are associated with individual transit events.

Thus, about 1.38 s is the period in laser data after water entrance which transit events are not reflected on the camera recorded video. This is only true if observed last photo-voltage signal on L4/D5 data is truly matching the last event (microparticle) observed by the camera before the observed blockage. We look to subsequently prove the case by measuring the time interval between the last and the second to last observed event on the L/D data and repeating the comparison. The second last observed microparticle on camera recoded video is at t_2, where $t_2 = 6.265$ s, so $\Delta t_{camera} = 2.89$ s, where Δt is the time difference between these two events. The second last observed signal on L4/D5 data is at 12.95 s, so $\Delta t_{Laser} = 2.9$ s. Both times almost match. It is, therefore, safe to count backwards and check if the number of microparticles on laser/detector data is same as detected microparticles on camera recorded video.
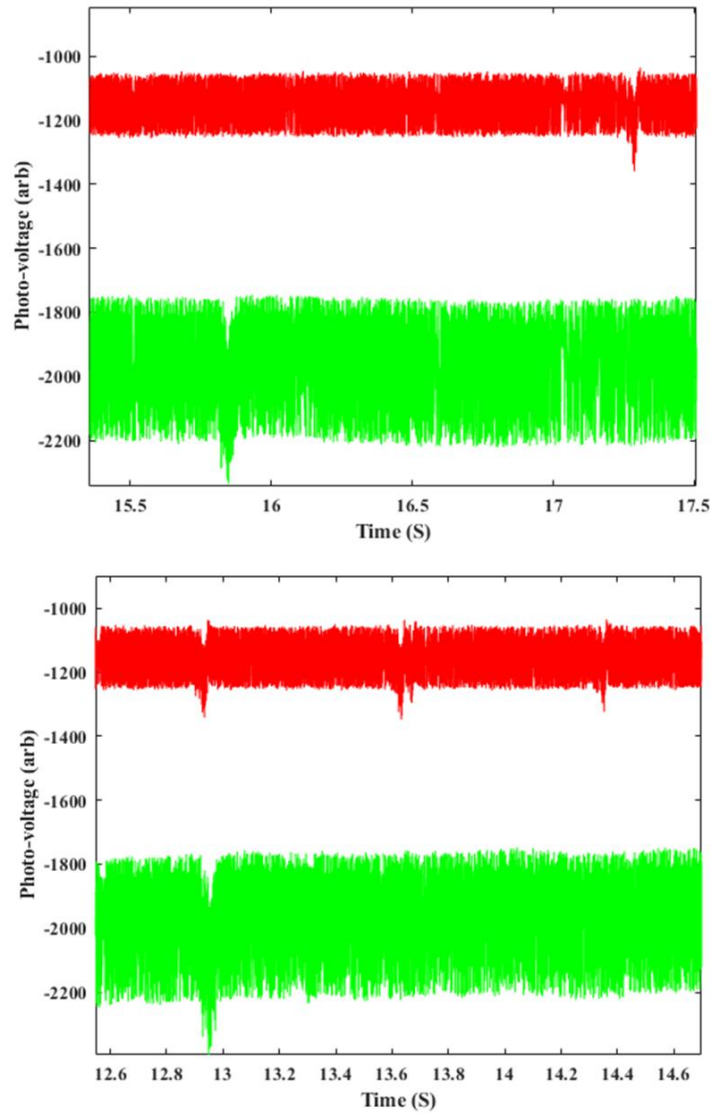
Figure 6-10 Zoom in of some events from Figure 6-9 showing the nature of the transit events.

On the camera recorded video we count only 14 microparticles, microparticle number 7 and 8 from the last observed event stuck together, and the n-DEP force caused them to rotate but not come apart, which is why the L/D signal changed in shape, see Figure 6-11. So not only it is clear that the spikes in the L/D data correspond exactly to microparticle transit events captured on the high speed camera, the DEP also worked to expectation and the photovoltage signal did not change its shape for the same size microparticle.
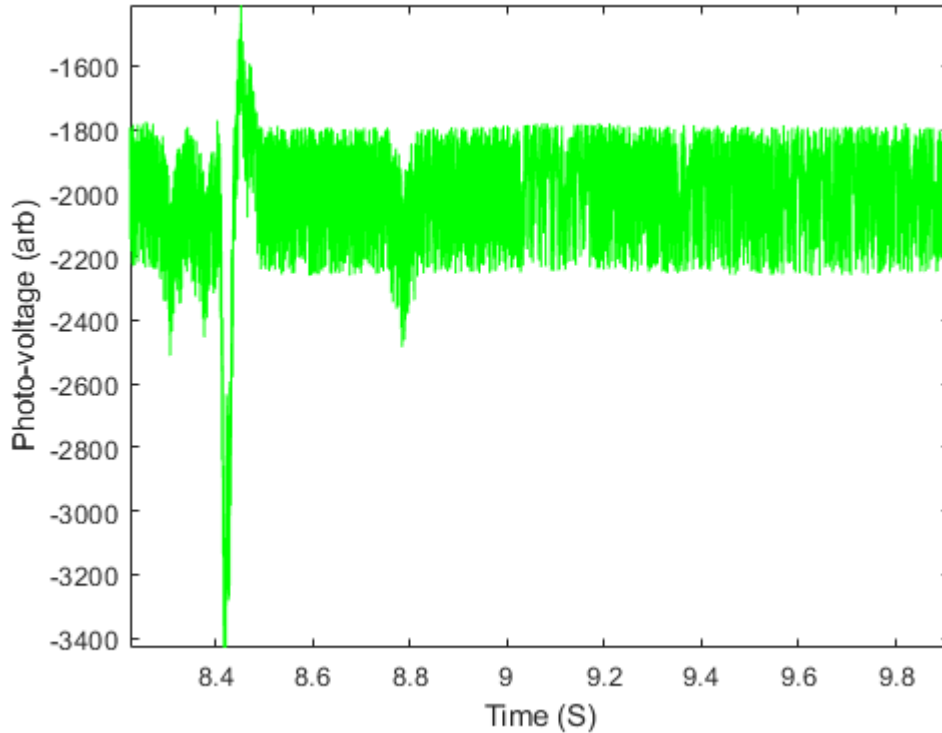
Figure 6-11 Zoom in of an event from Figure 6-9 showing the change in detected signal shape that occurs at around 8.4 seconds. This event corresponded exactly to microparticle number 7 and 8 captured on the high speed camera. The microparticles are stuck together and the n-DEP force did not make them come apart. Thus, we can argue that the spikes in the L/D data correspond exactly to the microparticle transit events.

These data show that the photo-voltage signal had the same shape for the same size microparticle, so it is more likely the DEP focuses microparticles in flowing fluid into a single streamline as expected. However, the signal does not look like the centred shape reported in [2], likely due to misalignment in the microelectrodes or misaligned laser sections with the centre point of the microfluidic channel.

6.6   Summary

In this chapter, the feasibility to integrate PIN photodiodes on a single substrate with on-chip capillary fill microfluidic delivery system and DEP particle focusing method to overcome variations in detected signals intensity from the same size microparticles is investigated. This is a step forward towards a true chip scale flow cytometry. Operating the microdevice in a laser/detector mode allows the photo-voltage generated

in the detector section to determine the light-current characteristics of the source section. The measured L/I curve shows the current required for the device to obtain a specific level of light. Based on the proposed design, the narrow-angle forward scattered light FSC was employed as a sensor to detect (present/absence) of polystyrene microparticles. The microparticle motion is recorded via a high-speed camera. In the experiments, the camera and microscope are used to characterise the performance of the chip and the effect of n-DEP on signal detection. The camera would not be required in the final device. The experimental results of each device are presented and discussed. The detected data shows the same signal shape for the same size microparticle which proves that the DEP force focuses the microparticle into a single streamline as expected. Although this chapter demonstrated that the performance of the n-DEP force in both horizontal and vertical directions overcome the variations in detected intensities from the same sized microparticles, it also showed that it reduces the tolerances in fabrication that can be acceptable. During fabrication of the microdevice, (chapter 3) we used two layers of SU-8 (SU-8 2002 and SU-8 3005) that serves as a base and electrical insulation. We have said that there is some variation across the SU-8. The SU-8 thickness is affected by spin speed and viscosity, but when we set the spin speed we should be able to achieve a thickness of (2 µm layer of SU-2002 and 5 µm layer of 3005), subject to having fresh SU-8. However, due to the cost of SU-8 and the short shelf life this is often not the case and the variation of the film thickness of the SU-8 photoresist is considered as the main factor that could led to difficulties in the eventual device. In the future, the thickness of the SU-8 will be measured so that we can ensure the laser will be at the mid-point of the channel and mid-way between the electrodes. Any imperfection in the lower SU-8 thickness can be compensated by the thickness of the top layer. Once the manufacturing tolerance is improved, it should be possible to extend the technique to microparticle size discrimination using forward scattered peak height or peak area.

6.7 Bibliography

[1]   R. Thomas, "Monolithic coupled-cavity laser diodes for bio-sensing applications," *PhD thesis*, no. Cardiff University, Cardiff, 2012.

[2]   R. Thomas, A. Harrison, D. Barrow, and P. M. Smowton, "Photonic integration platform with pump free microfluidics," *Opt. Express*, vol. 25, no. 20, p. 23634, 2017.

[3]   S. Gillgrass, "LASER HAEMOCYTOMETER," *PhD thesis*, no. Cardiff University, Cardiff, 2018.

Chapter 7

CONCLUSIONS AND FUTURE WORK

7.1   Summary and Conclusions

This thesis contained a description of the work that has been carried out to develop a novel photonic integrated platform with 3D capillary fill fluid delivery system and dielectrophoresis elements for chip based flow cytometer. The investigation has involved designing and fabricating a dielectrophoresis particle manipulation and control system with planar metallic microelectrodes, above and below the 3D capillary driven microchannel. Following fabrication of the capillary fill, dielectrophoresis actuated microchip, experimental characterization to determine a suitable alternating potential was performed. The designed planer microelectrodes produced a non-uniform electric field capable of focusing polystyrene microparticles in the flowing fluid via negative-dielectrophoresis (n-DEP) force. The focusing functionality aimed to improve the detection efficiency by reducing the variability of the detected signals in the device. The components of the microchip were integrated onto a single chip of III-V semiconductor material to form a chip scale flow cytometer. The theory behind the work was discussed in chapter 2, and in the following paragraphs, the major findings of the work are highlighted.

Chapter 3 presented the design and fabrication process necessary to create a novel integration of a dielectrophoresis system on an integrated optoelectronic microfluidic device. This required the development of integrated metallic microelectrodes. Two pairs of a triangular-shaped microelectrodes face-to-face below and above the surface of the 3D capillary fill fluid delivery system were proposed. The microelectrodes have to be capable of creating a localised non-uniform electric field to focus polystyrene microparticles in a flowing fluid around the centre of the microchannel via n-DEP force. The microelectrode design was either 380 or 300 µm in length and both were able to provide enough exposure time for the flowing microparticles to be moved under the influence of the n-DEP force. Any reduction in the length of the microelectrodes reduces the final chip size and so is advantageous. SU-8 negative photo-epoxy was chosen for the fabrication of the microfluidic system. This is due to its chemical and optical properties that allow for thick, nearly vertical exposure profiles to be created over a deep etched surface (GaAs substrate in this case). A 3D deep channel (25 – 30 µm) is built up in two layers of SU-8 using double exposure with spectral filters. Spectral filters were needed to select the required emission lines of a single mercury arc lamp. Thus, the 3D microfluidic structure is achieved using a conventional photolithography mask aligner within the cleanroom at Cardiff University. A thick layer of SU-8 3005 (~ 5 µm) is patterned over the GaAs substrate that provides an adhesion layer for the following layer and physical separation and electrical isolation from the GaAs substrate. The microchannel roof was successfully built using a layer of SU-8 3005 that was spin coated on top of SU-8 2050. The SU-8 3005 overcame adhesion problems for depositing the metallic microelectrodes above the surface of the 3D microchannel.

In a later stage of this research, SPR 220-7.0 thick positive photoresist in conjunction with an adhesion promoter HMDS was used to define the top microelectrodes instead of S1813 positive photoresist and the shadow mask. This is another significant achievement as it increases the number of samples in a process, which is otherwise a time consuming and costly single chip process. The fabrication process of the final fully integrated platform with lasers and photodetectors was presented. The developed process flow turns the design into a manufacturable integrated platform.

To allow reuse a two-stage cleaning process was developed. During the development stage of this device, this process especially improves the lifetime of the chip in use, which also reduces the timescale and the cost per experiment.

Chapter 4 focused on how the generated n-DEP, operating the metallic microelectrodes with an AC signal, will affect the dynamic behaviour of polystyrene microparticles inside the 3D capillary fill fluid delivery system. First, a theoretical study is presented to estimate the required frequency for the applied field based on the dielectric properties of microparticles and the surrounding medium. The results highlighted that frequencies in MHz range are required. Using different experimental conditions the n-DEP focusing of 6 and 10 µm diameter polystyrene microparticles was studied, varying the applied frequencies and voltages. The results suggested that both sizes of microparticles can be focused in a single stream around the centre of the microchannel when operating the microelectrodes with an AC potential of 10 MHz and no more than 30 V peak-to-peak. Further measurements revealed that the microparticles flowing downstream, to where the laser/photodetector sections will be in our final microchip, remained within the same focused position even after leaving the n-DEP region. This work illustrated, in the horizontal plane, the strength and potential of using DEP techniques for applications with capillary systems. To prove n-DEP potential in the vertical direction, more quantitative investigations were performed in chapter 5.

In chapter 5, velocity measurements of polystyrene microparticles inside the 3D microchannel were used to evaluate the performance of n-DEP in the vertical direction. The results suggested that the position is controlled with the polystyrene microparticles positioned at the same height. This is based on the narrower measured velocity distributions of the focused particles compared to those without the n-DEP applied. The unfocused particles are expected to be traveling in different stream lines; thus the velocity distributions are wider. In a capillary fill fluid delivery system, such as our system, the fluid velocity, i.e. the average velocity of the polystyrene microparticles, decreases with time. However, the result has shown that such velocity change (e.g. from 1.60 ± 0.10 mm/s to 1.23 ± 0.04 mm/s over about 35 seconds), assuming microparticles are focused to the same central position, is not significant compared to the velocity changes seen for the unfocused ones. The vertical focusing allowed the

microparticles to flow in a single stream at an almost uniform velocity. This work suggested that planar microelectrodes were successfully employed to focus microparticles with liquid flows in a single stream to the centre of the microchannel. Thus, the probability of detecting different signals from microparticles passing the detection region at different heights, because multiple microparticles can fit within the depth of the channel, would significantly be reduced. This is investigated more quantitatively in chapter 6. Also, the highest velocity of the microparticles was found at the centre of the microchannel, this suggested that the capillary force is only presented at the fluid front and the fluid flow becomes faster at the centre due to the greater friction at the side walls.

In Chapter 6, the fabricated fully integrated microchip was used to demonstrate more quantitively the strength and potential of the DEP focusing force for a chip scale flow cytometer. Operating the final III-V semiconductor platform in a laser/photodetector configuration allows determining the current required for the device to obtain a specific level of light. Measurements of narrow angle forward light scattering, based on the designed chip, shows that the presence of a polystyrene microparticle in the laser beam changes the photo-voltage output signal compared to the normal one. Using planer microelectrodes with cross (X) polarity of applied AC potential, the same signal shape was detected from the same size polystyrene microparticles. This indicates that the n-DEP force focuses microparticles within the liquid flow into a single stream around the centre of the 3D capillary driven microchannel. Polystyrene microparticles, based on volumetric similarity, were used as an example to investigate the potential of this chip scale and manufacturable photonic integrated platform for conducting scattering measurements of blood samples.

7.2 Future work

This work has been successful in developing a photonic integrated platform with a capillary fill fluid delivery system and integrated microelectrodes for particle focusing. Using DEP with capillary fill fluid delivery system, polystyrene microparticles within a stream have been positioned into the centre of the microchannel. A consistent pulse shape and peak have been observed in the laser illuminated detected pulses from

similarly-sized microparticles. This proves that the DEP focusing electrodes work to expectation, which significantly improves the detection mechanism by regulating the flow of the microparticles and passing them through a consistent scanning region. Nonetheless, in the future, there are certain aspects of this work that could be considered to further improve the device. These will be discussed briefly in this section.

During the course of the research, many of the fundamental device fabrication issues have been dealt with. However, additional improvement of the fabrication process would allow the optical axis of the laser/detector sections to intersect the middle point of the microchannel. The results obtained in chapter 6 suggest that there are some variations across the SU-8 which could lead to off-centred lasers in the final device. The variations in the thickness of the SU-8 are thought to be a result of not having fresh SU-8 used in each fabrication process, which was done to reduce cost. Therefore, in the future, the thickness of the SU-8 photoresist that has been deposited initially should be measured, then the recipe should be adjusted accordingly to ensure that the lasers/photodetectors are at the centre point of the microchannel and mid-way between the microelectrodes. This would increase the detection efficiency through reducing false negatives and positives in the detected pulses, while keeping the fabrication costs per experiment at a minimum.

Using a 30 µm wide oxide stripe laser, 10 and 15 µm polystyrene microparticles have been shown to have a measurable pulse. Microparticles with this size are comparable to some types of human cell biology. Smaller particles, such as nanosized metallic particles (about 500 nm in diameter), may have only a negligible effect on the optical coupling between laser sections. If so, it may be necessary to incorporate narrower ridge waveguide system into the device to maximise the influence that the nanoparticle has on optical coupling.

The performance of the device was verified by collecting narrow angle (forward) scattered light from a single population of polystyrene microparticles in solution. In chapter 3, I presented an extension to the microchip design (crossed laser configuration) to also allow the wide angle (side) scattered light collection. However,

the design has not yet been tested with a working laser. So, one of the main focuses of future work would be to operate one laser as a source, or an optical pump, while having the other three serves as detectors. The potential success of these suggested developments would allow the device to collect the scattered light patterns with both narrow and wide angle not only for microparticle identification, but also for a potential sorting using the same focusing principle, i.e. DEP. This would open up the potential for the device to demonstrate a performance as favourable as that of its commercial equivalent, i.e. the flow cytometer, except it would be on a simpler scale that is easy to configure and handle. In addition, the device's portability, transparency and size give the researcher more flexibility when handling the system, but with some changes to the current design. For example, the spiral channel with an open end is used in this work to provide a sustained pull at the sample fluid for a relatively long period. This setting is ideal for experiments that are focussed on particle investigations through the lasers' region only. However, if a researcher is also interested in investigating the particles after acquiring readouts from the on-chip lasers, a closed-end channel would be recommended. The closed-end channel would regulate the capillary flow by simply stopping it after a limited volume passes through the lasers' region. Thus, this would most likely provide the researcher with an ordered storage for the laser-inspected particles. The data acquired from the laser readings would then guide the researcher to locate the particle of interest in the spiral storage for further investigation under the microscope. If sorting DEP electrodes are added, the particles of interest could be automatedly sorted in real time into a closed-end sorting channel, based on pre-set scatter intensity thresholds by the researcher. Similarly, the researcher could then inspect these sorted particles with ease under the microscope, or even retrieve them if the device's channel design is changed so it allows for such a function.

Appendix

The shadow mask, made within the mechanical workshop of the School of Physics and Astronomy at Cardiff University, is designed with the essential elements to be aligned under an optical microscope. Once aligned, it is then very simple to use with the Edwards E306 thermal evaporation vacuum systems in a cleanroom. Figure A1-1 shows the designed mask that contains three main parts; i) a thin sheet of aluminium with pattern feature etched completely through the material, ii) a sample carrier which is designed for fixing the mask as well as a four-axis manual alignment to use under an optical microscope, iii) mounting points which allow the shadow mask to be fixed with eight screws and four pressure plates onto the carrier.

The use of this in house- made shadow mask was useful for metal deposition, because it prevents a continuous metal film from forming all over the surface of the sample which would be extremely hard to remove and also reduces the time required for lift-off, which reduces the solvent induced swelling of previously patterned SU-8. This process was not only a time consuming but also limited to a single chip and hence it was replaced with a more manufacturable process using the SPR 220-7.0 positive resist in conjunction with an adhesion promoter HMDS.
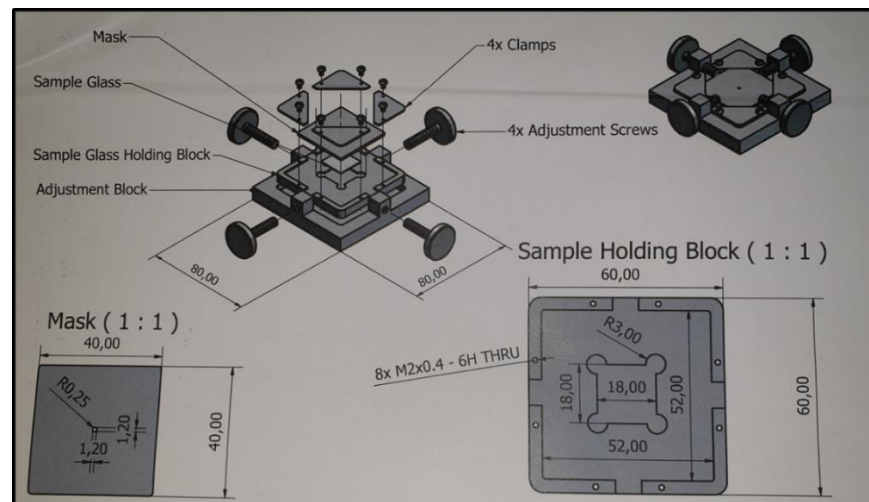

Figure A1-1 shows details of the shadow mask. After deposition the photoresist, the substrate being placed in metal deposition chamber. In metal deposition chamber, metal deposition process is carried out with the assistant of this shadow mask that prevent metal deposition film from forming where it will be hard to remove.